creative commons
COMMONS DEED

저작자표시-비영리-동일조건변경허락 2.0 대한민국

이용자는 아래의 조건을 따르는 경우에 한하여 자유롭게

- 이 저작물을 복제, 배포, 전송, 전시, 공연 및 방송할 수 있습니다.
- 이차적 저작물을 작성할 수 있습니다.

다음과 같은 조건을 따라야 합니다:

저작자표시. 귀하는 원저작자를 표시하여야 합니다.

비영리. 귀하는 이 저작물을 영리 목적으로 이용할 수 없습니다.

동일조건변경허락. 귀하가 이 저작물을 개작, 변형 또는 가공했을 경우에는, 이 저작물과 동일한 이용허락조건하에서만 배포할 수 있습니다.

- 귀하는, 이 저작물의 재이용이나 배포의 경우, 이 저작물에 적용된 이용허락조건을 명확하게 나타내어야 합니다.
- 저작권자로부터 별도의 허가를 받으면 이러한 조건들은 적용되지 않습니다.

저작권법에 따른 이용자의 권리는 위의 내용에 의하여 영향을 받지 않습니다.

이것은 이용허락규약(Legal Code)을 이해하기 쉽게 요약한 것입니다.

Disclaimer

dCollection

이학박사학위논문

Subtidal Temperature Variability in the Continental Shelf off the Mid-east Coast of Korea

한국 동해중부 연안의 장주기 수온 변동성

2014 년 8 월

서울대학교 대학원

지구환경과학부

조 창 봉

Subtidal Temperature Variability in the Continental Shelf off the Mid-east Coast of Korea
韓國 東海中部 沿岸의 長週期 水溫 變動性

指導敎授 張 京 一

이 論文을 理學博士 學位論文으로 提出함

2014 年 6 月

서울大學校 大學院
地球環境科學部
趙 唱 奉

趙唱奉의 理學博士 學位論文으로 認准함

2014 年 6 月

委 員 長 강 양 기

副委員長 장 경 일

委 員 박 종 진

委 員 이 재 철

委 員 승 영 호

Subtidal Temperature Variability in the Continental Shelf off the Mid-east Coast of Korea

A
Ph.D. Dissertation

by
Chang-Bong CHO

Supervisor: Prof. Kyung-Il CHANG

Thesis Committee:

Yang-Ki CHO
Committee Chairman
Seoul National University

Young-Ho SEUNG
Inha University

Jae-Chul LEE
Pukyung National University

Jong-Jin PARK
Kyungpook National University

Kyung-Il CHANG
Seoul National University

June 2014

Abstract

Subtidal Temperature Variability in the Continental Shelf off the Mid-east Coast of Korea

Chang-Bong Cho

School of Earth and Environmental Science

The Graduate School

Seoul National University

A wind-forced coastal trapped wave (CTW) model is applied to examine subtidal band (period of a few days to weeks) temperature variability in stratified shelf waters off the mid-east coast of Korea (at two coastal sites; an offshore site of 100 m depth and an inshore site of 27 m depth). The model-predicted temperature is significantly correlated with observed temperature (T_{OBS}) at offshore site ($r > 0.35$) and inshore site ($r > 0.36$). At both sites, the correlation coefficients increase when the remote wind forcing is included. Simulated phase speeds (4.6-5.9 m/s between Sokcho and Mukho and 9.5-10.3 m/s between Mukho and Pohang) are consistent with the propagating speeds of sea level observed along the coast (6.1 and 10.4 m/s, respectively) in spring and summer, 2001. The wind-forced CTW model reasonably reproduces the dominant portion of subtidal-scale temperature

variability, which is also supported by the comparison between T_{OBS} and T_{CTW} for the period of six years (2006 ~2011). However, T_{OBS} cannot be explained solely by the CTW model, particularly when nonlinear, horizontal advection becomes significant. This study suggests that abrupt changes in water properties caused by vertical mixing due to sudden downwelling and the eddy heat flux driven by diurnal oscillations are the causes that can modify the temporal structure of temperature beyond the CTW dynamics.

Bottom temperature variability at the inshore site contains an additional effect to that in the offshore site where the temperature variability is influenced by CTWs. The inshore temperature has strong relation with the vertical shear of along-shelf current at offshore site, and the difference between the inshore and offshore sites has high correlations with the vertical shears ($r > 0.87$), representing a good geostrophic balance. Nearshore upwelling on the inshore site can be driven by offshore forcing even without the upwelling-favorable local wind stress. The ensuing temperature drops on the nearshore bottom are as significant and comparable as that induced by the upwelling-favorable along-shelf wind stress. These suggest that the offshore pressure forcing can generate (or change) the inner shelf circulation.

Keyword: subtidal temperature variability, coastal trapped wave, continental shelf, East Sea (Japan Sea)

Student number : 2001-30270

Contents

List of Figures

List of Tables

Chapter Ⅰ. Introduction

1. Background

At mid-latitudes, water temperature fluctuations of synoptic/subtidal scale spanning a few days to weeks in the stratified shelf water are associated with synoptic-scale weather patterns, i.e. variation in wind, precipitation, and air temperature [Pringle and Riser, 2003]. In the inner-shelf area, upwelling/downwelling processes generated by the along-shelf wind has been known to affect the temperature fluctuations. Especially, nearshore upwelling is an important process for the cross-shelf circulation on continental shelves, and thus plays a significant role in exchanging heat, momentum, nutrients, and pollutants between the nearshore surface and the deep waters.

After the study of the offshore Ekman transport due to local along-shelf wind forcing [Smith, 1981], this wind forcing has been considered to be a main forcing to drive coastal upwelling. However, others such as along-shelf bathymetric change [Pringle, 2002], cross-shelf wind forcing [Fewings et al., 2008], wave stress [Lentz et al., 2008], and propagation of CTWs due to the remote wind [Pringle, 2002] have been recently suggested to give rise to nearshore upwelling.

a. Wind forced coastal trapped waves

The wind affects not only the underlying area locally but also the area hundreds of kilometers away from the wind forcing remotely via coastal trapped waves (CTW) propagation along the coast [cf. Battisti and Hickey, 1984; Griffin and Middleton, 1991]. The CTW is a hybrid one of the topographic Rossby wave and Kelvin waves propagating along the continental slops and shelves of the world' coastlines that leave the coast on the right (left) in the Northern (Southern) Hemisphere (Figure I-1). The characteristics of CTW depend on the strength of stratification. That is, for the Burger

Number ($B_u = (NH / fL)^2$, where H and L are vertical and horizontal length scales, respectively and f is Coriolis parameter, N is buoyancy frequency) less than O(1), the characteristics resemble the barotropic Rossby waves (continental shelf waves), while for the opposite case they resemble the internal Kelvin waves [Allen, 1980; Brink, 1991].

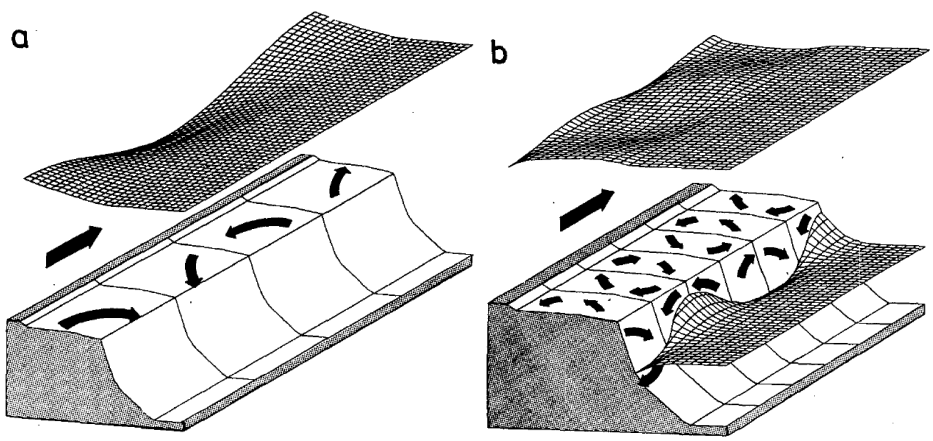

Figure I-1. CTW propagation and its related water particle movement feature in Southern Hemisphere. First mode (a) and second mode (b) structures [Griffin and Middleton, 1986]

According to Pringle and Riser [2003], the along-shelf wind at Baja California had a strong influence on the nearshore temperature at Point Loma, to the north hundreds of kilometers away from Baja California, on timescales of synoptic band or longer (a week to a year), and its propagation speed matched the phase speed of the first CTW mode. However, they just fitted the temperature fluctuation with the time-lagged wind signal that was weighted depending on the distance from temperature observation site. Jordi et al [2005] applied the CTW model (released by Chapman, 1997) to Mediterranean Sea, the semi-enclosed basin like the East Sea. They successfully

reproduced observed along-shelf current fluctuations by use of the first three CTW modes (correlation coefficient is over 0.7). A similar study was also performed for the Baltic Sea, which is the semi-enclosed basin and has the unique stratification condition having a strong halocline at a depth of 60~70m [Pizarro and Shaffer, 1998].

Subtidal fluctuations in association with the low-mode (energy-containing) CTW propagation are recently addressed. The CTW formalism can predict the time series of alongshore current and pressure, comparable to observations, but cannot expect good prediction for cross-shelf current and density (or temperature), particularly in the presence of a strong mean flow or large frictional damping [Brink, 1991]. Because of this limitation, it was difficult to reproduce the temperature variations (or demonstrate cross-shelf circulations) on the shelf area using CTW model. Therefore, analogous studies addressing temperature fluctuations based on the CTW model are very few in contrast to studies of the along-shelf currents and sea level fluctuations.

b. Coastal upwelling of non-wind origin

Besides the along-shelf wind remotely/locally driving coastal upwelling, other dynamics play a role particularly in the inner-shelf area (offshore of surf zone where the surface and bottom boundary layers interact, e.g., [Lentz, 1994]). It has been widely accepted that currents in the inner-shelf area are frictionally dominated (e.g., Mitchum et al., [1986]) with significance of wind/wave stress terms in the momentum balance [Fewings et al., 2008; Lentz et al., 2008] or are affected by the coastally-originated buoyancy forcing such as river plume [Lentz, 2004].

Offshore forcing has been hardly believed to drive or affect the inner-shelf currents. A persistent, upward motion of coastal water along their eastern boundary occurs in the left side of the northward western boundary current [Hsueh and O'brien ,1971]. Over

middle and outer continental shelves, cross-shelf pressure gradient force is balanced by the Coriolis force on the subinertial time scale [Shearman and Lentz 2003]. However, this dynamic has not been extended to the inner-shelf circulation.

Although many numerical simulations have demonstrated that the offshore current could influence shelf circulation as a form of pressure forcing, e.g., Palma et al. [2008], Weisberg and He [2003], and Gibbs et al. [1998], it is still not clear whether the response to this offshore forcing is limited to the outer-shelf or reaches the inner-shelf regime. Nevertheless, these numerical studies assert that inner-shelf currents were primarily controlled by local (both along-shelf and cross-shelf) winds, waves, alongshore bathymetric change, and buoyancy forcing.

2. Subtidal variability on the shelf area off the east coast of Korea

In the East Sea, a semi-enclosed deep (mean depth of 1700 m) basin surrounded by Korean peninsula, Japanese Islands, and Russian coast (Figure I-2), sea level fluctuations at a period band of 3-5 days have been known to be driven by non-isostatic sea level response to atmospheric pressure [Lyu et al., 2002; Nam et al., 2004]. Such sea level fluctuations had a spatial homogeneity due to rapidly propagating barotropic long waves around the basin [Lyu et al., 2002; Choi et al., 2004]. By analyzing sea level fluctuations along the east coast of Korea, Lee and Chung [1982] also reported that barotropic shelf waves propagated from north to south with phase speed of 1-3 m/s, suggesting that its travelling disturbance was generated by the atmospheric pressure fluctuations highly correlated to the changes of wind stress.

However, subtidal temperature fluctuations around the basin (presumably due to internal Kelvin waves/shelf waves or more generally wind-forced CTW) along the east

coast of Korea have not been paid attention to date, in spite of their importance. They may be significant, because strong and inhomogeneous wind variability associated with mountainous landmass in the northwestern part of the East Sea [Park et al., 2003; Nam et al., 2005a] potentially affects the variability at the same time scale along the east coast of Korea. It should be noted that the subtidal temperature fluctuations are important in understanding the background condition for the temperature fluctuations with higher frequencies (near-inertial and semi-diurnal) interacting with internal waves [Kim et al., 2001; Kim et al., 2005; Park et al., 2005; Nam and Park, 2008] as well as the coastal upwelling driven by the various forcings.

In the inner-shelf off the east coast of Korea (less than 30 m depth, defined in Figure II-2), the subtidal temperature fluctuations are somewhat different from those in the mid-shelf or offshore [Fewings et al, 2008a]. They are generated by frequent upwelling events due to the along-shelf wind [Yang, et al. 1998, Lee et al. 2003], which is supported by the cold water mass appearing at the sea surface off the east coast of Korea in every summer [Lim and Chang, 1969; An, 1974; Seung, 1974; Lee and Na, 1985; Lee et al, 2003]. A comparison among the time series of winds, coastal water temperatures, and sea levels along the southeastern coast [Lee, 1983] also supports that the subtidal temperature variations at inner-shelf area are connected with the nearshore upwelling. However, the nearshore upwelling is not confined within the wind driven one but can be generated by the other forcings. According to Lee et al. [2003], the coastal upwelling can be also induced (or affected) by the baroclinic tilting of isotherms due to offshore currents, e.g. the East Korean Warm Current as well as the southerly wind.

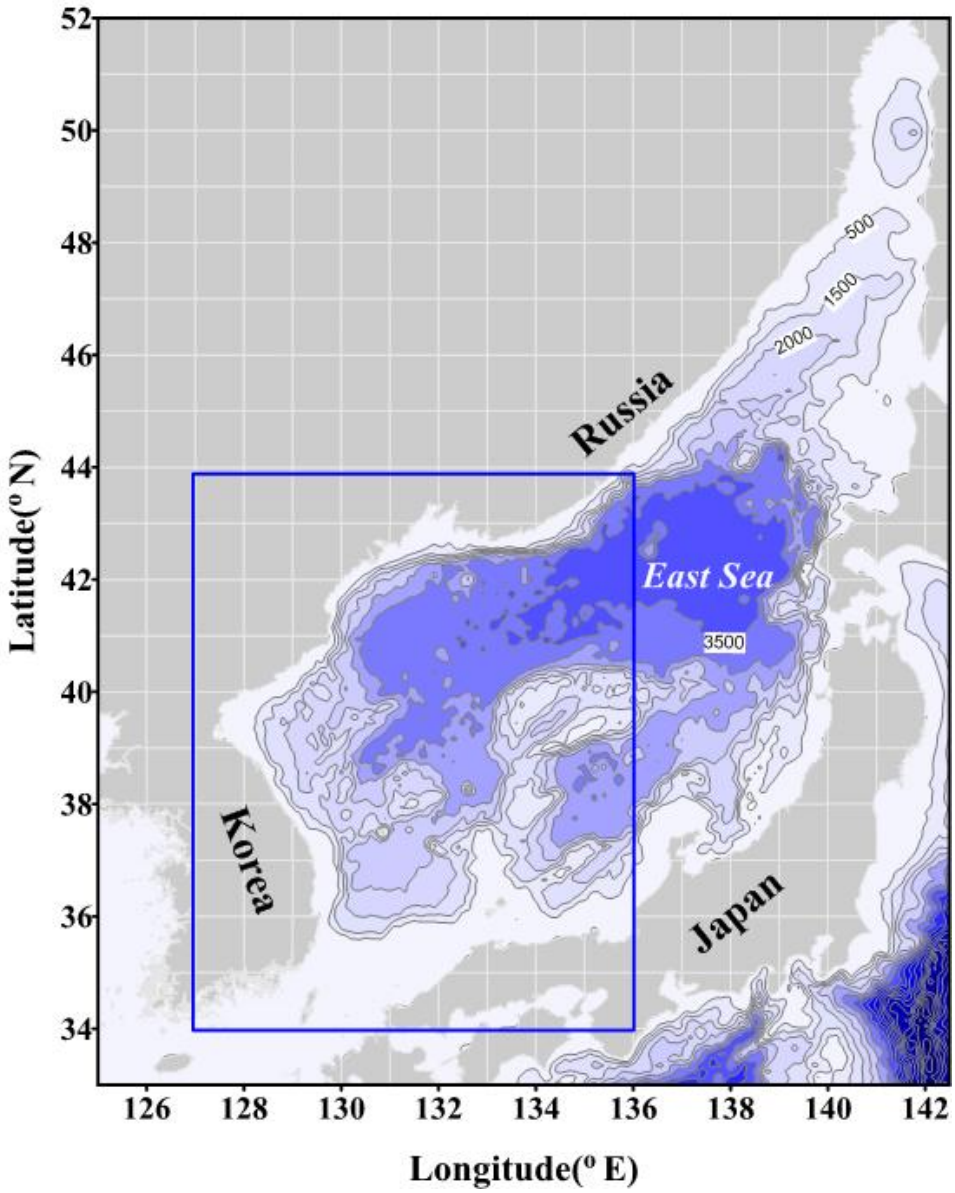

Figure I-2. Bathymetry of the East Sea (contour interval is 500 m). A semi-enclosed basin surrounded by Korea peninsula, Japanese Islands and Russian coast. The continental shelf area along the east coast of Korea within the interior box is the study area.

3. Purpose and outline

This study aims at addressing the subtidal water temperature fluctuations on the shelf area off the mid-east coast of Korea where the strong alongshore current frequently appears. Subtidal water temperature fluctuations in offshore site are examined by analyzing both observational data and results from the remotely wind-forced CTW model. In addition to CTWs dynamics, several local forcing effects leading to the subtidal water temperature fluctuations at offshore site were discussed: nonlinear heat advection, eddy heat flux due to diurnal oscillation, and abrupt downwelling event.

In the inshore area, a possible mechanism of the subtidal temperature variability (related to the inner-shelf circulation) induced by the offshore currents is suggested on the basis of observations, adding to the variation induced by CTWs. This is the first attempt to explain the detailed role of offshore forcing in inner-shelf circulation by analyzing data of current, sea level, pressure, water temperature, and salinity collected near and off the mid-east coast of Korea.

This thesis consists of eight chapters with the terminologies of the positions/areas used in this study are defined in Figure II-2, e.g. the inshore site, the offshore site, inner-shelf, mid-shelf, and outer-shelf areas. Chapter I addresses the subtidal water temperature fluctuations on the shelf area. Previous studies on the subtidal variability (of temperature, sea level, and along-shelf current) due to the coastal trapped waves are reviewed particularly in detail. The mechanisms of the inner-shelf circulations and nearshore upwelling previously documented are also summarized. Chapter II describes field experiments, ancillary data used, and pre-processing of time series data. The main data to be analyzed is acquired from the ocean monitoring buoy (deployed at 100 m

depth) and the inshore bottom mooring (27 m depth). Chapter III describes the observation results such as the propagation of sea levels and the subtidal variations of the temperature, currents, and wind stress. The theory, basic formulations and the numerical model of coastal-trapped waves (CTWs) are addressed in Chapter IV. And then, temperature fluctuations predicted by the CTW model are verified with the observed temperature fluctuations at inshore and offshore sites. There exist mismatches between the predictions and the observations, and the possible reasons for the mismatches are suggested in Chapter V. Some limitations of CTW theory are discussed, and the further works are suggested in Chapter VI followed by the summary and concluding remarks of this study in Chapter VII.

Chapter Ⅱ. Observations and Data Processing

1. Field Observations

a. Offshore observation by the ocean monitoring buoy

A real-time ocean observational buoy (surface mooring system) had been developed and applied in the study area off the coast of the mid-east coast of Korea from 1999 to 2001, where the bottom depth was about 100 m (M2 in enlarged map of Figure II-1). Since the year of 2002, the mooring position has been moved 12 km south-eastward and 30m deeper than the original location and depth (M3). This surface mooring system is equipped with meteorological sensors, five (six in 2006) Conductivity-Temperature Depth (CTD) sensors (SBE-37) and 300 kHz ADCP (RD Instrument) to collect the time series data of wind speed and direction, air pressure, air temperature, water temperature, salinity, and current velocity at selected depth levels. The data set was recorded every 10 minutes, the currents were measured at four levels from 26 to 50m depth in 1999 and twenty levels from 5 to 100 m depth in 2000 to 2001. Wind speed and direction were measured about 2 meters above the sea surface.

In this study, the data collected from March 30 to September 27 in 2001 were mainly analyzed and compared with other data including those predicted by CTW model. Measurement information of the surface mooring in 2001 is summarized in Table II-1. Table II-2 represents the observation period and the depth of CTD (SBE37 and/or SBE39 sensors) from 2006 to 2011 (the period of relatively good observational condition is maintained). These are also analyzed for comparison with the predictions by CTW model.

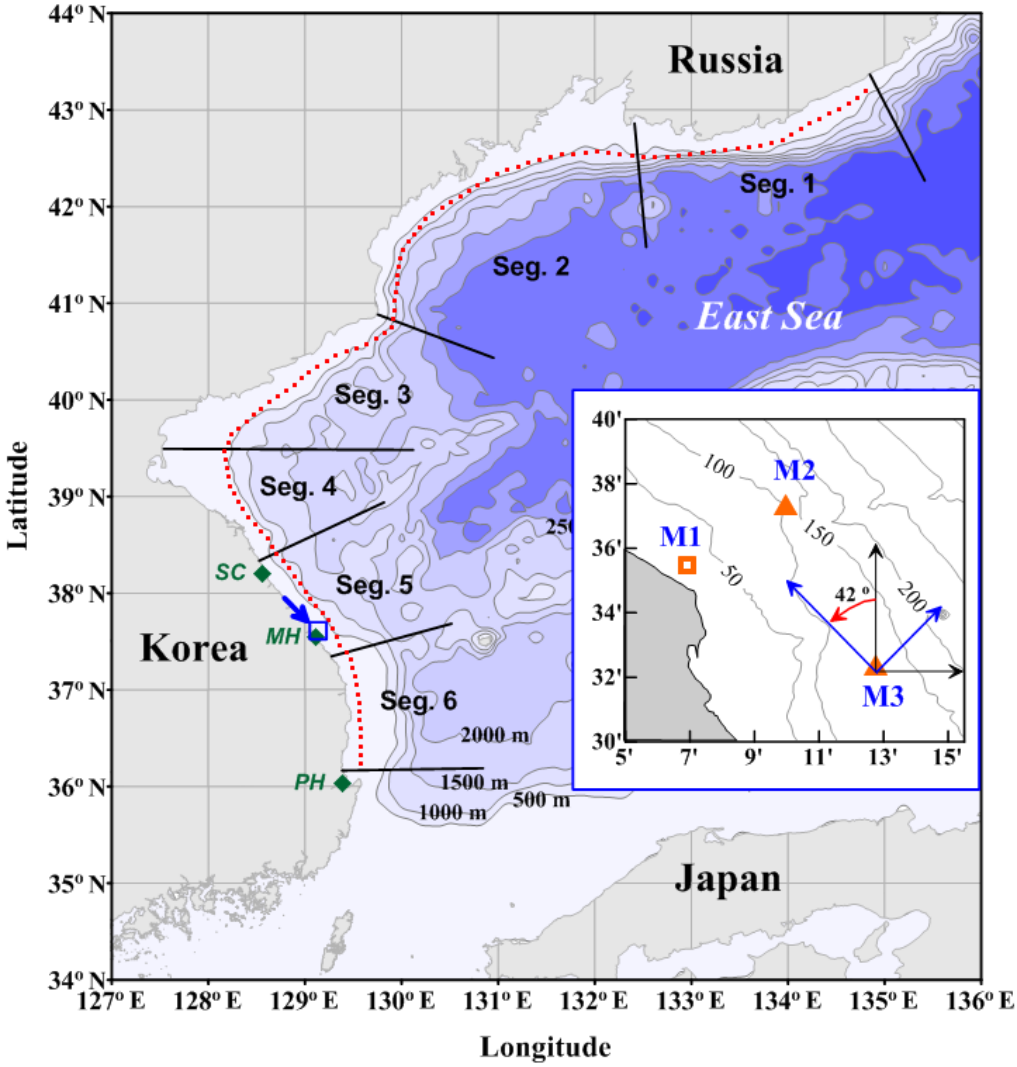

Figure II-1.A bathymetry off the east coast of Korea. Contours are depth with interval of 500 m. Positions of the tide-gauge stations (SC, MH and PH) are marked with diamond. Coastal area is divided into six segments (Seg.1 to Seg.6) according to the bathymetric features and coastline curvature. Dot line indicates the position of the wind forcing along the coast. Positions of bottom mounted mooring inshore (M1, water depth: 27 m) and the two surface mooring offshore (M2; water depth 100 m, and M3; water depth 130 m) within Seg.5 are shown in the enlarged map. Local along-shelf direction is defined to be rotated 42° anticlockwise from the north.

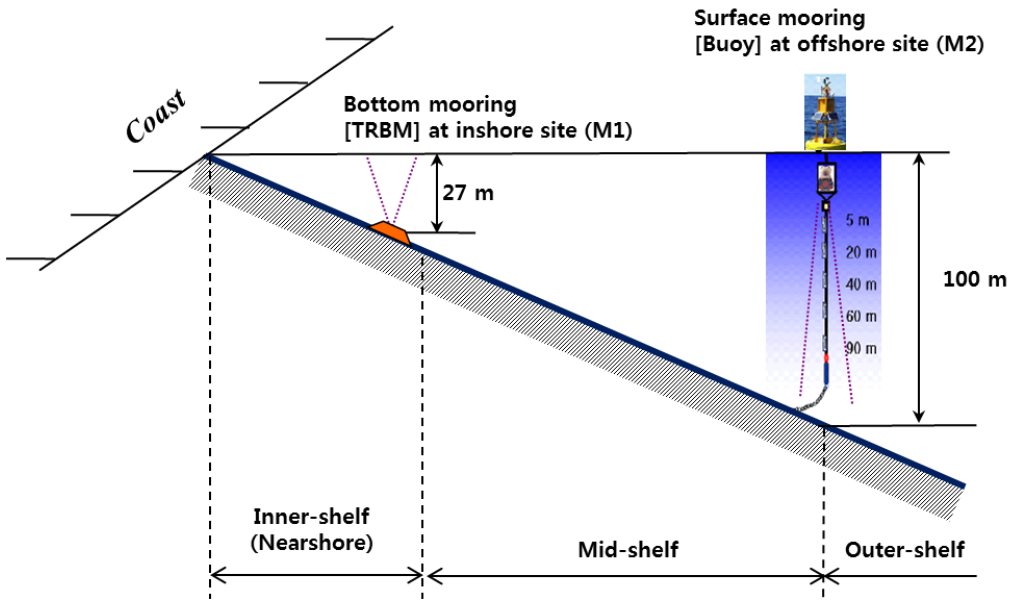

Figure II-2. Sectional design view of the observations using a surface mooring and a bottom mooring in the shelf area (enlarged map in Figure II-1). The bottom mooring (TRBM) is located within inner-shelf (M1; the inshore site) and surface mooring (Buoy) is at the offshore site (M2). The distance between the two moorings is about 5.7 km.

Table II-1. Information of data collected using surface mooring system (M2 in Figure II-1).

Observation Period		March 31~ September 25, 2001
Data	Weather	wind, humidity, air temperature Sea Surface temperature (SST)
	Current	current (5 m ~ 100 m, 5m interval)
	CTD	temperature and conductivity : 0m(T), 5m, 20m, 40m, 60m, 90m pressure : 5 m, 90 m

Table II-2. Information of CTD data collected using surface mooring system from 2006 to 2011. SBE37 had conductivity, temperature and depth sensors and SBE39 had only two sensors without conductivity (M3 in Figure II-1).

Year	Sensor/Installed depths (m)	Observation Period
2006	CTD (SBE37)/ 5, 20, 40, 60, 100, 120	Jan. 13 ~ Aug. 18 2006
2007	CTD (SBE37)/ 5, 20, 40, 60, 130	Feb. 28 ~ Apr. 15 2007 May. 6 ~ Dec. 31 2007
2008	CTD (SBE37)/ 3, 20, 40, 60, 130	Jan. 1 ~ Mar. 31 2008
	CTD (SBE39)/ 0, 1 m CTD (SBE37)/ 5, 20, 40, 60, 130	May 4 ~ Dec. 31 2008
2009	CTD (SBE39)/ 0, 1 m CTD (SBE37)/ 5, 20, 40, 60, 130	Jan. 1 ~ Aug. 30 2009 Sep. 20 ~ Dec. 31 2009
2010	CTD (SBE39)/ 0, 2 m CTD (SBE37)/ 5, 20, 40, 60, 130	Jan. 1 ~ May 27 2010
	CTD (SBE37)/5, 20, 40, 60, 110	Jul. 27 ~ Dec. 31 2010
2011	CTD (SBE37)/ 5, 20, 40, 60, 105	Apr. 15 ~ Dec. 31 2011

b. Inshore observation by the bottom mooring

A bottom mooring was deployed at the inner-shelf which was located 5.7 km coastward from the surface mooring site (M1 in Figure II-1 and Figure II-2). The depth of the inner-shelf site was 27 m, and the observation period was about four months (June 18 to September 13 in 2001), which was overlapped with the period of the observation at the offshore site. This bottom mooring system was equipped with a 1200 kHz workhorse ADCP installed in the TRBM (Trawl Resistant Bottom Mount). Through this observation, current speeds and directions were measured at every 1 m in a depth range from 5 m to 25 m. Temperature (naturally low-pass filtered temperature data was recorded from the temperature sensor within ADCP) and pressure variations were acquired at the bottom. In this study, these data were used to examine the spatio-temporal structures of water temperature and currents. Measurement information of the ADCP through the TRBM was summarized in Table II-3.

Table II-3. Information of data collected using bottom mooring system (M1 in Figure II-1 and Figure II-2).

Observation Period		June 18 ~ September 13, 2001
Data	Current	current (1 m ~ 25 m, 1m interval)
	Temperature	temperature at bottom (27 m depth)
	pressure	pressure at bottom (27 m depth)

2. Ancillary data

a. Sea level and air pressure data

Hourly sea level data were collected at three stations (SC, MH and PH in Figure II-1) from January 1 to December 31, 2001. The distance between the northern two stations (SC-MH) was about 88 km and between the two southern stations (MH-PH) was 170 km (Figure II-1). Sea levels were measured and released by KHOA (Korea Hydrographic and Oceanographic Administration) without air pressure compensation. These data were used for verifying the phase propagations of CTWs along the east coast of Korea, after the correction of the air pressure effect.

In order to remove the air pressure effect from the sea levels, the KMA (Korea Meteorological Administration) air pressure data was applied. The interval of the sea levels and air pressure was one hour. The air pressure data was checked using the observation from the surface mooring system. There was little difference between the two data sets (Figure II-3a).

b. Wind, temperature and salinity

The along-shelf wind stress is inputted as the forcing for the CTW model. The ECMWF wind data (the European Center for Medium-range Weather Forecast reanalysis wind product: ERA40) are used for the inputs of CTW model after the verification using of the observed wind. The interval of data is 6 hours and grid size is 0.5 by 0.5 degree. Low-pass filtered ECMWF wind stress is compared with the observed one from the surface mooring (Figure II-3b). The high correlation (> 0.89) of the two data sets allows us to use the ECMWF wind stress data as an input to the CTW model, in spite of a little mismatch for some periods (mid-July in Figure II-3b).

The buoyancy frequency (N^2) is another input parameter for running the CTW model. WOA2001 (http://www.nodc.noaa.gov/OC5/WOA01/woa01dat.html) temperature and salinity data is used to estimate representative buoyancy frequency profiles at each segment for three different periods (Period 1: Apr.-May, Period 2: Jun.-Jul., Period 3: Aug.-Sep.). WOA 2001 contained the temperature and salinity data for the entire of the East Sea including the coastal areas of Russian and North Korea.

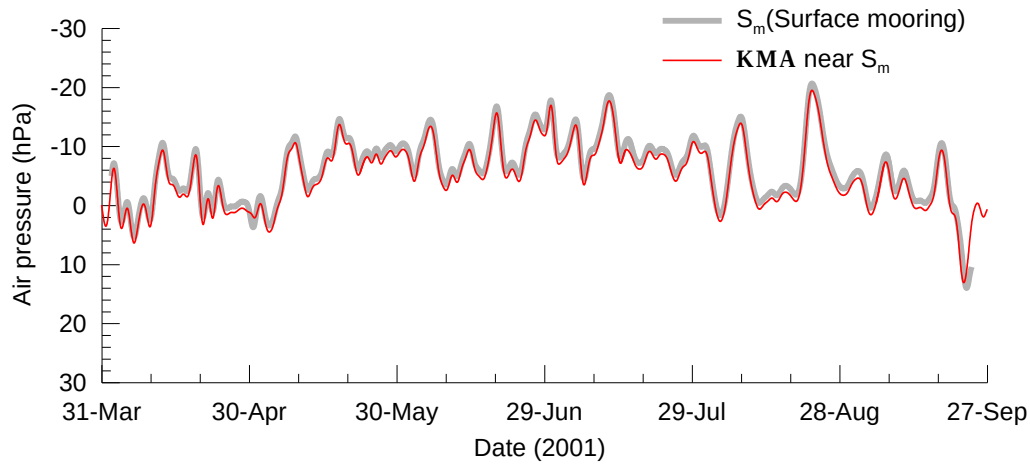

(a) Comparision of the two air pressure data sets

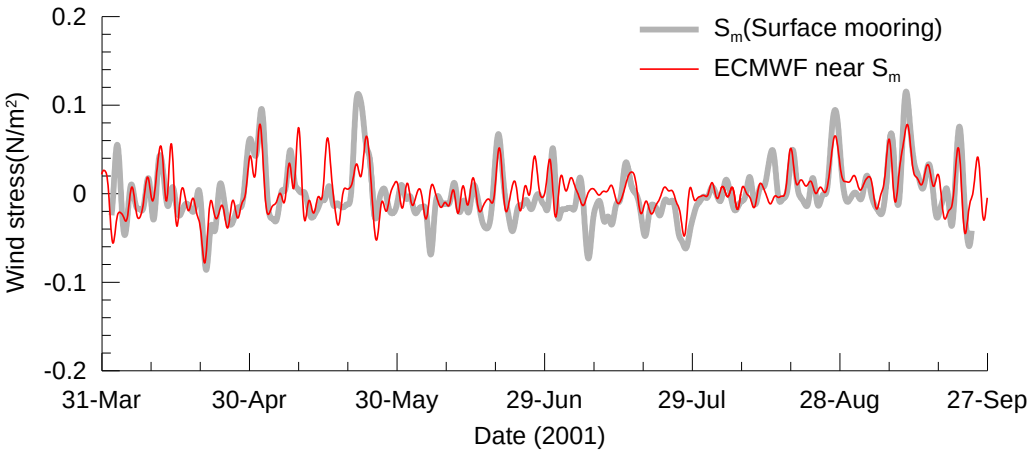

(b) Comparision of the two along-shelf wind stress data sets

Figure II-3. Comparison of the two data sets which (a) air pressure released by KMA (thin line) and observed by surface mooring system (thick gray line), (b) ECMWF along-shelf wind stress (thin line) and the observed surface mooring buoy (thick gray line) from the buoy. All data sets are low-pass filtered with 48 hours for the same period and air pressure were anomaly data from 1 atm.

3. Data processing

a. Current and wind stress

Defining the along-shelf direction as the major principal axis which was oriented 42° anticlockwise from north, roughly parallel to the local isobaths and coastline (Figure II-1), therefore current and wind stress data sets were rearranged on the basis of the main axis (along-shelf direction) and its orthogonal parts. For the case of along-shelf wind stress, positive sign represented the upwelling-favorable. Horizontal current vector at each depth level and position (inshore and offshore in Figure II-1) was separated into the along-shelf (*y*) and cross-shelf (*x*) components (Figure II-1). This coordinate system is only for the observed data processing in the mid-east coast of Korea (M1, M2, and M3 in Figure II-1).

ECMWF wind data were interpolated along the coast line with 10 km horizontal interval using the objective analysis method [Lyu, 2005], and rearranged with 1/10 day time interval using the Akima Cubic-spline interpolation method (red dots in Figure II-1). Wind stress was calculated from the along-shelf and cross-shelf wind data using a simple quadratic formula i.e. $\vec{\tau} = C_D \rho_{air} |\vec{W}| \vec{W}$, where the constant drag coefficient $C_D = 1.4 \times 10^{-3}$ and ρ_{air} is air density [Pond and Pickard, 1983]. The along-shelf directions of ECMWF wind stress were not same with the definition in the enlarged map of Figure II-1. In order to be used as a forcing for CTW model, the component of upwelling/downwelling-favorable wind stress was calculated at each position (red dots in Figure II-1). Therefore the ECMWF wind stress data were redefined as downwelling (upwelling)-favorable with positive (negative) at each point along the coast line as shown in Figure II-4. The along-shelf components of ECMWF wind stress along the

east coast of Korea were represented in Figure II-5. The x-axis is the distance (km) form the inshore site (M2) and y-axis is time (days) from late March to September in 2001.

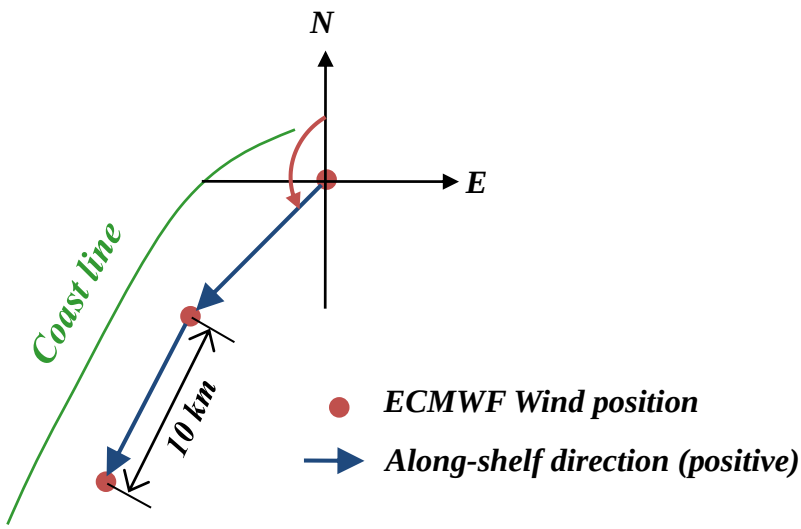

Figure II-4. Schematic of the definition of the along-shelf directions at the interpolated ECMWF wind stress positions. In this figure, south-westward component of the wind is considered as a positive value. The distance of the every two neighbored positions is 10 km.

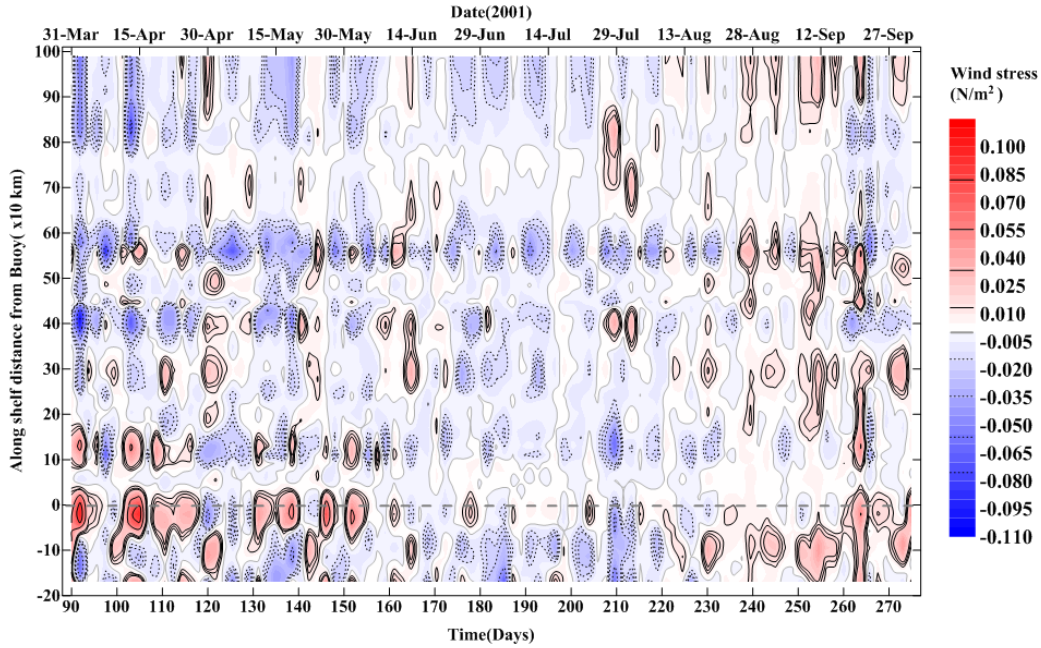

Figure II-5 The along-shelf component of the ECMWF wind stress along the east coast of Korea. The positive sign is downwelling-favorable wind stress. Dashed line means the surface mooring position (St. M2).

b. Sea levels

Diurnal and semidiurnal signals peaked at spectrum analysis of sea level time series data (Figure II-6). For taking into account to the subtidal/synoptic band fluctuations of sea levels, the data have been low-pass (48 hours, same as current and wind stress data) filtered. In general, the cutoff frequency of sub-inertial low-passed filter was 1/30 hours, but in order to make sure to eliminate all the high frequency signals, 1/48 hours was taken for the cutoff frequency for low-passed filter. There is no remarkable peak in the subtidal frequencies but weak concentrations of spectral density around 100 hours (Pohang) and 200 hours (Sokcho and Mukho).

In a semi-enclosed sea like the East Sea, sea level might not respond isostatically because such marginal seas are connected to open oceans through narrow straits [Lyu et al., 2002; Lyu and Kim, 2005]. The sea level response of the realistic East Sea to the idealized forcing varies with geographical location and shows zonally asymmetric variations in amplitude and phase [Inazu et al, 2005]. The results (the amplitudes compensate rate and the time lags in the East Sea) from the study of Inazu et al [2005] were used to correct the sea level data. The sea levels at SC, MH and PH were invers barometrically compensated with 0.7 cm/hPa, and the sea level phase responses at the site SC, MH and PH were delayed 3, 4 and 5 hours to the local air pressure variations respectively.

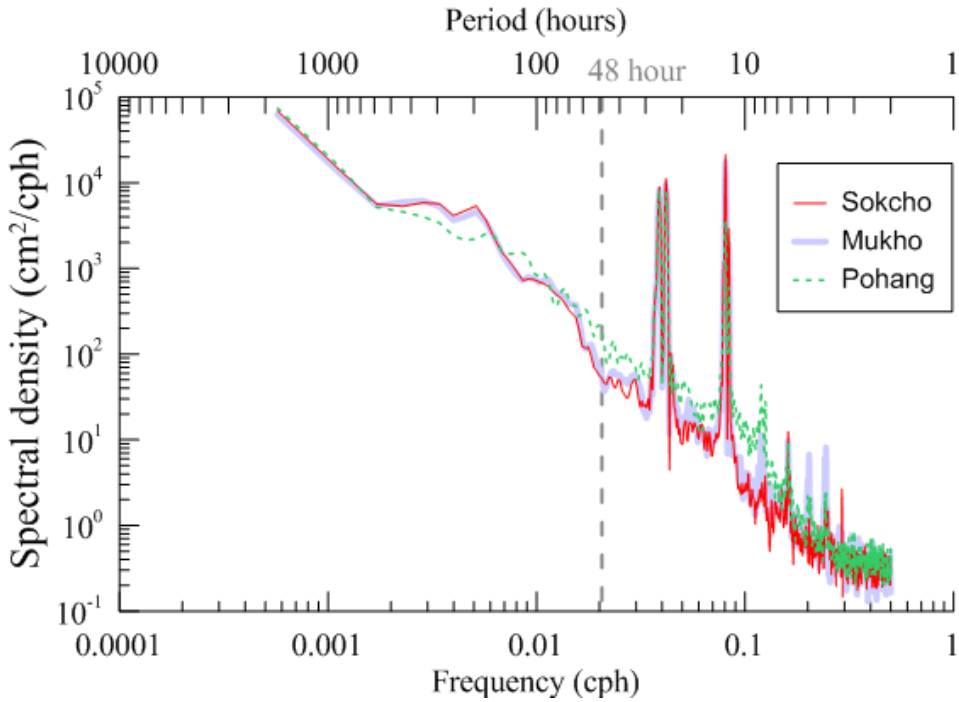

Figure II-6 Auto-spectra of sea level elevations at Sokcho, Mukho and Pohang along the east coast of Korea.

Chapter Ⅲ. Results of observations

1. Propagation of sea levels along the east coast of Korea

The wave like signals with the periods of 3 ~ 5 days seem to propagate from SC to PH via MH in the low-pass filtered sea level variations (Figure III-1a and b). Subtidal sea level fluctuations (after correcting the barometric effect) show the southward phase propagations along the coast from SC to PH with a speed of a few to tens of m/s (Table III-1). Time lags of the sea level fluctuations between SC and MH and between MH and PH are 3-5 and 7-10 hours in April, and 7-9 and 8-18 hours in September, respectively (Figure III-1b). Maximum correlation for the total period from spring to summer 2001 is found at the time lag of 4 hours between SC and MH (distance: 88 km) and 4.5 hours between MH and PH (distance 170 km), yielding phase speeds of 6.1 and 10.4 m/s, respectively (Table III-1 and Figure III-1c).

Table III-1. Propagation speeds of the subtidal sea level fluctuations observed between SC and MH (in Seg.5) and between MH and PH (in Seg.6) along the coast for three periods.

	Distance (km)	Propagation speed (m/s)			
		Period 1 (Apr. to May)	Period 2 (Jun. to Jul.)	Period 3 (Aug. to Sep.)	Total period (Apr. to Sep.)
SC-MH	88	8.2	6.1	6.1	6.1
MH-PH	170	11.7	15.6	7.8	10.4

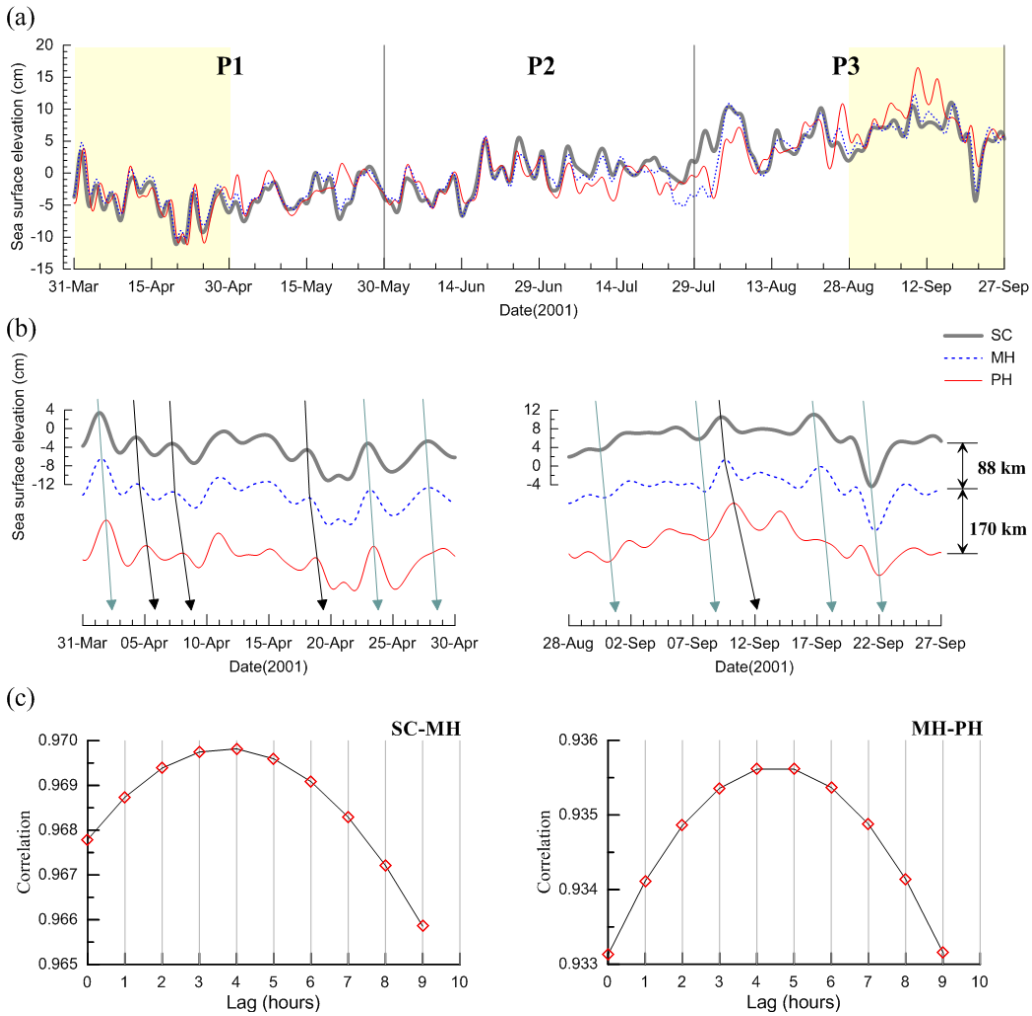

Figure III-1. (a) Subtidal sea level fluctuations (after correcting atmospheric pressure loading effect) from Mar. 31 to Sep. 27. 30, 2001, (b-left) from Mar. 31 to Apr. 30, 2001, and (b-right) from Aug. 28 to Sep. 27 at tide-gauge stations SC (thick gray line), MH (thin dashed blue line), and PH (thin red line). Distances between SC and MH (88 km) and between MH and PH (170 km) along the coast are shown in right. P1 to P3 in the top panel denote the three different periods/seasons (Apr. & May, Jun. & Jul, and Aug. & Sep). Southward propagations are shown with arrows in bottom panels. And (c) is lagged correlations between SC and MH (left), and MH and PH (right).

2. Fluctuations of wind, currents, temperature and salinity at offshore site

Using the surface mooring system at offshore station (M2 in Figure II-1), the time series data (wind stress, current, temperature, and salinity) are obtained, and the data are presented synchronously in Figure III-2, after filtering low-passed. Upwelling-favorable wind stress is appeared during June and July (Figure III-2a). The magnitudes of upwelling-favorable wind stress are smaller than those of downwelling-favorable.

Horizontal currents observed at the surface mooring are primarily polarized into the along-shelf direction, and vertical shears of the currents are strongly enhanced in July and August 2001 when the local winds are mild (magnitude of wind stress is typically less than 0.1 N/m2). Four event periods are defined as the 15-day-long periods of strong along-shelf currents and associated enhancement of the vertical shear (N1 to S2 in Figure III-2c). Both along-shelf and cross-shelf currents are strong (> 30 cm/s) at the upper depths (less than 20 m) during N1 and N2, whereas only along-shelf currents are remarkably strong in S1 and S2 (Figure III-2b and c).

High salinity water (>34.2 psu) is appeared with the start of event N1, accompanying low salinity water (<33.0) at surface (5m depth). The temperature varied at the subtidal frequency and increased gradually, but there is an interruption just after July 29, during 5 days. In this period, cooling occurred at whole depths. After the end of the cooling, it gets warming and the salinity becomes lower (red arrows in Figure III-2d and e). The strong upwelling-favorable wind appears just before July 29, but magnitude of the wind stress is not enough to change the temperature compared to other period's wind forcing. It is need to be explained reasonably the unchanged (or weakly changed) temperature in spite of the strong northward current in July as well as

a sudden drop and restoring of temperature at the end of July. Particularly, the fluctuations of temperature, currents, and salinity at the near bottom (the third black arrow in Figure III-2c and the red arrows in Figure III-2d and 2e) are the uncommon features to be more investigated in this study area.

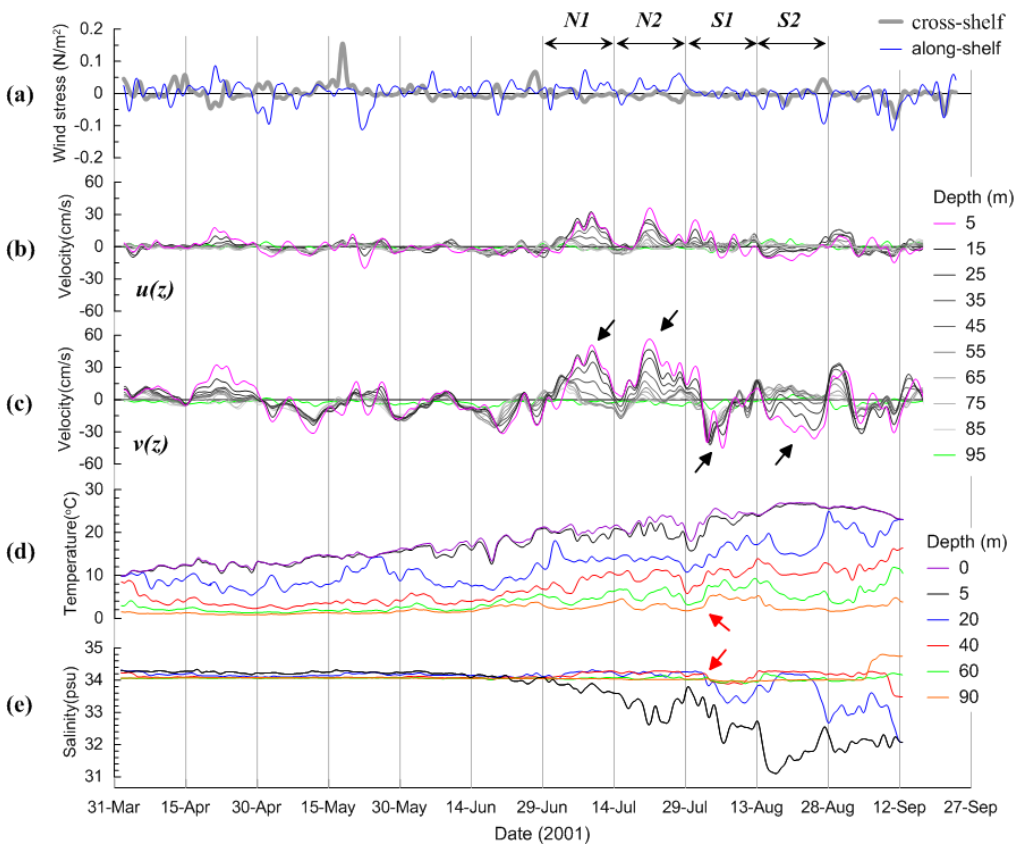

Figure III-2 Time series data of (a) along-shelf (blue) and cross-shelf (gray) wind stresses, (b) cross-shelf and (c) along-shelf currents at ten different depths shown in the right, (d) temperatures at six different depths shown in the right, and (e) salinities at the five depths (no surface salinity). Periods of strong vertical shear of along-shelf currents are highlighted with arrows in (c). Event names; northward (N1 and N2) and southward (S1 and S2) currents are shown in the top.

3. Temperature fluctuations at inshore site

Bottom temperature and current were measured at inshore mooring station (27 m depth) with the time interval of 10 minutes from June 18 to September 13, 2001 (M1 in Figure II-1 and Figure II-2). The bottom temperature was observed with the state of the low-pass filtered, because the temperature sensor was installed within TRBM housing, so the temperature sensor responded smoothly to the change of environmental temperature fluctuations with a bit time delay. But it was worth enough to be used for the comparison with other observed data with the restrictions of subtidal frequency.

In order to quantify the horizontal difference of temperature between inshore and offshore stations, temperature variations at the offshore-same depth (27 m) is interpolated, using the data observed at offshore station (blue dashed line in Figure III-3b).

The horizontal difference (green dashed line in Figure-3b) between the two temperature data sets (inshore and offshore) have a good correlation (correlation coefficient: 0.87 with 95% confidence) with the depth averaged vertical shear of along-shelf currents at offshore station (Figure III-3b). This strong relation implies that there is working of the geostrophic balance between the horizontal temperature (or density) difference ($\partial T / \partial x$) and the vertical shear of along-shelf current ($\partial v / \partial z$) at offshore area. This balance of geostrophy is valid even when the temperature eventually decreased with the range from 3 to 5 ^{o}C at inshore bottom (red line in Figure III-3b).

Although the correlation of the two temperature variations (inshore and offshore) was also high (> 0.81; this correlation might be including the seasonal trend), there were some visible differences between them, and four times cooling events were obviously separated at inshore bottom (arrows in Figure III-3b). The period of the

discrepancies of temperatures between inshore and offshore was coincided with the period, when the northward currents became stronger (N1 and N2 in Figure III-2c). During the cooling events at inshore bottom, the sea level also decreased at inshore surface, however, that in the coast (Mukho) didn't decrease rather than increased during the first two cooling event periods. This was not the general relation between the near-shore cooling and the coastal sea level changes induced by the along-shelf wind forcing. Therefore, the cooling of bottom water mass inshore (or increasing of sea level at coast) without the along-shelf wind is necessary to be explained.

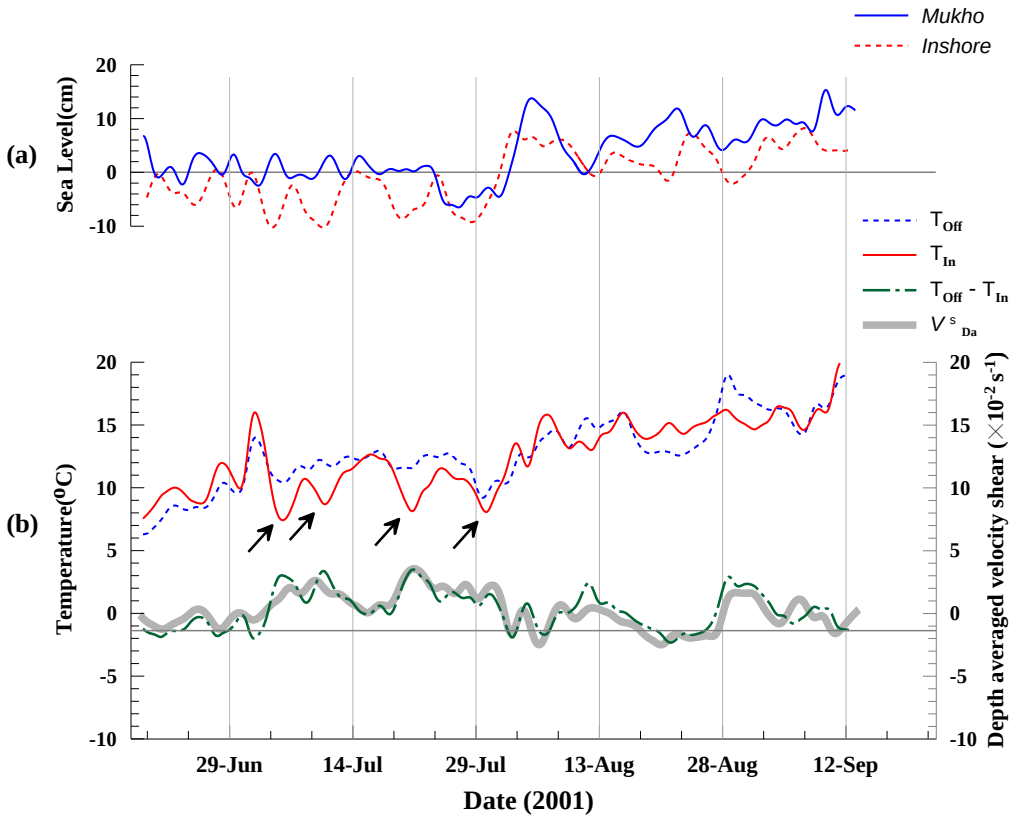

Figure III-3 (a) Low-pass filtered time series of sea level at the inshore station and at coast (Mukho). (b) Comparison of depth averaged vertical shear of along-shelf current at offshore with the horizontal temperature difference between inshore and offshore at the same depth. Notice the out of phases between the sea levels at inshore station and at Mukho before July 14 in (a).

4. Diurnal oscillations

Although this study is concentrated on the subtidal temperature fluctuations, those of inertial and tidal band were also important subjects in this study area. This is the reason why so many studies have been carried out related to the inertial/tidal periodic variations [Kim et al., 2001; Kim et al., 2005; Park et al., 2005; Nam and Park, 2008]. Moreover, the heat flux due to the diurnal oscillations of temperature and currents is often believed to give rise to change the lower frequency fluctuations of temperature [Nam and Send, 2013]. Wavelet analysis is a useful method for analyzing localized variations of power within a time series, by decomposing a time series into time–frequency space [Torrence and Compo, 1998].

The strengths of inertial and diurnal band (IDB) of the observed data are investigated by use of the wavelet analysis tool (Figure III-4). The diurnal oscillations of the along-shelf wind are amplified in mid-May and August-September. Particularly, in the mid-May, the strong oscillations of wind have lasted 15-days, and the similar peaks are observed in the cross-shelf currents (solid line in Figure III-4b). The amplification of the cross-shelf winds are more frequently appeared in the early April, late April, mid-May, and early July in the basis of the 95% confidence level. However, during the event periods (N1 to S2), the diurnal oscillations are relatively small in both directions (along-shelf and cross-shelf).

The depth-averaged along-shelf currents have a striking peak in the event S1 (dot line in Figure V-4b). The cross-shelf currents also become strong at that time, but it is not alone. There are several peaks with the similar amplitude in the cross-shelf component. The peak (within S1) is also found in the temperature variations recorded at 90 m depth (black thick line in Figure III-4d). During the S1 and S2 periods, there

are 2~4 day periodic oscillations as well as the diurnal one in the 90 m depth (Figure III-4c).

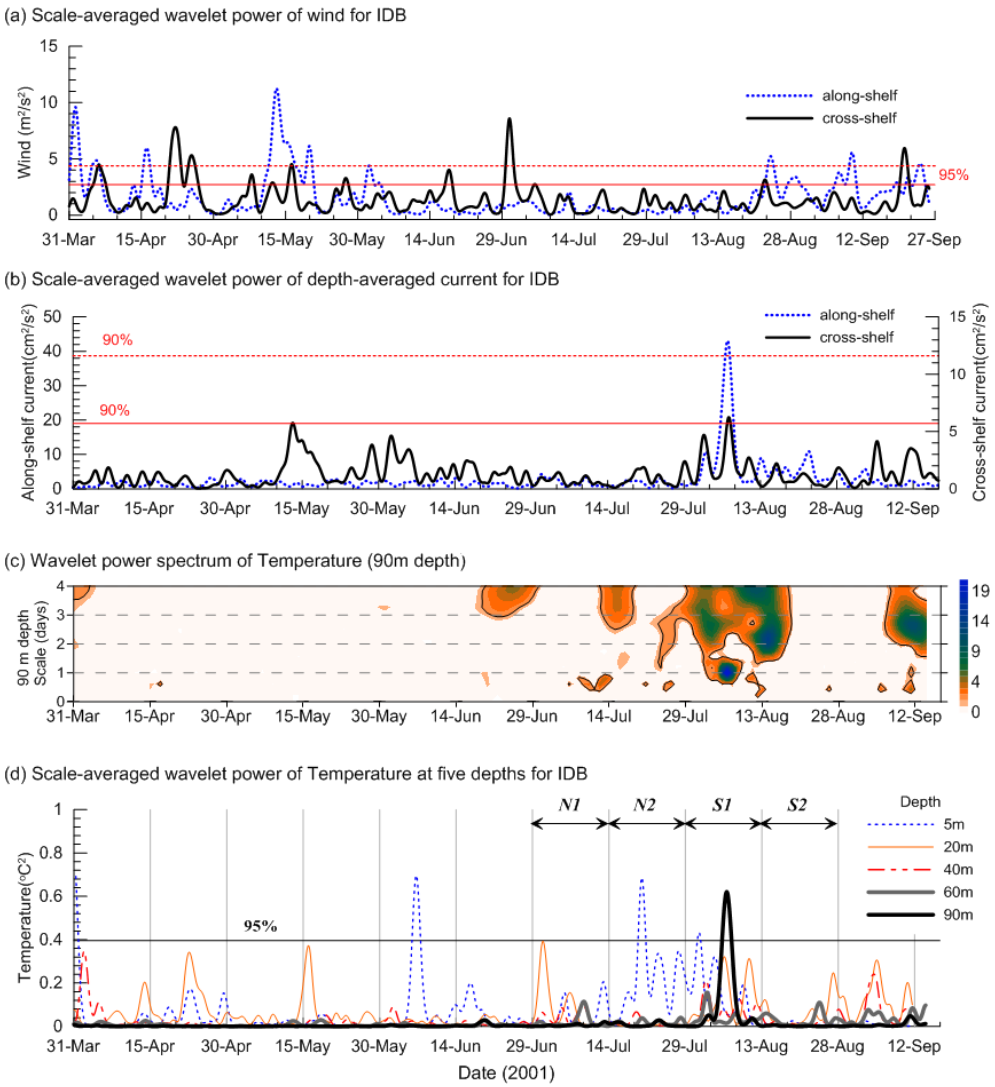

Figure III-4. (a) Scale-averaged wavelet power over the IDB (0.79 ~ 1.17 day) of wind, (b) Scale-averaged wavelet power over the IDB of depth averaged current, (c) wavelet power spectrum of temperature at 90m depth and (d) Scale-averaged wavelet power over the IDB of temperature at five depths (5, 20, 40, 60 and 90m). The confidence lines in (a) and (b) indicate 95% and 90 % levels for each wavelet power respectably. The 95 % confidence line in (d) is only for the temperature at 90 m depth, those in the others depths are less than 95% confidence levels (not shown because the lines exceed the range of y-axis).

Chapter Ⅳ. Subtidal water temperature fluctuations driven by CTWs

1. Coastal trapped wave model

Many phenomena induced by wind forcing over the continental margin can be explained in terms of the properties of coastal-trapped waves (CTWs). Most of the continental shelves around the world allow the existence of the CTWs. The areas are including the along the coastal area of the semi-closed basin like the East Sea. The CTWs generally have periods longer than the inertial period, so that they often play a role in the response of the ocean to atmospheric weather changes [Huthnance et al, 1986; Brink, 1991]. Therefore, CTWs should be considered when the subtidal/synoptic band variability in the shelf area is studied.

a. formulation

The problem of CTWs is formulated in the arbitrary geometry (Figure IV-1). The governing equations are bellows

$$\left.\begin{aligned}
&\varepsilon\frac{\partial U}{\partial t} - fV = -\frac{1}{\rho}\frac{\partial P}{\partial x}\\
&\frac{\partial V}{\partial t} + fU = -\frac{1}{\rho}\frac{\partial P}{\partial y}\\
&0 = -\frac{\partial P}{\partial z} - g\rho\\
&\frac{\partial U}{\partial x} + \frac{\partial V}{\partial y} + \frac{\partial W}{\partial z} = 0\\
&\frac{\partial \rho}{\partial t} + W\frac{\partial \rho_0}{\partial z} = 0
\end{aligned}\right\} \text{---------- (4-1)}$$

The variables *U, V* and *W* are the velocity components in the *x*, *y*, and *z* directions, respectively. The Coriolis parameter is *f*, the acceleration due to gravity is *g*, and the pressure perturbation is *p*. Density is defined by $\widehat{\rho} = \rho_0(z) + \rho(x, y, z, t)$.

The Boussinesq approximation is made throughout. The quantity ε is set to either 0 (long wave approximation) or 1 (general frequency and wavenumber). In this study, the long wave approximation is applied. This long wave limit allows the simplification of the problem, where the along-shelf scales are large relative to cross-shelf scales and where frequencies are low ($\frac{\partial^2}{\partial t^2} << f^2$).

The coordinate system used in the CTW model is shown in Figure IV-1, such that the coast lies at x = 0. The along-shelf coordinate is y and the vertical coordinate is z (positive upwards), such that z = 0 at the ocean surface.

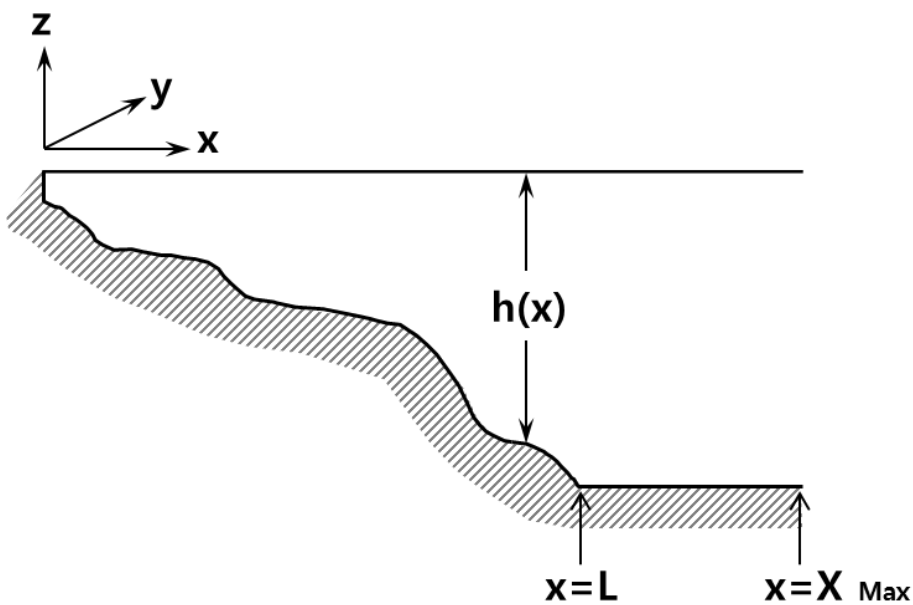

Figure IV-1. Topography and coordinate system used in the CTW model. [Brink, 1985]

All variables are taken to vary as $e^{i(\omega t + ly)}$, so that equations (4-1) reduce to

$$0 = \frac{\partial^2 P}{\partial x^2} + \frac{2f\beta}{(f^2 - \varepsilon\omega^2)}\frac{\partial P}{\partial x} - P\left[-\varepsilon l^2 + \frac{l\beta}{\omega} - \frac{2f^2\beta l}{\omega(f^2 - \varepsilon\omega^2)}\right] + \left(f^2 - \varepsilon\omega^2\right)\frac{\partial}{\partial z}\left(\frac{\partial P}{\partial z}N^2\right)$$

subject to the boundary conditions

$$\frac{\partial P}{\partial z} + \delta\frac{N^2}{g}P = 0 \quad at \quad z = 0$$

$$W + \frac{\partial h}{\partial z}U = 0 \quad at \quad z = -h(x)$$

$$U = 0 \quad at \quad x = 0$$

$$\frac{\partial U}{\partial x} = 0 \quad at \quad x = x_{\max}$$

where, N is the buoyancy frequency, ω is frequency, and l is the along-shelf wavenumber.

The fourth boundary condition [Brink, 1982] replaces the more desirable P bounded as $x \to \infty$, which is not very practical on a finite difference grid. The parameter δ is either 0 (rigid lid surface) or 1 (free surface) at the user's discretion. In this study, the model running is only for the case of free surface and fixed β.

The solution of pressures (p) can be written as

$$p(x, y, z, t) = \phi_n(y, t)F_n(x, z)$$

where F_n are the free CTW modal structures, and the amplitudes ϕ_n are can be represented as

$$\frac{\partial \phi_n}{\partial t} - c_n\frac{\partial \phi_n}{\partial y} = 0 \ .$$

The eigenvalue of the problem is now c_n and members of the complete set of eigenfunctions are F_n.

It is straightforward in the long-wave limit to solve for the wind-forced problem (with no bottom stress). Further, it is frequently assumed that forcing is only through an alongshore wind stress that does not vary in the cross-shelf direction [$\tau^x = 0,\ \tau^y = \tau^y(y,t)$]. In this case, the pressure can still be expressed in terms of the eigenfunctions,

$$P(x,y,z,t) = \sum_n F_n(x,z)\phi_n(y,t) \qquad \text{---------- (4-2)}$$

where now the amplitude functions obey

$$\frac{\partial \phi_n}{\partial t} - c_n^{-1}\frac{\partial \phi_n}{\partial y} = b_n \tau^y$$

Here , τ^y is the alongshore wind stress at the surface, and b_n is the coupling coefficient of mode *n* to the wind stress .

Most work on the excitation of coastal-trapped waves, however, has concentrated on wind-forced motions in the long-wave limit (e.g. Gill & Schumann 1974). Restriction to this limit is superficially quite reasonable because of the large scales of weather systems and because of the relatively short onshore-offshore scales of the continental margin. Given this assumption, along with the absence of a mean alongshore flows, the free coastal-trapped-wave modes have the convenient orthogonal property

$$\frac{\partial \phi_n}{\partial t} - c_n^{-1}\frac{\partial \phi_n}{\partial y} + \sum_m a_{nm}\phi_m = b_n \tau^y \qquad \text{---------- (4-3)}$$

where a_{nm} is the frictional coupling to mode *m*, and defined as contained the bottom friction (*r(x)*)

$$a_{nm} = \frac{1}{f}\int_0^{\infty} F_n(x,-h)\{r(x)\cdot[F_m(x,-h)]_x\}_x]dx + \frac{1}{f}\int_{-h}^{0}\left.\frac{F_n(x,z)[F_m(x,z)]_x r(x)}{h(x)}\right|_{x=0} dz$$

$$b_n = \frac{1}{h(0)}\int_{-h}^{0} F_n(0,z)dz$$

The b_n is related to the F_n at a vertical coastal wall at $x=0$. In the limit of weak friction, the equations given by (4-3) become uncoupled at lowest order, and a_{nm} can be thought of as an inverse-decay distance for the force wave. The physical mechanism for the wave forcing is straightforward. An along-shelf wind stress causes an onshore-offshore transport within the surface Ekman layer. In order to conserve mass, a compensating offshore onshore flow must take place at greater depth. As this flow crosses isobaths, vortex stretching leads to changes in the local relative vorticity. This vorticity is expressed largely in terms of the alongshore velocity and, in the presence of alongshore variability ($\partial/\partial y \neq 0$), gives rise to wave propagation [Brink, 1982].

b. Applying procedure

In addition to the limitations imposed by the long wave theory itself, numerous choices and decisions should be made in order to apply the coastal trapped wave theory to a realistic situation. The application process follows a flow chart in Figure IV-2. This flow diagram was originally suggested by Chapman in 1989, and some parts were modified in this thesis by adding 1) the scattering effects and 2) comparison with the observations in the real ocean. All decisions made following this flow chart have the potential of affecting the model predictions, the comparisons with observations, and hence the interpretations of the model results. The procedure in this flow chart is divided into four parts, the first part is the preparations of the input parameters, and the second one is the CTW model running so that seeking the modal structures and finding

the parameters for each mode, the predictions of the fluctuations of the oceanographic variables are conducted in the third phase using the output parameters from the model and the prepared wind forcing, and the last works are the comparison with observed data. The detailed procedures in each part are explained separately in the following sections.

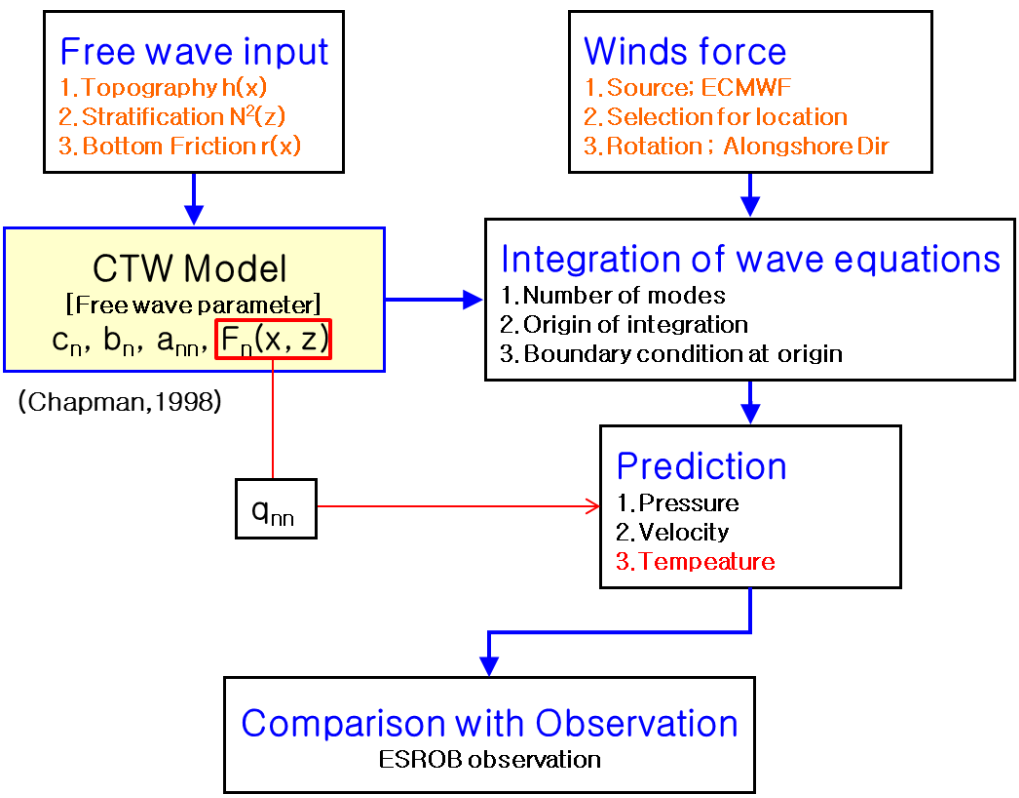

Figure IV-2. The flow diagram illustrates the procedure for applying the long wave CTW theory to realistic ocean and comparison process. This CTW model application process is modified (add scattering effect) based on that suggested by Chapman in 1989.

2. Application to the shelf area off the east coast of Korea

a. Preparation of the input parameters for running the CTW model

For computing the modal structures (F_n) and the parameters of CTWs propagations (a_{nn}, b_n, and c_n) along the east coast of Korea, the numerical model released by Brink and Chapman was used. This model had been several times upgraded since the first release in 1985. The program was run using the shelf topography for the six cross-sections (Figure IV-3) with the vertical coastal walls of 30 m depth and $N(z)$ profiles calculated from the WOA2001 (temperature and salinity data). The maximum distance of the propagations of CTWs is 1,010 km from the starting point (North-Eastern edge of segment 1 where y=1,010 km) to the surface mooring position (y=0) along the east coast of Korea (Figure II-1).

Besides the two initial conditions (the simplified bottom topography and the buoyancy frequency profile), the idealized bottom friction coefficient is needed for running the CTW model. The bottom friction ($r(x)$) is applied as a function of cross-shelf distance from the coast. In the previous studies, the various bottom friction coefficients (0.05 ~ 0.2) have been applied and checked the sensitivities to the results of CTW model. And, it was shown that the effects of the bottom friction could be negligible compared to the other items, e.g. the stratification condition and the bottom topography [Jordi et al, 2005].

b. Topography and buoyancy frequency

Coastal areas in the western margin of the East Sea were divided into six segments (Seg.1 to Seg.6) to represent along-shelf structures and changes in shelf topography as shown in Figure II-2.

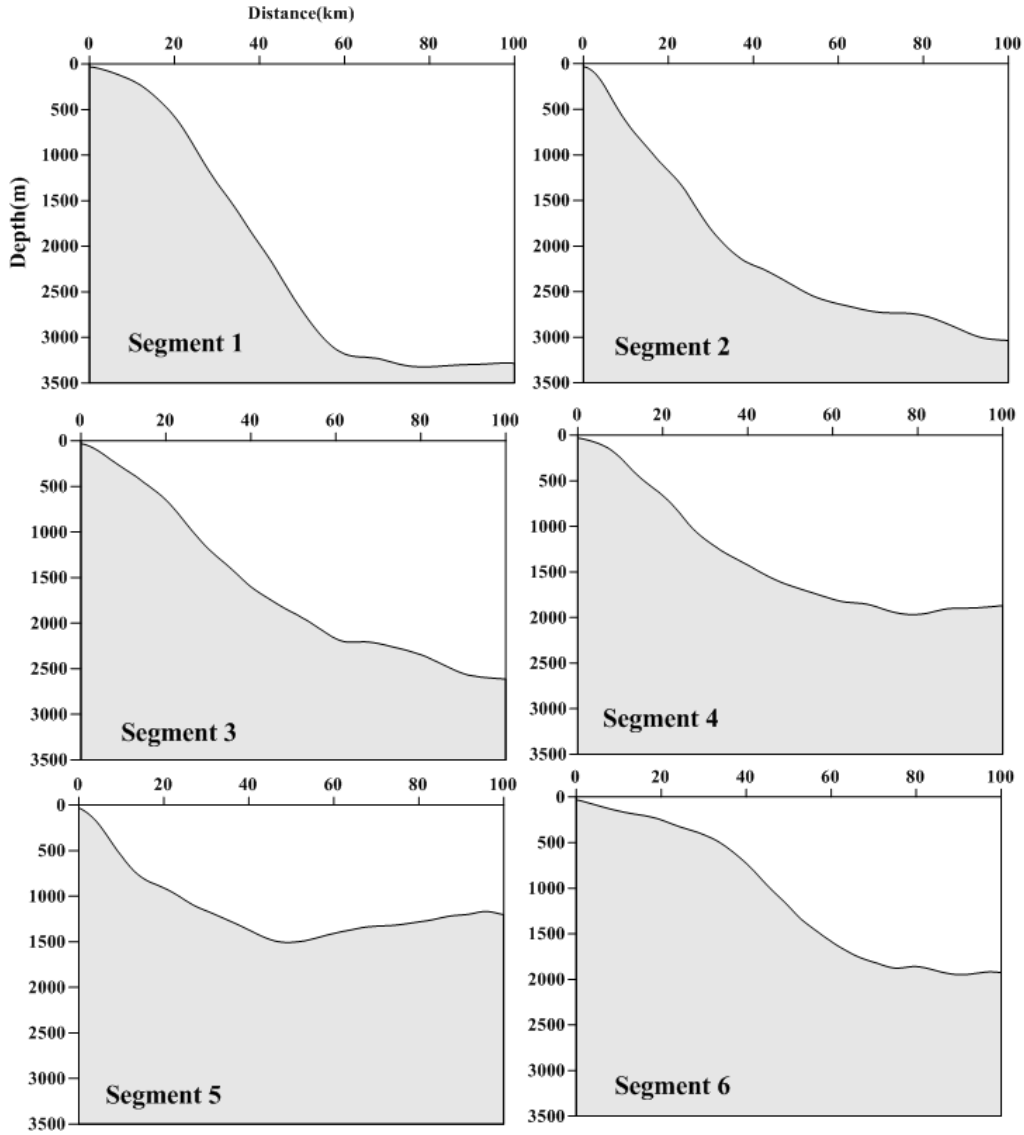

Figure IV-3. Topographies of six segments as for input data to run the CTW model. The distance from the coast is 100 km but in running the model, the full domain of the cross-shelf direction is 200 km. In the model, the topography of the seaward last 100 km is considered as flat with the depth of the deepest one at the each segment.

In each segment, the representative shelf topography was obtained by averaging eight to fourteen cross-sectional bathymetries from ETOPO2 (http://www.ngdc. noaa.gov/mgg/fliers /06mgg01.html) (Figure IV- 3).

The offshore distance from the coast is 100 km. This is arbitrarily chosen under the assumptions; both of 1) influence of wind forcing farther than the along-shelf separation, and 2) influence of shelf topography offshore of cross-shelf separation, can be neglected. The results are not sensitive to the choice of domain of integration within reasonable ranges, where the along-shelf scales are large relative to cross-shelf scales.

The northern three segments have the relatively narrow continental shelf and deepened over 2,000 m at the distance less than 40 ~ 50 km apart from the coast. The continental shelves have better developed in the southern three segments than the northern parts, and the maximum depths of southern parts do not reach to 2,000 m, even at the offshore edges. These sectional bathymetries varying with the distance from the coast contribute to the results of CTW model, e.g. modal structures and phase speeds of the CTWs.

Together with the bottom topography, the stratifications (the profiles of bouncy frequencies) are the main decision makers of the modal structures and the characteristics of CTWs. The choice of a stratification profile $N^2(z)$ for each segment poses considerable difficulties in the model. WOA2001 (http://www.nodc.noaa.gov/OC5 /WOA01/woa01dat.html) temperature and salinity data were used to estimate representative buoyancy frequency (N^2) profiles for each segment and the three different periods (Period 1: Apr.-May, Period 2: Jun.-Jul., Period 3: Aug.-Sep.). When $N^2(z)$ is not available from surface to bottom, an exponential extrapolation was used like

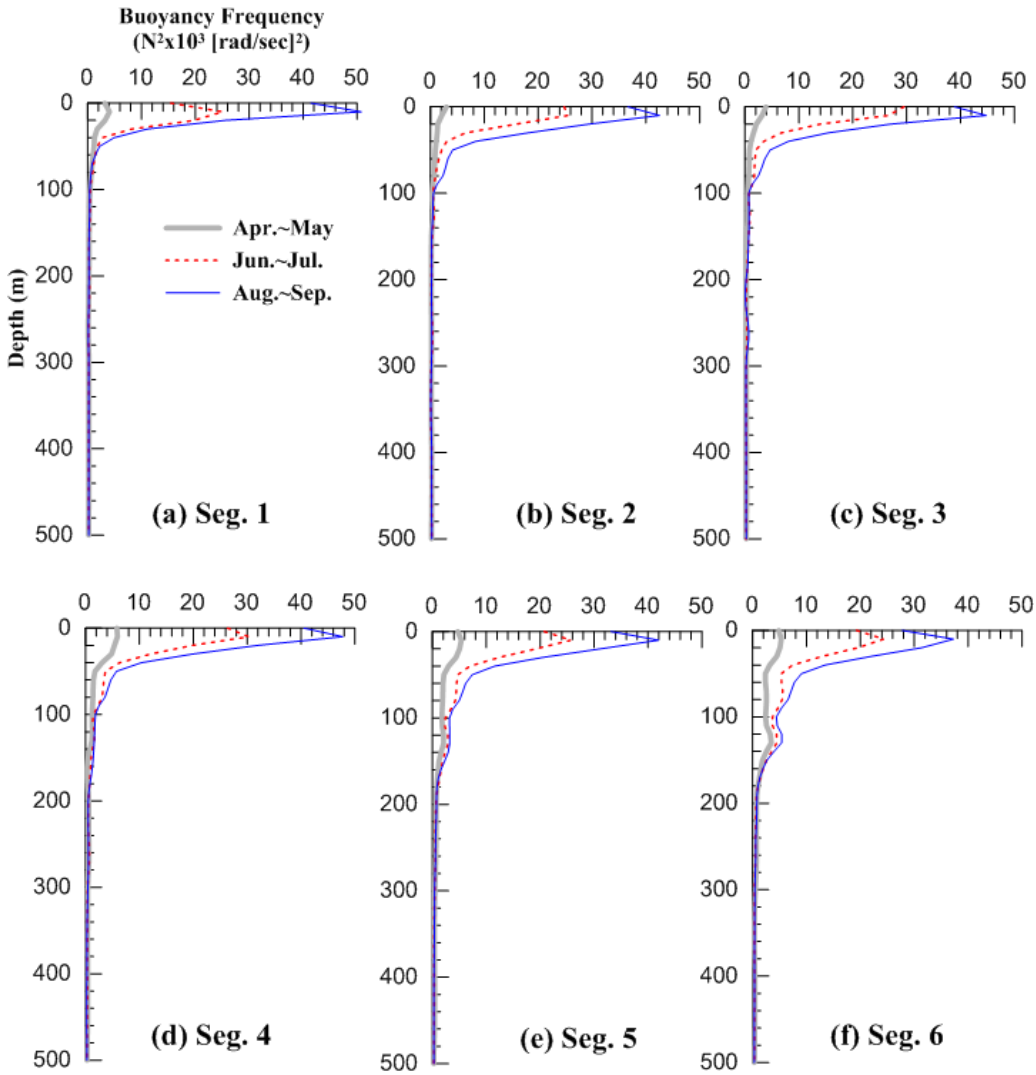

Figure IV-4. Buoyancy frequency profiles at the three separated periods (April to May, June to July and August to September) for the six segments from (a) to (f). These stratification conditions were used for input data in the CTW model run.

$$N^2 = N_O^2 \exp((\zeta_O - \zeta)/\alpha)$$

where N_O^2 is the deepest $N^2(z)$ value, ζ_O is the depth of the last $N^2(z)$ value, ζ is the depth of the point $\zeta = -z$ and α is the exponential tail on the N^2 profile then the α is the exponential length scale of $N^2(z)$ decay. Figure IV-4 shows the bimonthly-averaged stratification conditions for the 18 cases (topography 6 cases by stratification 3 cases) in terms of the buoyancy frequencies. In the northern three segments, the considerable values of buoyancy frequencies are limited with the 100 m depth from surface. But those in southern three segments are deepened near 200 m depth. At the depth range from 100 m to 150 m in segment 6, a remarkable feature is appeared regardless of periods, i.e. the buoyancy frequencies are increasing as deepening.

3. Results of the CTW model

A number of simulations were performed to determine the relative effects depending on the various choices of the input parameters. The eighteen environmental cases were prepared and applied for calculating the characteristics of the CTWs. The results of CTW model ($F_n(x,z)$, a_{nn}, b_n, and c_n,) in the study area, were computed by using the numerical method described by Brink and Chapman (developed in 1985 and updated 1992 with some tools to check the modal structures and modal number). It was not easy to separate the higher modes from given initial conditions because of not only the limited numerical resolution, but also the increased sensitivity of higher modes due to the inputs. It was reported that only a few CTW modes (generally within the first

three modes) were enough to explain the predictions by the CTW propagations in the previous study [Chapman et al, 1987 and Jordi et al, 2005].

The three leading CTW modes were calculated using a grid of 100 vertical by 120 horizontal cells. The along-shelf wind stress data (ECMWF-ERA40) from March 31 to September 27, 2001 at cells selected along the coast are used to integrate wind forcing combined with decay coefficient (a_{nn}) and wind coupling coefficients (b_n) of the first three CTW modes (Table IV-1).

The way of identifying CTW mode is counting the number of zero crossing in pressure structures. In case of the barotropic Kelvin wave, there is no zero crossing in pressure. The first CTW mode will have one zero crossing, etc. In this study, the source program is modified to find the mode number automatically, by adding the code to count the number of zero crossing in the structures of pressure. Using this modification, it is possible to identify the higher modes of CTW, for the various initial and boundary conditions.

Cross-sectional structures of pressure P (F_n) of first three CTW modes for the 18 cases (six shelf topographies for segment 1 to 6 and three stratifications for Periods 1, 2, and 3) are shown in Figure IV-5. The modal structures in the northern three segments were similar each other, irrespective of the stratification conditions from spring to summer. The opposite sign appears at the depth of 1,400 m in the first modal structures at all stratifications in the northern segment. It is more likely that the internal Kelvin waves than the shelf waves, as expected by the large burger number ($B_u = (NH/fL)^2$ is an order of 10^2 compared to those of the Mediterranean Sea (order of 1) and Baltic Sea (order of 1 or less). In the second modes of the northern three segments, the first changes of the sign are appeared at 500 m depth and the second changes near 2,000 m depth. There are no considerable differences in the modal structures depending on the

seasonal changes, but the propagation related parameters (phase speeds, frictional decay coefficients and wind coupling coefficients) are calculated with some differences due to the changes of the stratifications. These results reveal that the CTW modal structures in the northern parts off the east coast of Korea (at the higher latitude than 40 ^{o} North) are less affected by the stratification conditions (at least spring and summer season) rather than the bottom topography.

Phase speeds, wind coupling coefficients, and frictional decay coefficients of the first three CTW modes are more sensitive to shelf topography than stratification for the given environments (Table IV-1). Phase speeds of the first modes (c_1) are range of 8.3 to 11.9 m/s at all segments except Seg.5 (4.6-5.9 m/s) where the basin is shallow. These remarkably high speeds of CTWs are reported in the previous studies of New Jersey shelf area (~10m/s) [Yankovsky et al, 1998] and the south-eastern coast of Austria (~15m/s) [Freeland et al, 1986]. Higher mode's CTWs have propagated shorter distance, and easily damped with lower phase speed and larger frictional decay coefficient. Wind coupling coefficient generally increases southward (though not always) as the shelf widens regardless of the stratification conditions.

Applying the cross-shelf geostrophic and vertical hydrostatic balances, temperature fluctuations in Segment 5 (T_{CTW}) are predicted from the pressure field and variations. Temporal structure of T_{CTW} is determined by the amplitude ϕ_n . The energy conservation ratio (q_{nn}) at each boundary between the two successive segments was calculated using the CTW modal structure only for the case of mode n to n (Table IV-2). In the first CTW modes, the energy loss caused by scattering at the boundaries is less than 5% except the boundary between segment 4 and 5 (6%). It was shown that the energy transport ratios from segments to segments gradually decreased in the higher modes (see the equation 4-4 for q_{nn}).

Table IV-1. Along-shelf distance (y; km) from the mooring off the mid-east coast of Korea, phase speed (c_n; *m/s*), frictional decay coefficient (a_{nn}; x 10^{-9} cm^{-1}) and wind coupling coefficient (b_n;$s^{1/2}$ $cm^{-1/2}$) of the first three CTW modes for six segments (Seg. 1 to 6; different shelf topographies) and three periods (Period 1 to 3; different stratifications).

Segment No.	y (*km*)	Mode	April ~ May			June ~ July			August ~ September		
			c_n	a_{nn}	b_n	c_n	a_{nn}	b_n	c_n	a_{nn}	b_n
1	1,010	1	10.6	0.97	0.34	11.4	0.29	0.36	11.3	0.29	0.35
		2	5.4	0.69	0.38	5.3	1.04	0.45	5.2	1.13	0.40
		3	3.1	1.41	0.45	3.1	3.06	0.61	3.2	4.05	0.47
2	770	1	9.5	0.36	0.37	11.0	0.30	0.36	11.9	0.29	0.37
		2	4.3	0.97	0.40	4.5	0.93	0.41	5.5	0.90	0.42
		3	3.0	1.61	0.35	3.0	1.64	0.39	3.7	1.03	0.29
3	430	1	10.6	0.37	0.39	8.8	0.43	0.41	9.8	0.53	0.43
		2	5.1	0.96	0.37	3.6	0.76	0.34	5.0	2.11	0.52
		3	3.2	2.02	0.40	2.5	1.62	0.26	3.6	1.98	0.31
4	220	1	8.7	0.67	0.49	8.3	0.94	0.54	8.7	0.66	0.53
		2	4.4	2.10	0.58	4.4	1.72	0.40	5.2	0.21	0.27
		3	2.8	3.34	0.55	2.9	1.84	0.18	3.4	1.09	0.16
5	90	1	5.8	0.98	0.54	4.6	0.45	0.18	5.9	1.01	0.54
		2	3.4	1.74	0.44	2.4	1.11	0.14	2.9	2.31	0.53
		3	2.0	3.35	0.41	2.4	1.10	0.10	1.6	4.21	0.40
6	-	1	10.3	0.77	0.55	10.0	0.80	0.57	9.5	1.20	0.65
		2	5.1	2.47	0.64	4.7	3.02	0.81	5.3	2.81	0.68
		3	3.3	3.07	0.52	3.3	3.34	0.71	3.5	2.00	0.32

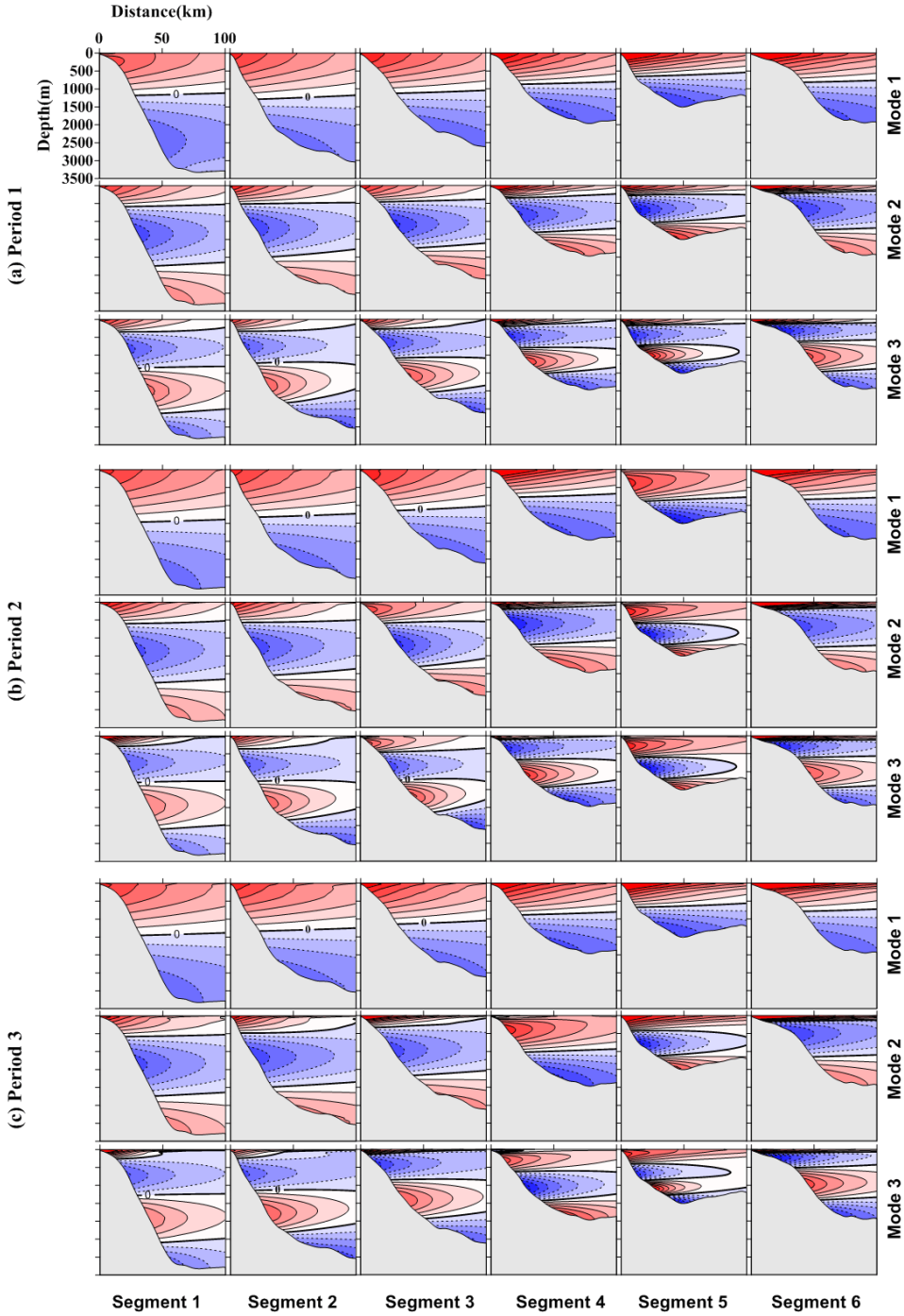

Figure IV-5. Modal structures of the first three modes of CTWs (F_1, F_2, and F_3) for three different periods (Period 1 to Period 3) and six segments (Seg.1 to Seg.6).

Table IV-2. Modal scattering ratio (s_{nn}) at the segment's boundaries calculated for the first three mode CTWs for three different periods (different topography and stratification conditions). The portion of energy ($q_{nn} = 1\text{-}s^2_{nn}$) entering the each section boundary is scattered into the other modes.

Segment Boundary.	April ~ May			June ~ July			August ~ September		
	mode1	2	3	mode1	2	3	mode1	2	3
1-2	0.99	0.96	0.91	0.99	0.95	0.89	0.99	0.88	0.42
2-3	0.98	0.96	0.86	0.98	0.94	0.83	0.95	0.33	0.44
3-4	0.99	0.79	0.62	0.99	0.78	0.59	0.98	0.83	0.50
4-5	0.94	0.89	0.86	0.99	0.52	0.23	0.93	0.86	0.66
5-6	0.96	0.85	0.70	0.97	0.42	0.30	0.96	0.67	0.41

4. Prediction of the temperature fluctuations in 2001

In order to predict the temperature fluctuations due to the CTWs propagations, the along-shelf wind stress are inputted as a forcing to generate the CTWs. The wind forcing along the coastal positions (red dots in Figure II-2) is applied to the equation (3-3) with the wind coupled coefficient (b_n).

The fluctuations of the water temperature (T_{CTW}) at the surface mooring station are predicted using the CTW propagation parameters (a_{nn}, b_n, and c_n,) and energy conservational ratio (q_{nn}) with the along-shelf wind forcing. The integrated fluctuations of CTWs make influence on the water temperatures through upwelling or downwelling processes at the coastal area. The equation (4-2) has a solution to calculate the variations of the amplitudes due to the generations and propagations of the CTWs, like equation (4-4).

$$\phi_{ni}(0,t) = q_{nni}\phi_{ni}\left(y, t - \int_0^y c_{ni}^{-1} d\xi\right)\exp\left(-\int_0^y a_{nni} d\xi\right) + \int_0^y b_{ni}(\xi)\tau\left(\xi, t - \int_\xi^y c_{ni}^{-1} d\xi'\right)\exp\left(-\int_\xi^y a_{nni} d\xi'\right)d\xi \quad \text{------ (4-4)}$$

$$q_{nn} = \int_{-h(\infty)}^{0} F^{+}{}_{n}(d_{+}(z), z)F^{-}{}_{n}(d_{-}(z), z)dz$$

where, n is modal number and i is the stratification condition indicator (the period number). And q_{nn} is the modal scattering ratio of the amplitude of scattered mode n to that of incident mode m, the scatterings of mode n to n only are applied here and F is evaluated before (+) and after (-) the irregularity in shelf topography at each section boundary [*Johnson*, 1991 and *Jordi*, 2004]. The first term of right hand side of equation (4-4) is the amplitude variation due to the propagations (with phase speed of c_n) of coastal trapped waves freely along the coast modified by friction (a_{nn}). And the second term is the response of the wave amplitude function to the past forcing along

the wave's path [Battisti and Hickey, 1984]. The resulting amplitude $\phi_n(0,t)$ from equation (4-4) combined with $F_n(x,z)$ from equation (4-2) predict $P(x,y,z,t)$. Density perturbation can be estimated from $\rho = -\frac{1}{g}\frac{\partial p}{\partial z}$ and temperature from the state equation ($\rho = \rho(T,S,p)$) by assuming that the contribution of salinity (*S*) to density change is negligible compared to that of temperature (*T*).

The amplitudes of the CTWs are calculated for the forty-five cases (three stratifications, five accumulated starting points, three accumulated modes) using the following equation

$$\phi_{mki}(0,t) = \sum_{m=1}^{k}\sum_{n=1}^{m} \phi_{ni}(0,t) \quad \text{---------- (4-5)}$$

where *m* is the mode number to be summed and *k* indicates the starting segment number. The starting segment number (*k*) represents the simulation number which is separated with the different initial boundary conditions (or locations, diamond in Figure IV-6d). Because that the position of the ESROB is setting as the end of CTWs propagations southward, the model results in the segment 6 are not used to compromise the T_{CTW}.

Figure IV-6 shows the results of the predictions induced by the CTWs propagations along the coast for forty-five cases. At the boundaries between the periods, the predictions are continued to the next period successively. The temperature fluctuations simulated by only the first CTW baroclinic mode is shown in Figure IV-6a of which variations are simpler than the others (in cases of including the higher modes in Figure IV-6b and c). In the case of the integrations from the northern segments, the major wind events along the coast make the time delayed phenomena on the features of

predictions. These features dominantly appeared in spring season (March to mid-June) and mid-August in Figure IV-6.

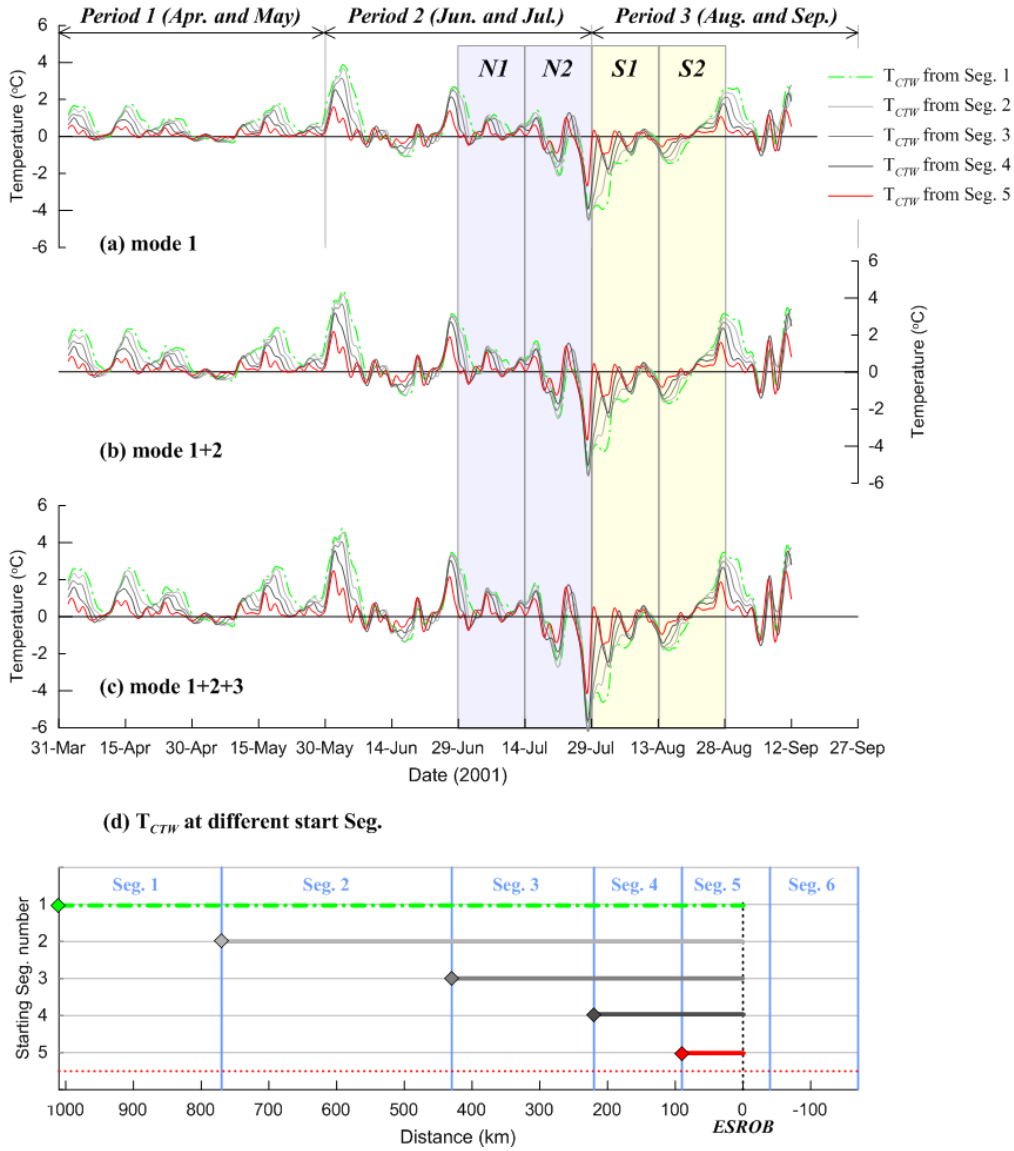

Figure IV-6. The predictions of the variability of the water temperature at the buoy station. The total period (from April to September) is divided into three periods (period 1, 2 and 3) with two month for each period. The five cases of predictions distinguished from the accumulated start segment boundary are depicted for the three cases of the accumulated modal numbers. (d) explains the concepts of the accumulation with different start segment to predict the T_{CTW}. Diamonds are the initial boundary of CTW model, and the red dot line is rearranged straightly of the curved line along the east coast of Korea. The vertical black dot line is the location of surface mooring (ESROB) which is the end of accumulation.

5. Comparison with observed temperature fluctuations

a. Comparison between T_{OBS} and T_{CTW} at offshore site

Using the CTW model and the first order wave equation (4-3), the water temperature fluctuations are predicted and compared with the observed ones at offshore site (Figure IV-7b). The wind forcing is integrated to the surface mooring position in terms of the amplitude (ϕ) of the CTWs. And it is converted to temperatures (T_{CTW}; temperature induced by CTWs), using hydrostatic approximation and negligible salinity variations.

Seasonal trend is removed from the observed temperature variations, applying the 3rd order orthogonal polynomial curve fitting, and the temperatures are depth-averaged with a weight proportional to vertical separations of CTD sensors. The low-passed, depth-averaged, demeaned, and de-trended water temperature fluctuations (T_{OBS}) are compared with T_{CTW} (Figure IV-7b). Correlations between the observed and modeled temperature (T_{OBS} vs T_{CTW}) is significant in 95% confidence and the maximum correlation coefficient for total period is 0.35 (integrated from Segment 3) which increases up to 0.58 when excluding August events (S1 and S2; Table IV-3). This is in contrast to the low (< 0.2) correlations between T_{OBS} and other fluctuations, e.g. sea level and wind stress. Even though including 2nd and 3rd mode, the prediction by CTWs does not meaningfully improve the correlation (results are not sensitive to the number of modes summed, but the periods, Table IV-3).

T_{CTW} are best correlated with T_{OBS}, when the equation is integrated from Segment 3 in Period 1, Segment1 in Period 2, and Segment 4 in Period 3 (only September and excluding two August events). High correlations (correlation coefficients of 0.65 which is significant in 95% confidence) during Period 2 including two July events (N1 and

N2) is found when integrated from Segment 1 (Table IV-3). In contrast, low or negative correlations appear during Period 3, and events S1 and S2 in August mainly contribute to the negative correlations between T_{OBS} and T_{CTW}. Excluding those August events (the period of the southward currents become strong), the correlations show high values of 0.6 when integrated from segment 4 (Figure IV-7b and Table IV-3). The maximum correlations between T_{CTW} and T_{OBS} are found in the case of start from not Seg. 5 but more northern segments, which implies that the remotely wind forcing takes obviously a role to change of the local temperature.

Table IV-3 Correlations between the modeled (T_{CTW}) and observed (T_{OBS}) water temperature for the cases with different starting points of integration (from Seg.1 to Seg.5) and different numbers of modes (mode 1 only, modes 1+2, modes 1+2+3) for three periods (Period 1 to 3) and periods including and excluding August events.

Modes	Start Seg. No.	Period 1 Apr. to May	Period 2 Jun. to Jul.	Period 3 Aug. to Sep.	Period 3		Total period	
					Aug.	Sep.	Include Aug.	Exclude Aug.
1	1	0.36	**0.65**	-0.07	-0.27	0.24	0.34	0.54
	2	0.39	0.64	-0.10	-0.36	0.37	0.34	0.56
	3	**0.41**	0.62	-0.06	-0.39	0.54	**0.35**	**0.58**
	4	0.40	0.56	0.05	-0.42	**0.60**	0.34	0.55
	5	0.33	0.44	0.04	-0.46	0.43	0.26	0.44
1+2	1	0.35	0.65	-0.06	-0.33	0.35	0.33	0.53
	2	0.39	0.63	-0.08	-0.37	0.45	0.33	0.55
	3	0.40	0.60	-0.04	-0.41	0.58	0.34	0.57
	4	0.40	0.54	0.05	-0.44	0.59	0.33	0.54
	5	0.33	0.44	0.04	-0.46	0.44	0.26	0.44
1+2+3	1	0.35	0.64	-0.05	-0.35	0.38	0.33	0.52
	2	0.39	0.63	-0.07	-0.38	0.47	0.33	0.55
	3	0.40	0.60	-0.04	-0.42	0.57	0.34	0.56
	4	0.40	0.55	0.04	-0.45	0.60	0.33	0.54
	5	0.33	0.44	0.05	-0.47	0.45	0.26	0.44

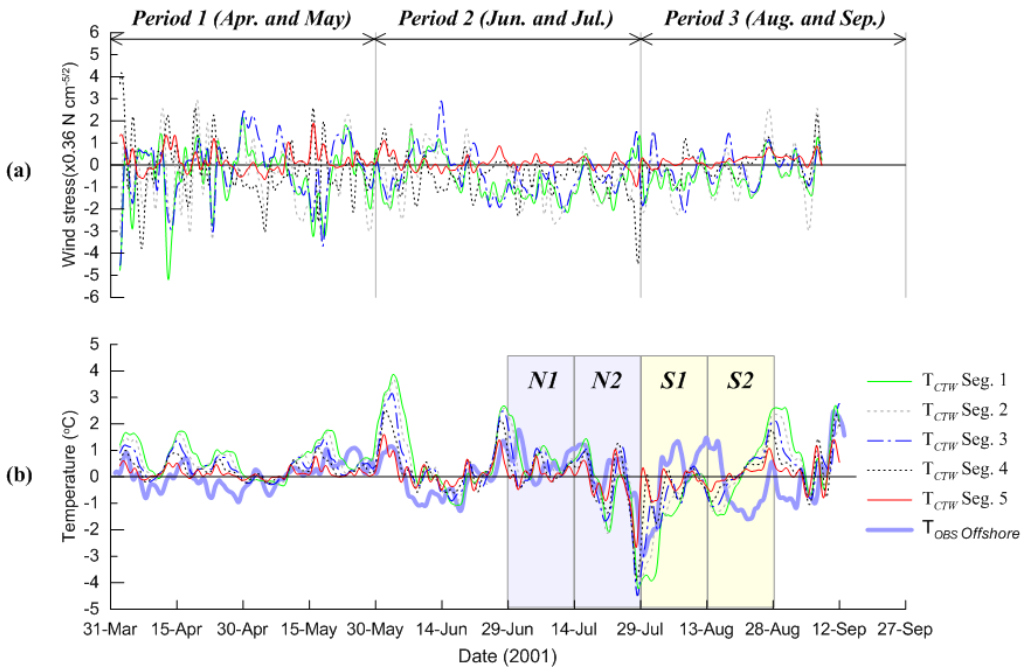

Figure IV-7. (a) Cumulative along-shelf wind stress applied to the CTW model for six segments. (b) Depth-averaged subtidal temperature fluctuations observed (thick gray) at offshore site and predicted by the first CTW mode for different starting points of integration along the coast.

b. Comparison between T_{OBS} and T_{CTW} at inshore site

The water temperature fluctuations at inshore bottom are also compared with the predicted by CTW model (Figure IV-8). Correlations between the observed and modeled temperature (T_{OBS} vs T_{CTW}) at inshore site show the similar values with the cases at offshore site for the period 2 (r=0.59 in inshore site vs. r=0.65 in offshore site). During the period 3, the correlation between T_{OBS} and T_{CTW} becomes lower compared to that in period 2 at inshore site, though it is higher than that at offshore site (Table VI-3 and Table VI-4). The maximum correlations are appeared in the case of the accumulated form segment 1 (when the remote wind forcing is applied).

Besides the events S1 and S2 (low correlations between the predicted and observed temperature fluctuations at offshore site), there are some mismatches between the predicted and observed ones at inshore site, which are caused by the temperature drop at inshore bottom (black arrows in Figure IV-8). The first two cooling events at inshore bottom are not observed at offshore site. Being unlike the previous two events, the temperatures drop at both sites around 29-Jul. (the forth arrows in Figure IV-8). During the third cooling event, the temperature at offshore site is weakly changed comparing with that at inshore site. The patterns of the change of temperature at inshore and offshore sites can be divided into two types, e.g. first two cooling events and the forth (including weakly the third case) one. Moreover, the last two cooling events are relatively well predicted by CTW model. The discrepancies of the temperature fluctuations between inshore and offshore sites and between the observations and predictions by CTW model at inshore site are investigated in this study, considering the along-shelf currents and enhanced vertical shear which is described in Chapter III.3.

Table IV-4 Correlation coefficients between the modeled (T_{CTW}) and observed (T_{OBS}) water temperature fluctuations at inshore site, applying the different starting points of integrations of the CTW model predictions.

Modes	Start Seg. No.	Period 2	Period 3	Total period
		Jun. ~ Jul.	Aug. ~ Sep.	
1	1	**0.59**	**0.25**	**0.36**
	2	0.53	0.21	0.35
	3	0.47	0.21	0.33
	4	0.35	0.22	0.28
	5	0.21	0.20	0.20

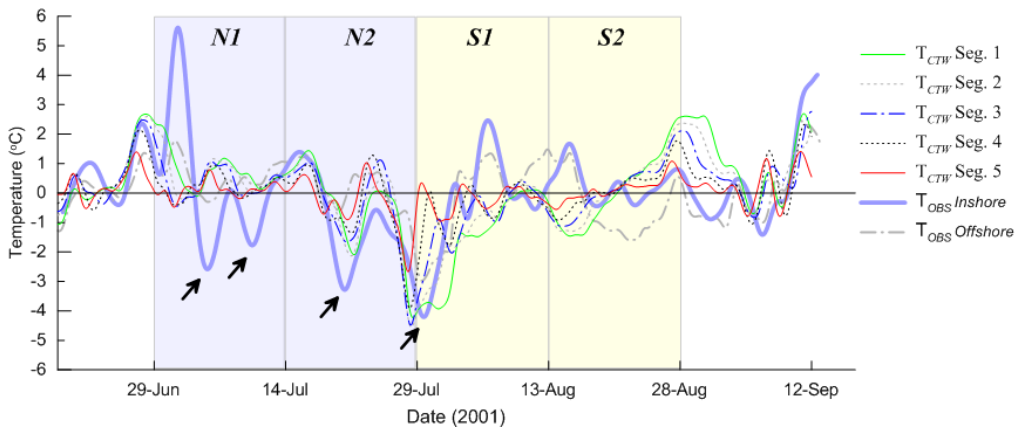

Figure IV-8. Subtidal temperature fluctuations observed at inshore bottom (light thick blue line), depth-averaged one observed at offshore site (grey semi-dot line), and predicted by the first CTW mode for different starting points of integration along the coast.

6. Application of the CTWs theory (model) to the years from 2006 to 2011 at offshore site

a. Application of CTW model including winter season

In order to check that the subtidal temperature variability can be generally explained in terms of the CTW theory in this study area, it is applied for the additional periods (the year from 2006 to 2011) adding to the year of 2001. The procedure of application of CTWs theory is the same as described in Figure IV-2. The CTW model and bathymetries are reused. But the stratifications (N^2; buoyancy frequency) are newly calculated using the WOA2001 data for each segment and six periods which are bimonthly and include winter season (Figure IV-9). These stratification conditions are differ from those in the year of 2001 defined in period 1 (April to May), 2 (June to July), and 3 (August to September). There are minor differences of the frequencies between the segments, but those of winter season (from November to April) are less than $5x10^3$ rad^2/sec^2 and there are weak peaks within 200 m depth. At this additional application of CTW model, the total number of predictions of temperature variability driven by CTW model is 3,240 (stratification condition: 6 cases, segments: 6 cases, modal structure: 3 cases, accumulated number of starting: 5 cases, yearly periods: 6 cases).

To perfume the predictions, the phase speeds (c_n), frictional decay coefficients (a_{nn}), and wind coupling coefficients (b_n) of the first three CTW modes are extracted from the runs of CTW model (Table IV-5). The energy conservational ratios (q_{nn}) at each boundary between the segments also are calculated from the modal structures (not shown but used for predictions of T_{CTW}).

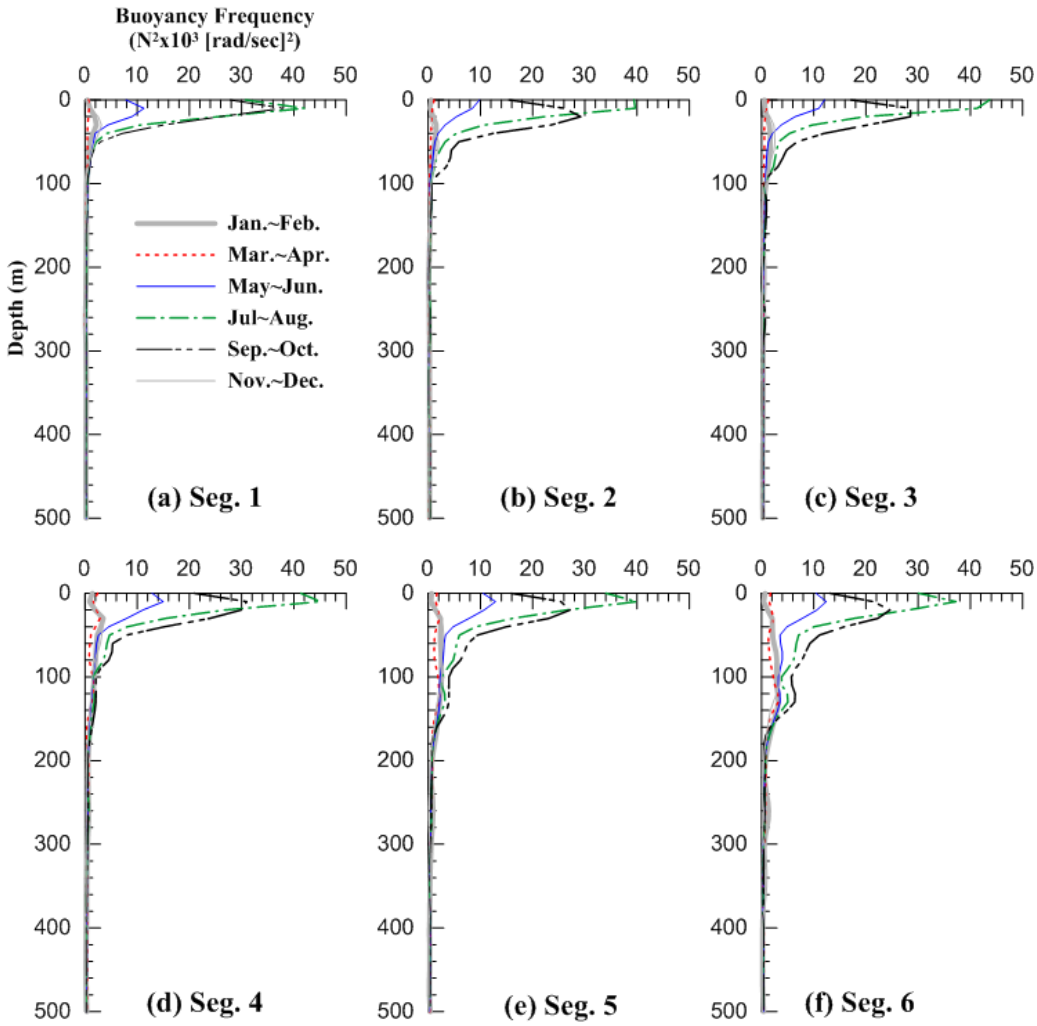

Figure IV-9. Buoyancy frequency profiles at the six distinguished periods (bimonthly) for the six segments from (a) to (f). These stratification conditions were used for input data in the CTW model run.

Table IV-5. Phase speed (c_n; *m/s*), frictional decay coefficient (a_{nn}; x 10^{-9} cm^{-1}) and wind coupling coefficient (b_n;$s^{1/2}$ $cm^{-1/2}$) of the first three CTW modes for six segments and bimonthly (six) stratification conditions

Seg. No.	mode	January-February			March-April			May-June		
		c_n	a_{nn}	b_n	c_n	a_{nn}	b_n	c_n	a_{nn}	b_n
1	1	**11.6**	.28	.37	**11.3**	.30	.37	**11.4**	.29	.37
	2	**5.4**	.86	.42	**5.4**	1.22	.43	**5.4**	1.07	.48
	3	**3.2**	2.24	.53	**3.3**	3.52	.46	**3.1**	3.25	.69
2	1	**10.4**	.32	.36	**10.9**	.33	.38	**11.2**	.34	.39
	2	**4.1**	.94	.39	**5.7**	.17	.07	**3.9**	.40	.08
	3	**2.9**	1.78	.40	**3.7**	.43	.07	**3.9**	.42	.08
3	1	**10.3**	.41	.41	**9.4**	.49	.42	**9.3**	.47	.42
	2	**5.0**	1.16	.38	**4.6**	1.39	.45	**4.1**	.97	.43
	3	**3.3**	1.90	.28	**3.1**	2.76	.50	**2.7**	1.65	.41
4	1	**8.9**	.69	.50	**8.6**	.83	.53	**9.4**	1.14	.49
	2	**4.5**	1.86	.55	**4.2**	1.92	.54	**5.1**	.30	.17
	3	**2.9**	2.72	.48	**2.8**	2.38	.40	**3.1**	1.08	.13
5	1	**5.8**	1.00	.54	**5.8**	.98	.54	**7.6**	.90	.57
	2	**3.3**	1.82	.46	**3.2**	2.07	.51	**4.1**	.76	.22
	3	**1.9**	3.63	.45	**1.8**	4.45	.52	**2.2**	1.43	.15
6	1	**10.4**	.79	.56	**10.4**	.73	.56	**10.4**	.89	.59
	2	**5.4**	2.45	.61	**4.2**	2.46	.79	**5.3**	2.95	.72
	3	**3.5**	2.38	.36	**2.8**	3.69	.97	**3.6**	2.11	.38

		July-August			September-October			November-December		
		c_n	a_{nn}	b_n	c_n	a_{nn}	b_n	c_n	a_{nn}	b_n
1	1	**11.3**	.28	.36	**11.3**	.29	.35	**8.0**	.26	.45
	2	**5.2**	.52	.53	**5.3**	1.03	.46	**7.9**	.35	.50
	3	**.4**	5.99	.02	**3.1**	3.39	.71	**2.8**	4.18	.32
2	1	**11.6**	.32	.39	**12.1**	.29	.38	**8.3**	.41	.37
	2	**5.4**	.96	.44	**5.7**	.83	.42	**3.7**	1.29	.42
	3	**3.6**	1.05	.29	**3.8**	.81	.24	**2.5**	2.52	.46
3	1	**9.8**	.52	.44	**10.1**	.53	.44	**7.0**	.35	.35
	2	**4.9**	1.78	.52	**5.2**	1.85	.48	**3.0**	.91	.22
	3	**3.4**	2.27	.41	**3.7**	1.38	.21	**1.5**	.78	.17
4	1	**8.5**	.72	.54	**8.7**	.66	.53	**6.5**	1.55	.55
	2	**3.4**	1.23	.78	**3.6**	1.24	.76	**3.8**	2.08	.27
	3	**.4**	8.85	.01	**.5**	28.15	.00	**2.4**	2.15	.06
5	1	**6.5**	.99	.57	**6.7**	.97	.57	**3.7**	.97	.34
	2	**3.4**	1.86	.49	**3.5**	1.75	.48	**2.0**	2.11	.26
	3	**1.9**	4.10	.52	**1.9**	3.87	.50	**1.2**	5.73	.17
6	1	**10.2**	1.39	.64	**9.9**	.54	.55	**7.5**	.82	.59
	2	**6.0**	.81	.09	**3.9**	.75	.45	**3.1**	1.40	.53
	3	**3.8**	1.02	.08	**2.9**	.75	.44	**1.7**	1.50	.16

Most of q_{nn} are greater than 0.95 for the first CTW modes and these values are similar to the results of previous CTW model runs.

The phase speeds of the first CTW modes are in winter (from Nov. to Feb.) are 3.7 ~ 11.6 m/s, those of November-December are small (3.7 ~ 8.3 m/s) compared to the other periods. Phase speeds in segment 5 are smallest among the 6 segments at all periods.

b. Predictions of water temperature fluctuations by CTW model

Using the CTW model results (a_{nn}, b_n and c_n), the T_{CTW} can be predicted with remotely and locally wind forcing (equation 4-5). The wind stress data are obtained for six years (2006 ~ 2011), using the same process that was applied in the previous works. The period of wind stress calculation is determined, based on the periods of T_{OBS}. After the main trial periods (Apr. to Sep. in 2001), the observations of temperature (including the oceanographic and metrological data) have been continued near the surface mooring site off the mid-east coast of Korea (as described in Chapter II.1.a). The temperature time series data with a few blanks are selected as the comparison data sets of six years with T_{CTW} (period of the yellow box in Figure IV-10).

As the results of applications from 2006 to 2011, the T_{CTW} was produced using the first three CTW modes for that period. But, the higher CTW modes lead to little change the prediction (according to the results of the comparison between T_{OBS} and T_{CTW} in 2001). Therefore, the T_{CTW} considered the only first CTW mode were analyzed with different start locations (Figure IV-6d and Figure IV-11).

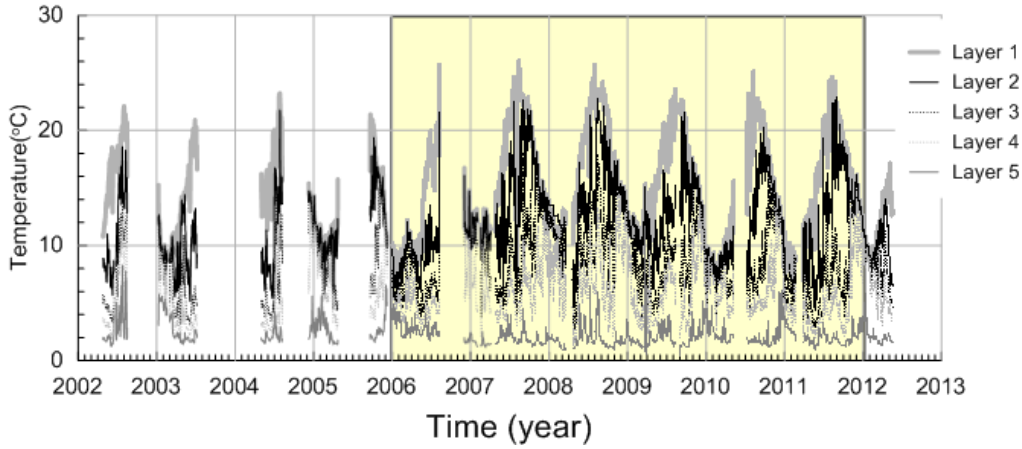

Figure IV-10. Low-passed filtered temperature variations from 2002 to 2012 observed from surface mooring system at the mid-east of Korea. The discontinuity of the time series is caused by observation error at that period. Period of relatively good observation condition is highlighted with a yellow box.

c. Comparison between TOBS and TCTW from 2006 to 2011

During the periods from 2006 to 2011, T_{CTW} predicted by the first CTW mode's propagations was compared with the T_{OBS} (only for the overlapped periods of the two data sets) in Figure IV-11. The correlations between T_{OBS} and the five T_{CTW} accumulated with different start sites, showed significant similarities for the overall periods. These features of similarities between the T_{OBS} and T_{CTW} were shown in winter as well as summer. In 2007 and 2008, mismatches of the two water temperatures were rather clear in summer (Jul. to Sep.). These mismatches might be related to the strong local currents and enhanced vertical shear (not shown).

The correlation coefficients between the T_{OBS} and T_{CTW}s are summarized at Table IV-6. The monthly correlations are calculated classify the features of monthly basis. The correlations between T_{CTW} and T_{OBS} have wide range from -0.78 (May 2010, Seg.1) to 0.88 (November 2007, Seg.2). The difference of correlations within a year and even within a month was larger compared to that in 2001. During the period from January to May in 2006, it showed high correlations between T_{OBS} and T_{CTW} (0.45 to 0.78). After May, the mismatches were increased and the correlations had been down to negative sign (-0.11, on the basis of the highest correlation for each month of the year). During the period from 2007 to 2011, there were large differences in the monthly correlations. The averaged values of monthly correlations showed that the water temperatures variations predicted by CTW model were better matched with those in winter (Nov. to Apr.) than in spring and summer (May to Oct.). When it came to the averaged value with the maximum correlations within each month, the monthly correlations were over 0.3 except June and September. This relation between T_{OBS} and

T_{CTW} is similar to the case in 2001 including the period (August in 2001) of the poor correlation.

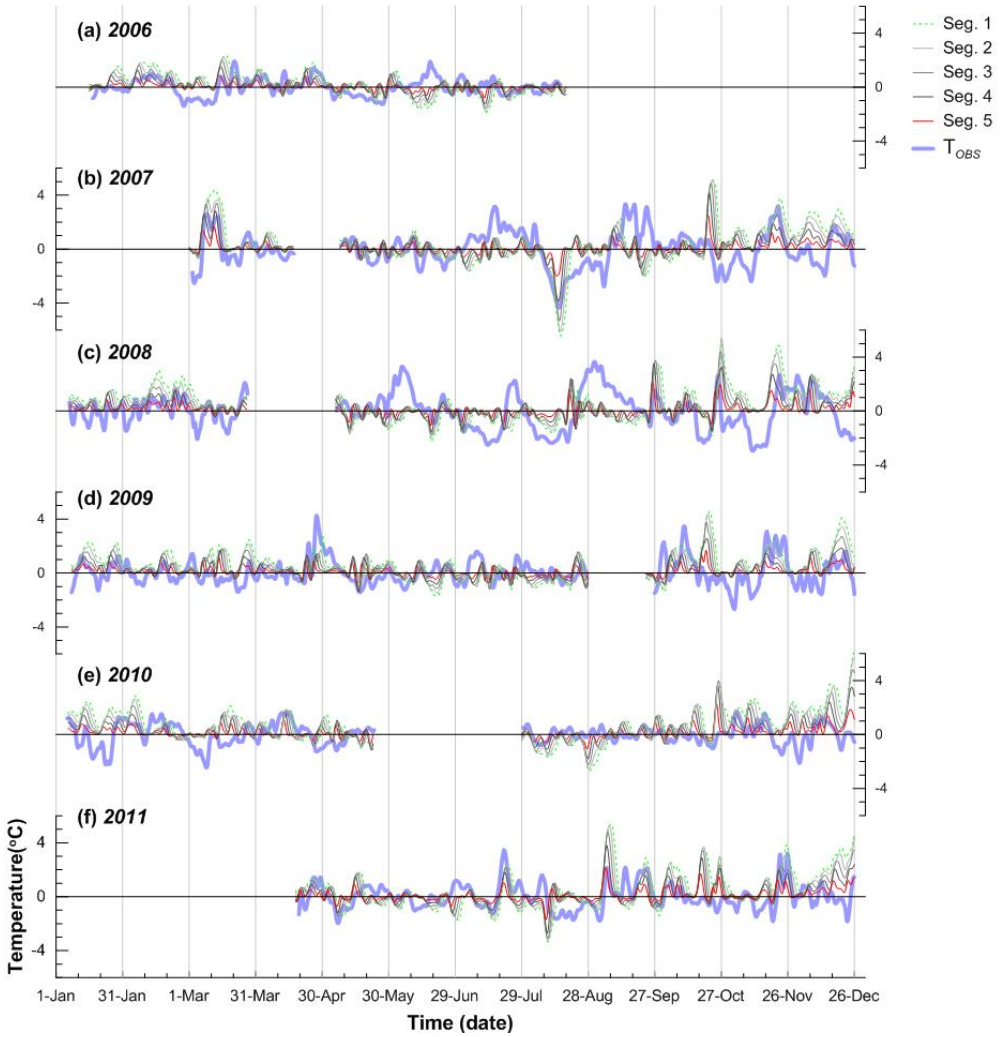

Figure IV-11. Depth-averaged subtidal temperature fluctuations observed (thick line) and predicted by the first CTW mode for different starting points of integration along the coast (thin lines) for six years (2006 (a) ~ 2011(f)).

Table IV-6. Correlations between the modeled (T_{CTW}) and observed (T_{OBS}) water temperature for the cases with different starting points of integration (from Seg.1 to Seg.5) and monthly separated from 2006 to 2011 and six years mean (2006~2011).

year	Start Seg. No.	Period (month)											
		Jan.	Feb.	Mar.	Apr.	May.	Jun.	Jul.	Aug.	Sep.	Oct.	Nov.	Dec.
2006	1	.29	**.78**	.47	**.57**	**.56**	-.54	-.14	-.58				
	2	.41	.74	.51	.42	.44	-.47	.02	-.41				
	3	.42	.69	**.56**	.24	.37	-.38	.08	-.27				
	4	.40	.61	.56	.25	.41	-.24	.09	-.06				
	5	**.45**	.53	.47	.37	.44	**-.11**	**.18**	**.25**				
2007	1			.77		**.70**	.21	**.56**	**.74**	-.12	-.46	.86	.31
	2			.82		.45	.37	.52	.73	-.15	-.23	**.88**	.38
	3			**.83**		.37	.46	.52	.71	-.11	.00	.87	.43
	4			.73		.51	**.50**	.52	.66	-.02	.17	.79	**.45**
	5			.52		.60	.46	.50	.59	**.04**	**.25**	.68	.42
2008	1	.02	.46	.11		**.16**	.20	-.28	**.57**	**.40**	.68	**.75**	**.09**
	2	**.21**	.49	.29		.11	.26	-.20	.52	.30	.69	.62	.09
	3	.16	**.58**	.49		.08	**.33**	-.06	.44	.20	**.71**	.50	.03
	4	.12	.53	**.56**		-.06	.30	**.01**	.36	.10	.70	.35	-.07
	5	-.03	.23	.45		-.22	.22	.01	.25	-.03	.58	.24	-.24
2009	1	.30	.13	**.44**	.54	.32	-.03	-.06	**.15**		-.14	**.81**	.61
	2	.35	.25	.35	.56	**.38**	.11	-.02	.10		-.13	.75	**.63**
	3	**.41**	**.30**	.28	**.68**	.31	**.18**	**.06**	.01		**-.11**	.70	.63
	4	.39	.25	.12	.46	.18	.15	.04	-.13		-.12	.59	.59
	5	.21	.07	-.16	.07	.05	.07	-.06	-.28		-.12	.40	.46
2010	1	.25	.35	**.23**	**.45**	-.78			**.52**	-.19	**.42**	**.62**	.14
	2	**.26**	.35	.15	.32	-.73			.50	-.21	.35	.53	.22
	3	.26	.34	-.01	.13	-.67			.50	-.14	.32	.40	.30
	4	.21	.38	-.14	.04	-.52			.45	-.01	.25	.24	**.31**
	5	.12	**.42**	-.11	.05	**-.36**			.39	**-.00**	.08	.01	.24
2011	1					**.46**	-.39	.56	**-.33**	.44	.33	.64	-.10
	2					.42	-.38	.66	-.36	.48	.33	.69	-.06
	3					.41	-.40	.77	-.37	**.51**	**.34**	**.76**	**.01**
	4					.37	-.34	**.84**	-.38	.49	.25	.71	-.02
	5					.24	**-.22**	.81	-.46	.37	.03	.50	-.12
Mean (2006 ~ 2011)	1	.22	.43	.40	**.52**	**.24**	-.11	.13	**.18**	.13	.17	**.74**	.21
	2	**.31**	.46	.42	.43	.18	-.02	.20	.18	.11	.20	.69	.25
	3	.31	**.48**	**.43**	.35	.15	.04	.27	.17	.12	**.25**	.65	**.28**
	4	.28	.44	.37	.25	.15	.07	**.30**	.15	**.14**	.25	.54	.25
	5	.19	.31	.23	.16	.13	**.08**	.29	.12	.10	.16	.37	.15

Chapter Ⅴ. Subtidal water temperature fluctuations with non CTWs

1. Local forcing effects at the offshore site

a. Local nonlinear heat advection

The correlation between T_{CTW} and T_{OBS} drops during the periods of S1 and S2 (July 29 to August 28 in Figure IV-7b). It was reported that the horizontal temperature advection associated with regional-scale circulation variability at this local setting by two known currents; the East Korean Warm Current (EKWC) and the North Korean Cold Current (NKCC) [Cho and Kim, 1994]. When the study area is influenced by the strong along-shelf currents, Rossby number ($Ro = U/fL$) increases up to O(1), the nonlinear advection may be important.

In the assumption of the incompressibility and Boussinesq approximation (the adiabatic condition), the changes of temperature in time can be represented as

$$\frac{dT}{dt} = \frac{\partial T}{\partial t} + u\frac{\partial T}{\partial x} + v\frac{\partial T}{\partial y} + w\frac{\partial T}{\partial z} = 0$$

And if the horizontal heat advections are greater than the vertical one due to the strong along-shelf currents, the nonlinear advection effect can be expressed below

$$\frac{\partial T}{\partial t} = -\left(u\frac{\partial T}{\partial x} + v\frac{\partial T}{\partial y} \right) \quad \text{---------- (5-1)}$$

The thermal wind relationship in the ocean yields

$$\begin{aligned} f\frac{\partial v_g}{\partial z} &= g\cdot\alpha\frac{\partial T}{\partial x} - g\cdot\beta\frac{\partial S}{\partial x} \\ f\frac{\partial u_g}{\partial z} &= -g\cdot\alpha\frac{\partial T}{\partial y} + g\cdot\beta\frac{\partial S}{\partial y} \end{aligned} \quad \text{---------- (5-2)}$$

Where, the geostrophic velocity are v_g ($=v-v_{ag}$) and u_g ($=u-u_{ag}$), defined as the difference between velocity (u and v) and the ageoptrophic velocity (v_{ag} and u_{ag}).

Assumption with the contribution of salinity (S) to density change can be negligible ($\alpha >> \beta$) compared to those of temperature (T), it can be approximated as below considering the thermal-wind relationship (equation (5-2)),

$$\frac{\partial T}{\partial x} = -\frac{f}{\alpha g}\frac{\partial v_g}{\partial z} \quad , \quad \frac{\partial T}{\partial y} = \frac{f}{\alpha g}\frac{\partial u_g}{\partial z}$$

which is supported by the cross-shelf geostrophy in observations (Figure III-3).

Then equation (5-1) can be represented as below

$$\frac{\partial T}{\partial t} \approx \alpha' \left(u_g \frac{\partial v_g}{\partial z} - v_g \frac{\partial u_g}{\partial z} \right) + \alpha' \left(u_{ag} \frac{\partial v_g}{\partial z} - v_{ag} \frac{\partial u_g}{\partial z} \right) \text{-------- (5-3)}$$

Here $\alpha'=f/(\alpha g)$, α is the thermal expansion coefficient $\alpha = -\rho^{-1}(\partial\rho / \partial T)_{p,S}$, and g is the gravity constant.

Even though the heat advections due to the geostrophic (first term of right side of (5-3)) become zero, the ageostrophic velocity can cause the change of temperature with time.

Local change of the depth-integrated temperature ($\frac{\partial}{\partial t}\int T dz$) can arise due to the horizontal advection (vertical advection does not appear in the vertically-averaged form of balance) as follows with negligible diffusion and when the surface heat flux is small (the variation of temperature at 20 m depth is much greater than 5 m depth)

$$\frac{\partial}{\partial t}\int T dz \approx \alpha' \int \left(u\frac{\partial v_g}{\partial z} - v\frac{\partial u_g}{\partial z} \right) dz \text{ ---------- (5-4)}$$

Time series of depth-averaged, cross-shelf ($u \times (\partial v_g / \partial z)$) and along-shelf ($v \times (\partial u_g / \partial z)$) advections and their subtraction show the increased nonlinear advection during the four events (Figure Ⅴ-1a), which are beyond the linear CTW dynamics. Events N1 and N2 are characterized by the strong (> 30 cm/s) northward currents near surface with the large vertical shears, and the weak (but not negligible) cross-shelf currents (Figure III-2b and 2c).

During both July (N1 and N2) and August (S1 and S2) events, the temperature changes due to horizontal advection ($u\frac{\partial v_g}{\partial z}$ and $v\frac{\partial u_g}{\partial z}$) are significantly enhanced at both directions (Figure V-1a and 1b), because both currents and vertical shears are enhanced. However, net-change ($u\frac{\partial v_g}{\partial z} - v\frac{\partial u_g}{\partial z}$) is minimized by largely compensating each component during July event (N1 and N2), whereas not during August events (S1 and S2), yielding significant net-temperature change (Figure V-1c and d). The net-temperature change due to horizontal advection at the lower depths during S1 event may significantly modify the temporal structure of T_{OBS} departed from T_{CTW}, and may not be negligible. A change of 100 x 10^{-3} cm s^{-2} on the right hand side of equation (5-3) corresponds to 3.2 ˚C/day. There is also no compensation of the temperature changes between along- and cross-shelf directions at the end of S2 event.

The mismatches between T_{CTW} and T_{OBS} during S2 (Figure IV-7b) appear because of the advections of relatively cold and warm waters at depth of around 20 m, e.g., decrease and increase in temperature at 20 m followed by southward and northward currents during S2, (Figure III-2c and 2d). During event S2, southward currents and associate negative vertical shear are dominant at the upper levels (isotherms sloped down toward the coast, increasing water temperature on the near shore bottom,

negative anomaly of the temperature difference in Figure Ⅳ-2c). The cooling induced by such onshore advection of colder offshore water with no compensation of along-shelf temperature advection causes additional temperature changes that could not be predicted by remote wind-forced linear CTW dynamics.

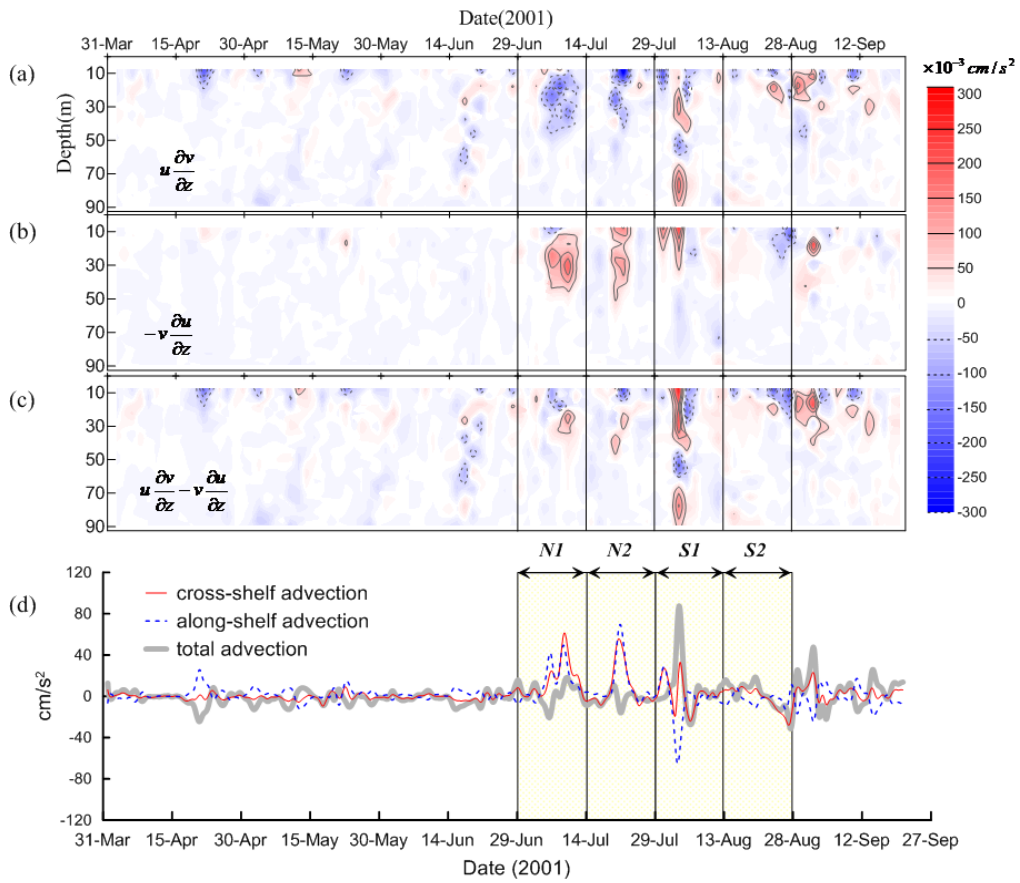

Figure V-1. Time-depth contours of temperature change due to non-linear advections in (a) cross-shelf $u\times(\partial v/\partial z)$ and (b) along-shelf $-v\times(\partial u/\partial z)$ directions, and (c) net-horizontal advection. Solid contour and positive value (dashed contour and negative value) represent warming (cooling). (d) is the depth-averaged fluctuations of (a), (b), and (c).

b. Abrupt change of water properties due to downwelling

A mechanism responsible for the low correlation between T_{CTW} and T_{OBS} during the S1 is needs to be explored detailed. Figure V-2 shows the temperature, salinity, along- and cross-shelf currents, vertical shears of currents by means of contouring, during the four event periods. In order to investigate the variations more minutely, the data is not low-pass filtered (hourly data is used). The S1 event can be divided into two periods when a sudden change in T-S properties is observed (S1a) and when the properties are maintained with amplified diurnal flow oscillations (S1b) (Figure Ⅴ-2). During S1a, both temperature and salinity at lower depths (90, 60, and 40 m) increase in August 2 and then salinity abruptly decrease in August 3 to make the lower water column filled with water mass previously found only in the upper depths, e.g., salinity less than 34.0 (Figures Ⅴ-2 and Ⅴ-3). Such abrupt change accompanies strong southward current ($v < 0$) and downward shift of the core of strong along-shelf current during S1a (Figure Ⅴ-2b). Consequently, negative vertical shear of the along-shelf currents below the core deepens (Figure Ⅴ-2c), which is consistent with deepened isotherms (Figure Ⅴ-2a, Ⅴ-3b, and Ⅴ-3c) considering the cross-shelf geostrophy (Figure Ⅱ-9b).

Such abrupt downwelling during S1a (e.g., isotherm or isopycnal lines sloping down toward the coast and deepening in time) schematized in Figure Ⅴ-3b and Ⅴ-3c accounts for following features observed during the event: 1) flow reversal from northward current to strong southward current, 2) enhanced vertical shear of the along-shelf current, 3) downward shift of the current core and associated change in deepening of iso-shear lines, 4) abrupt freshening (salinity decreases) at the lower depths, and finally 5) increased local rate of temperature change or net-temperature change due to horizontal advection via equation (5-3).

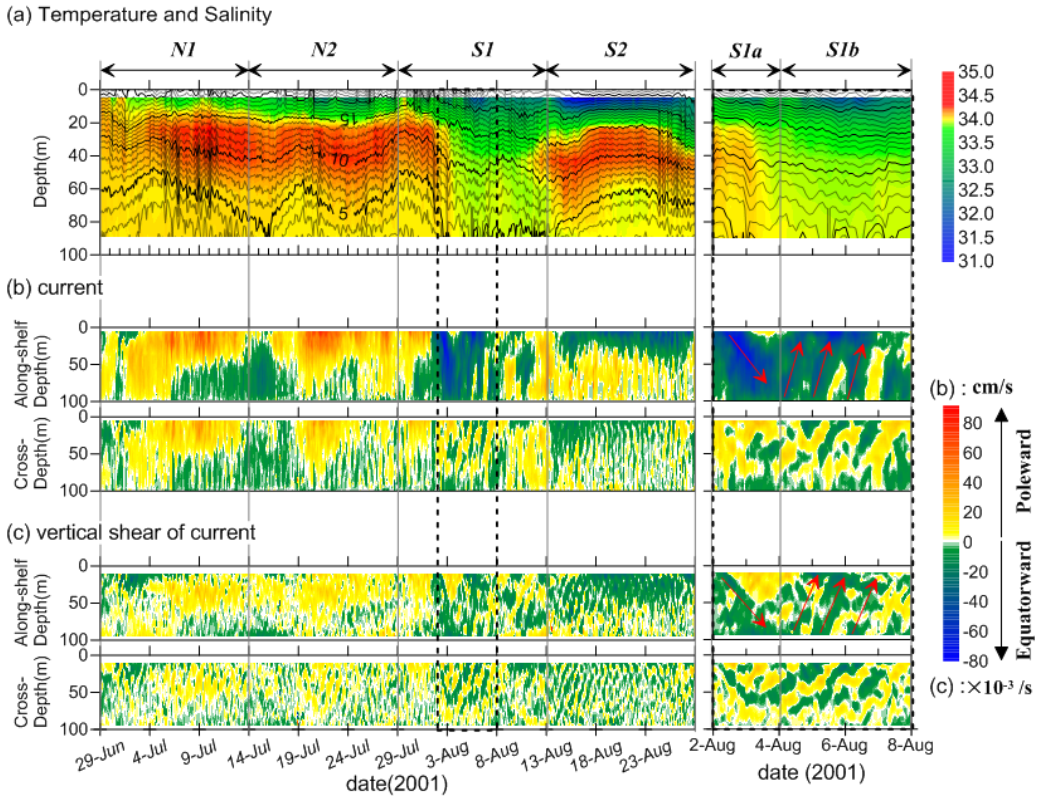

Figure Ⅴ-2. (a) (Left) Temperature (contour) and salinity (color), (b) along-shelf and cross-shelf currents, and (c) vertical shear of along-shelf and cross-shelf currents observed at the mooring (water depth: 100 m) from June 29 to Aug 28, 2001 where four events (N1, N2, S1, and S2) are remarked with vertical bars. (Right) Same but highlighted for S1a and S1b events (see text). Red arrows in (b) and (c) denote downward and upward propagations of along-shelf current and the vertical shear. Contour interval in (a) is 1 ^{o}C.

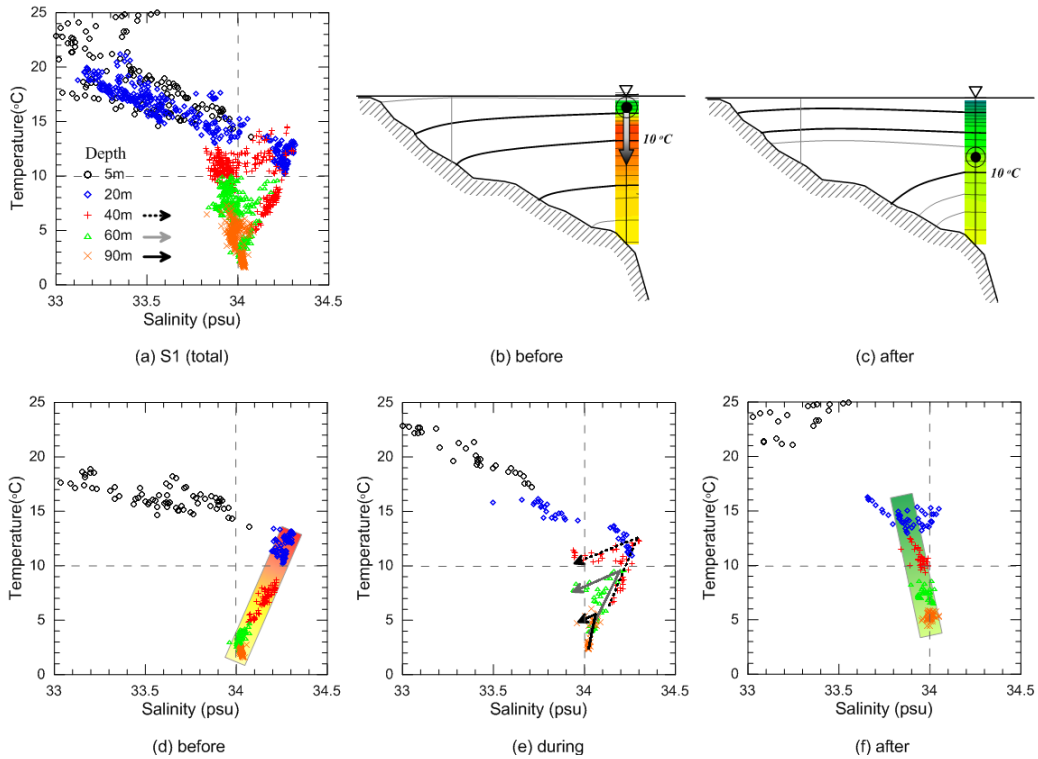

Figure Ⅴ-3. TS-diagrams for (a) total period of S1 event, and (d) before, (e) during, and (f) after downwelling on Aug. 2-3 (see text), characteristics of water mass before (yellow-red box in (d)), during (arrows in (e)), and after (green box in (f)) the downwelling are remarked. Schematics on downwelling; (b) before and (c) after the event where downward movement of current core at the mooring location (symbol) and associate isopycnals sloped down toward the coast (thick and think lines) are shown. In (b) and (c), lines represents isotherms (thick and thin lines are 5 ^{o}C and 1^{o}C interval respectively) and colors denote salinities averaged over the events in the same scale shown in Figure Ⅴ-2a.

c. Eddy heat flux by diurnal oscillations

After the abrupt downwelling, diurnal oscillations in both along-shelf and cross-shelf currents and enhanced shears are amplified and propagate upward during S1b (red arrows in Figure Ⅴ-2b and Ⅴ-2c). Such amplified diurnal oscillations during S1 accompanies diurnal temperature oscillations and currents which are clear and dominant over the total observational period at 90 m of the mooring in the wavelet analysis (Figure Ⅲ-4). It implies an increased horizontal temperature gradient during S1b which is also consistent with the enhanced vertical shear. Time-integration of $T_{IDB} \times v_{IDB}$ at 90 m depth changed 4,800 °C m^2 over 2 days (Figure Ⅴ-4d) which corresponds to 0.24 °C/day over 10 m by 10 m area over the water column of 100 m, and that of $T_{IDB} \times u_{IDB}$ at depths below 60 m reaches up to 44,960 °C m^2 over 15 days (Figure Ⅴ-4e left) corresponding to increase of 0.75 °C/day over the thickness of 40 m (60-100 m) or 0.30 °C/day in T_{OBS}, highlighting significant role of eddy heat flux due to amplified diurnal oscillations in modifying subtidal temperature fluctuations during the period. The abnormal water properties (e.g., low salinity) concurrent with the downwelling are maintained over several days at the lower water column (Figure Ⅴ-2a and Ⅴ-3a) potentially due to significant eddy heat flux associated with enhanced diurnal oscillations (Figure Ⅴ-4). This disturbance of heat flux driven by diurnal oscillations intensively occurred, but the period is not so long compared with the entire time scale.

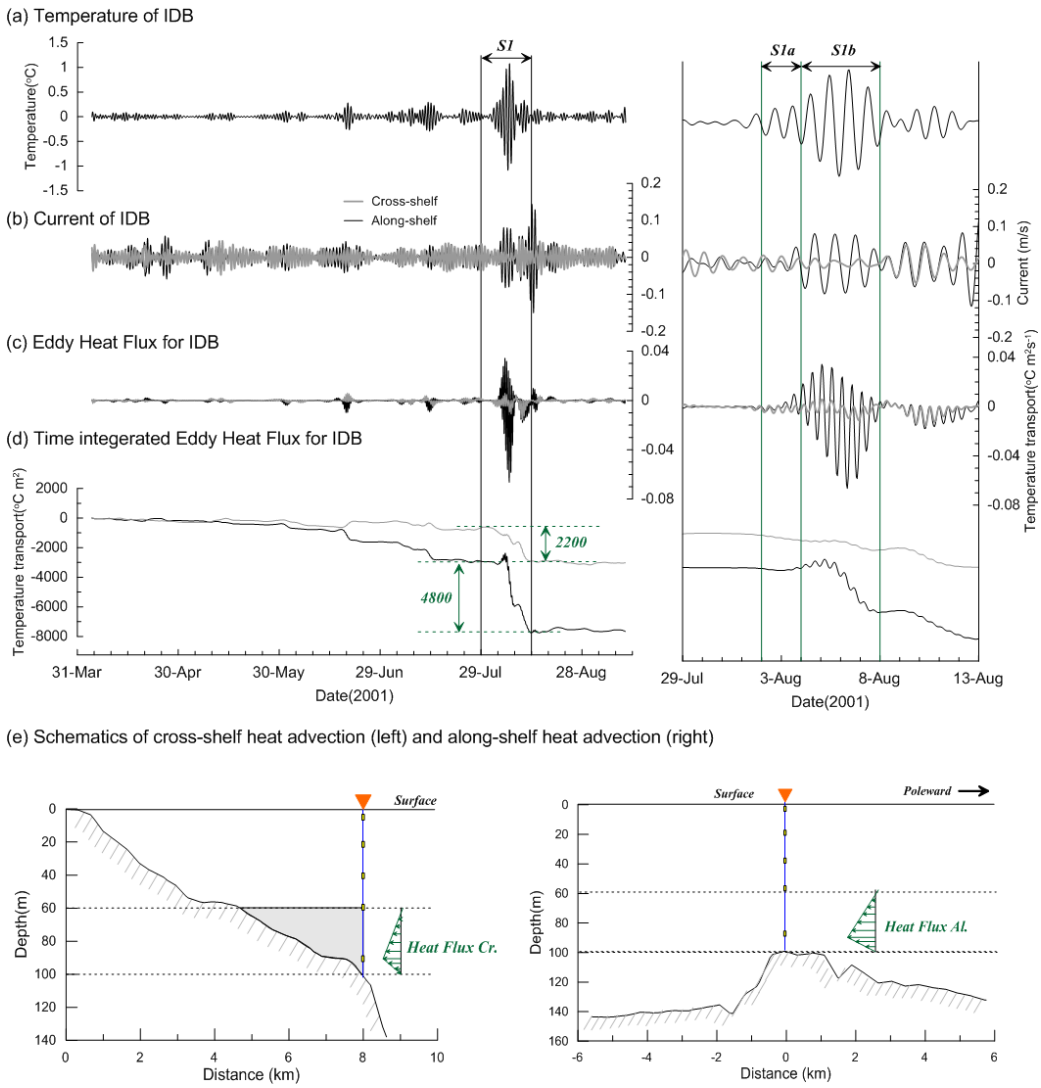

Figure Ⅴ-4. (Left) Time series of IDB band (inertial-diurnal band; periods from 0.79 to 1.17 day) (a) temperature (T_{IDB}), (b) along-shelf (v_{IDB}, black) and cross-shelf (u_{IDB}, gray) currents, (c) $T_{IDB}\times v_{IDB}$ (black) and $T_{IDB}\times u_{IDB}$ (gray), and (d) time integration of $T_{IDB}\times v_{IDB}$ (black) and $T_{IDB}\times u_{IDB}$ (gray) at 90 m. (Right) Same but zoomed-in for the period S1a and S1b. (e) Schematics of heat advection induced by eddy heat flux of cross-shelf (left) and along-shelf (right) direction.

2. Local forcing effects at the inshore site

a. Inner-shelf circulation and nearshore upwelling

Inner-shelf off the east coast of Korea (less than 30 m depth) is subject to frequent upwelling events driven by along-shelf wind stress [Yang, et al. 1998, Lee et al. 2003]. And flow associated with coastal upwelling is often described as a result of a two-dimensional balance between wind-driven offshore flow within a surface boundary layer and a compensating onshore subsurface flow. These flows give rise to generate the cross-shelf circulations. The resulting across-shore pressure gradient then drives an along-shelf flow parallel to the wind [Lentz and Chapman, 2004]. But these studies have not been sufficient to describe the mechanism of the inner-shelf with this two-dimensional calculation of upwelling. Where the western boundary current flows, the bottom fiction over the continental shelf caused reduction of the Coriolis acceleration and allowed the development of an onshore flow near bottom due to the unbalanced pressure gradient [Hsueh and O'brien, 1971].

Four inner-shelf cooling events (E1, E2, E3, and E4 in Figure V-5g) were identified in July as 2-5 day-long periods showing abrupt bottom temperature decreases (< -1.7 ℃/day) at the inshore mooring. Only for E4, wind stress was relatively strong (> 0.05 N/m2) and upwelling-favorable for long time (> 4 days) and the changes in water temperature, sea level, and currents observed are consistent with two-dimensional upwelling circulation. Temperature at 27 m dropped at both moorings (Figure V-5g) with lowered sea levels also both at coastal (Mukho) and inshore stations (Figure V-5f).

During the events E1, E2, and E3, bottom temperature dropped at the inshore mooring with lowered coastal sea levels (Figure V-5g and 5f) similar to those during

E4. Changes in temperature and sea level at offshore mooring, however, differed from those during E4. The sea level variations at coast showed out-of-phase with inshore sea level during E1, E2, and E3 in contrast to the in-phase variations during E4 (Figure V-5d). The out-of-phase variation of the sea level implies an enhanced sea level slope between the inshore mooring and coastal station. Temperature at 27 m changed little or slightly increased at the offshore mooring during E1, E2, and E3. This results in an enhanced temperature difference together with the temperature drops at the inshore bottom (Figure V- 5f), so that the slope of subsurface isotherms between the inshore and offshore moorings gets steeper during the events E1, E2, and E3. Although temperatures at 27 m are generally well correlated between the two moorings, (correlation coefficient is over 0.85), the temperature difference between the moorings becomes larger during E1, E2, and E3 events reaching up to 3.5℃. During the events, vertical shear of along-shelf currents at the offshore mooring was also enhanced (Figure V- 5b). For the whole period, the temperature difference between the moorings is well correlated with the vertical shear of along-shelf currents at the offshore mooring (correlation coefficient=0.87, Figure V-5g), supporting the thermal wind relationship below.

$$\frac{\partial v}{\partial z} = \frac{g}{f}\frac{\partial \rho}{\partial x} \approx \alpha \cdot \frac{g}{f} \cdot \frac{\partial T}{\partial x} \quad \text{---------- (6-1)}$$

where f , g , ρ , T , α are Coriolis parameter, gravitational accelerator, density, temperature and thermal expansion coefficient, respectively.

The cooling events (E1, E2, and E3) at inshore bottom are characterized by steepening cross-shelf slopes of both sea level (lifted up toward the coast, Figure VI-2a) and isotherms (shallower inshore as temperature becomes colder, Figure V- 5g). The events were also concomitant with strong northward currents at the upper levels

with enhanced vertical shear of along-shelf currents at the offshore mooring (Figure V-5b and 5f).

The observed wind at the offshore mooring was northerly during E1, E2, and E3 similar to the period of E4. The magnitude and duration of the winds, however, were weak and short as compared to those during E4, so that the temperature variations at the offshore mooring during the first three events showed no indication of the upwelling like the one observed during E4. Hence, the observed drops of bottom temperature at the inshore bottom and of sea level at the coast are not wind-driven.

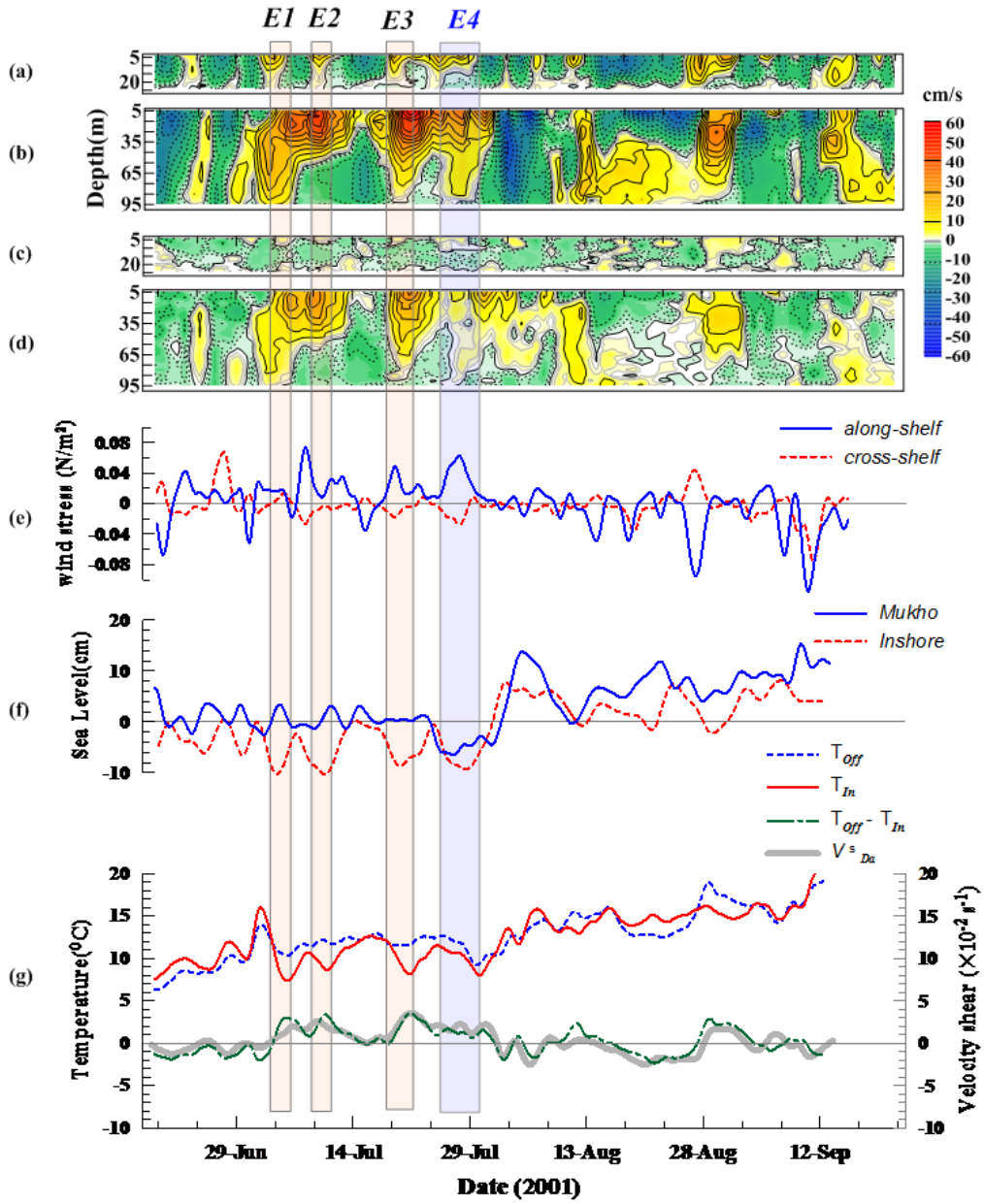

Figure V-5. Along-shelf and cross-shelf currents observed at 27 m depth inshore ((a) and (c), respectively) and 100 m depth offshore moorings (((b) and (d), respectively) from 18 June to 13 September 2001. Along-shelf and cross-shelf wind stresses (solid and dashed lines in (e)), sea level at the coastal station (Mukho, solid line in (f)) and bottom pressure at the inshore mooring (dashed line in (g)). The cooling events (E1, E2, E3 and E4) at the inshore bottom are marked with the four rectangles.

b. Nearshore upwelling driven by offshore currents

Currents, water temperatures, pressures, and sea levels observed during the E4 indicate typical, two-dimensional (cross-sectional) local wind-forced upwelling circulation. Upwelling-favorable wind stress during the event (Figure Ⅳ-3b) can lower the sea levels at both coastal station and inshore location (Figure Ⅳ-3c) by the seaward Ekman transport at the upper levels (Figure Ⅳ-3a-3 and 3a-4), and cause temperature drops (lifting up isotherms) at both inshore bottom and the same depth of offshore location (Figure Ⅳ-3d). Figure Ⅴ-6b demonstrates the cross-sectional circulation on the continental shelf during the E4. The seaward transport (per unit along-shelf distance) at the upper layer (5~13 m) on the inshore location is 0.049 m^3/s, exactly equal to the shoreward transport at the lower layer (13~27 m) and 1.070 m^3/s less than that on the offshore location (1.119 m^3/s over the layer of 5~40 m), yielding a volume of upwelled water of 462,423 m^3 over the 5 days period of event. Resultant vertical velocity of 0.019 cm/s accounts for temperature changes of -3.48˚C over the period, consistent with our observation at both locations (Figure Ⅴ-5g).

In contrast to the upwelling case observed during the E4, nearshore upwelling events were observed in E1, E2, and E3 regardless of onset of local along-shelf wind forcing. During the E1, E2, and E3, sea level on the inshore site became significantly lower than that at the coast (Figure Ⅳ-1c), and temperature decreased only at inshore location enhancing cross-shelf temperature difference (Figure Ⅳ-1d), indicating shoaling up of isotherms at the inshore location (Figure V-6a). During the E2, vertical structure of cross-shelf currents at the inshore location supports parabolic shape, contrasting to first baroclinic profile during the E4, yielding shoreward transport of

0.13 m^3/s at the middle layer (9-22 m) that much exceeds seaward transport of 0.03 m^3/s above it. This, combined with strong seaward transport at the upper levels (7.17 m^3/s over the layer of 5~55 m) and steepened sea surface and (opposite) isotherm slopes (sea surface slope was enhanced up to 6.0×10^{-5}, and temperature difference between the two location corresponds to isotherm slope of 3.0×10^{-3}), explains the onshore bottom flow to the coast and supporting inner-shelf upwelling cell shown in Figure V-6a.

Moreover, accompanied during the E2 were strong northward current and associate vertical shear of along-shelf current on the offshore location (Figure V-5b) that are well balanced with cross-shelf temperature difference via thermal wind relationship (Figure V-5g). The steep isotherms during the E2 were primarily due to huge temperature drops at the inshore bottom (against temperature increase at the offshore location). Local time rate of change of inshore bottom temperature, -0.8 ˚C/day, exceeds the magnitude of maximum rate (occurred at 36m depth) of change of offshore temperature of +0.4 ˚C/day. Thus, the coastward flow affects stronger on the inner-shelf, combined with strong northward current offshore (Figure V-5a).

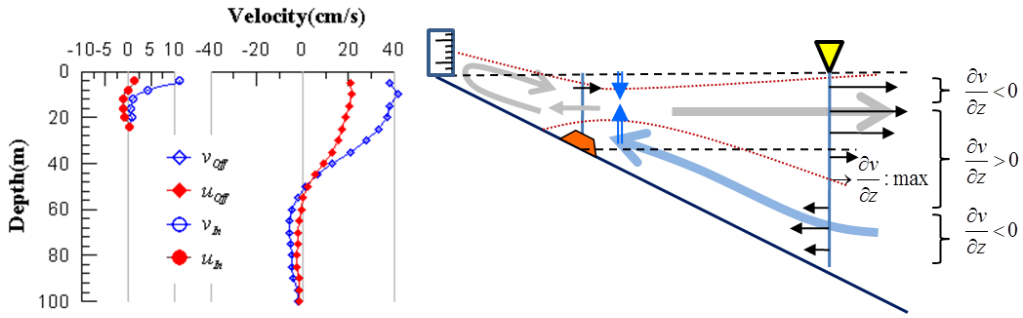

(a) Velocity profiles(left) and schematics(right) in case of E2

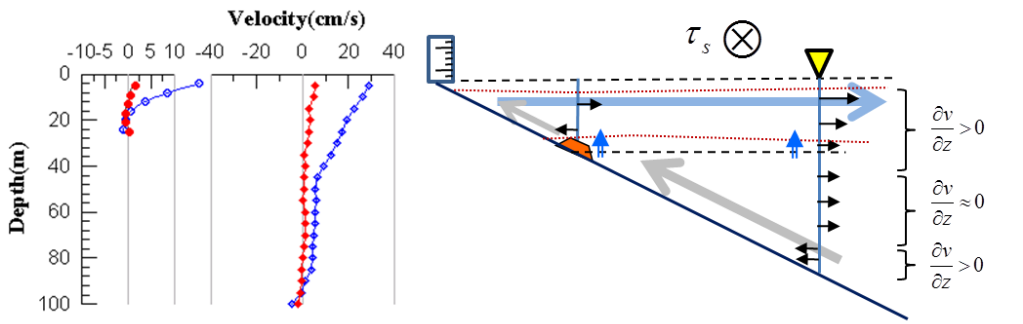

(b) Velocity profiles(left) and schematics(right) in case of E4

Figure V-6. Vertical profiles of along-shelf and cross-shelf currents (left) and schematic diagrams showing two different nearshore upwelling processes, (a) driven by the offshore forcing (E2), and (b) driven by local along-shelf wind stress (E4). The currents are time averaged for the each event period. The isotherm and sea level are shown with dashed line (initial state) and dotted line (final state). Arrows denote cross-shelf currents (black) and circulation (thick gray), and vertical motion (double line arrow).

Chapter Ⅵ. Discussion

1. Capability and limitation of CTW model

It has been a question that observed speeds of sea level propagation along the east coast of Korea disagree with (three times faster than) the phase speeds derived from the continental shelf wave theory, e.g., 1.6 m/s between SC and MH, and 2.6 m/s between MH and PH [Lee and Chung, 1982]. That is, such (relatively) fast sea level propagation observed along the coast cannot be explained by the barotropic shelf wave theory without consideration of stratification, e.g., excluding Kelvin waves. Due to the effects of basin-scale oscillations, every single event in the observed sea level does not agree with the phase speed of CTW model [Lyu et al., 2002; Nam et al., 2004; Park et al., 2005; Inazu et al., 2005]. In the aggregate, observed propagation speeds between SC and MH (6.1 m/s) and between MH and PH (10.4 m/s) (Table III-1) are, however, consistent with those of first mode CTWs at Seg.5 (4.6-5.9 m/s) and Seg.6 (9.5-10.3 m/s) (Table IV-1). First mode CTWs clearly show baroclinic structures with one or more zero-crossings at shallow depths (Figure IV-5). The stratification is thus suggested to be one of important keys to understand the propagation of subtidal sea level fluctuations along the east coast of Korea. The model applications with use of different stratifications for three periods (Periods 1, 2, and 3) could not account for changes in propagation speed of the observed sea level among different seasons (Table IV-1).

Besides the August events (S1 and S2 in Table IV-3), there are mismatches between T_{OBS} and T_{CTW} in April 7-15, April 20 - May 2 and June 5-20 in Figure IV-7b. These mismatches could be caused by modification of observed water temperature due to many processes beyond the CTW dynamics and reflect generally well-known

limitations of the CTW model to predict density or water temperature. Nevertheless, the model practically reproduces some (though not all) subtidal temperature fluctuations observed off the mid-east coast of Korea during the stratified season. The results also support Pringle and Riser [2003] suggesting that remote (rather than local) wind forcing is responsible for most of the observed fluctuations in nearshore water temperature by analyzing observations in the nearshore zone off southern California. These results have a significant implication on the CTW studies on shelves inside a semi-enclosed basin where the CTW model has not been widely verified with observations and has not been expected to work well due to frequent presence of strong mean flows.

The first mode CTWs takes a dominant role in reproducing water temperature fluctuations (correlation between T_{OBS} and T_{CTW} are rather insensitive to choice of modes, Table IV-3), i.e. the second and third modes CTWs does not significantly improve the predictions. The propagation of remote-wind forced, first mode CTW plays an important role in driving subtidal temperature fluctuations off the mid-east coast of Korea. High correlations between T_{OBS} and T_{CTW} are still maintained during the periods of strong mean currents (N1 and N2 events), but T_{OBS} and T_{CTW} are anti-correlated (negative correlation coefficients) during the events of S1 and S2, again implying that other processes affect the temperature fluctuations.

2. Effects of local nonlinear advection on the predictions by CTWs

Coastal trapped wave is a hybrid wave which contains the characteristics of Kelvin wave and topographic wave (topographic Rossby wave) types. In the continental

shelves of real oceans, it is not strictly separated into the two types, so that the CTW has been considered as the more general wave form which can be existed on the shelves off many continental margins. However this physical mechanism has not been applied to the East Sea, because the strong local current can add the nonlinear effects on the CTW mechanism which is approximated into a linear form to compute the solutions of the CTW mechanic system [Brink 1991]. The nonlinear advection can bring about the negative effect on the predictions of the temperature variations which demonstrated by CTW model (Figure IV-7b). Particularly, the presence of a mean along-shelf flow over the continental margin can alter the free-wave properties through Doppler shifting, modification of the background vorticity field, and then give rise to the growth of instabilities [Brink 1990]. Moreover, when the coastal-trapped waves propagate in the opposite direction to that of the mean current (e.g. N1 and N2), the direction of wave propagation is locally reversed owing to the strength of the mean flow [Gill & Schumann, 1979].

There are no steady mean flows in this study area, but strong currents are occasionally appeared due to the regional-scale circulations. But, the nonlinear advections by the currents are not always distorting the liner mechanic systems. In some cases, the nonlinear advection effects are reduced not to change the heat budget on the water column. The case is that heat advections in the along-shelf direction are compensated to near zero with those in the cross-shelf direction (N1 and N2 in Figure Ⅴ-c and d). In case of $u\frac{\partial v}{\partial z} = v\frac{\partial u}{\partial z}$, the thermal wind equation (5-4) comes to be zero and the temperature changes due to the local nonlinear heat advection can be ignored.

3. Subtidal temperature variations due to diurnal oscillations

Addressing physical driver(s) of the transient downwelling and amplification of diurnal oscillations during S1 is still not closed and laid for future study. Potential interactions between subtidal shear and diurnal oscillations (internal waves) [e.g., Nam and Send, 2013] and/or between bottom slope and internal waves/tides [e.g., Nam and Send, 2011] seen on other shelves may be considered. Note that local wind does not seem to be responsible for triggering the event since the data show no significant downwelling-favorable wind (S1 in Figure III-2a) nor strong diurnal sea/land breeze during or prior to the periods (Figure III-4a). However, in the mid-May, the diurnal oscillations of the along-shelf/cross-shelf wind, cross-shelf currents, and temperatures (20 m depth) are considerably amplified (Figure III-4). In this period, the daily changes of wind in the shelf area (e.g. the land-sea breeze) can be a forcing to generate the eddy heat flux. But the transient process of the energy from the surface wind stress to the change of temperature at 20 m depth is not explored yet.

Another interesting interruption in S1a is found in the currents structure of the lower layer (depth range from 60 m to 90 m), which is including the strong bottom current (> 30 cm/s at 85 m depth) and cannot be ignored, compared with the upper/middle currents (Figure III-2c). Below the thermocline depth, the lower layer becomes more unstable easily, i.e. the Bulk Richardson number ($Ri_b = N^2/S^2$ (N: bouncy frequency, S: vertical current shear)) decrease to O(1) (Figure VI-1). Then the possibility of vertical mixing increases due to the strong bottom current.

Nevertheless, it is suggested that the advective and diffusive heat fluxes associated with abrupt downwelling (S1a) and amplified diurnal oscillations (S1b) respectively are ones of the primary mechanism to modify temporal structure of subtidal

temperature fluctuations off the mid-east coast of Korea, departing from those predicted by remote wind-forced CTW model.

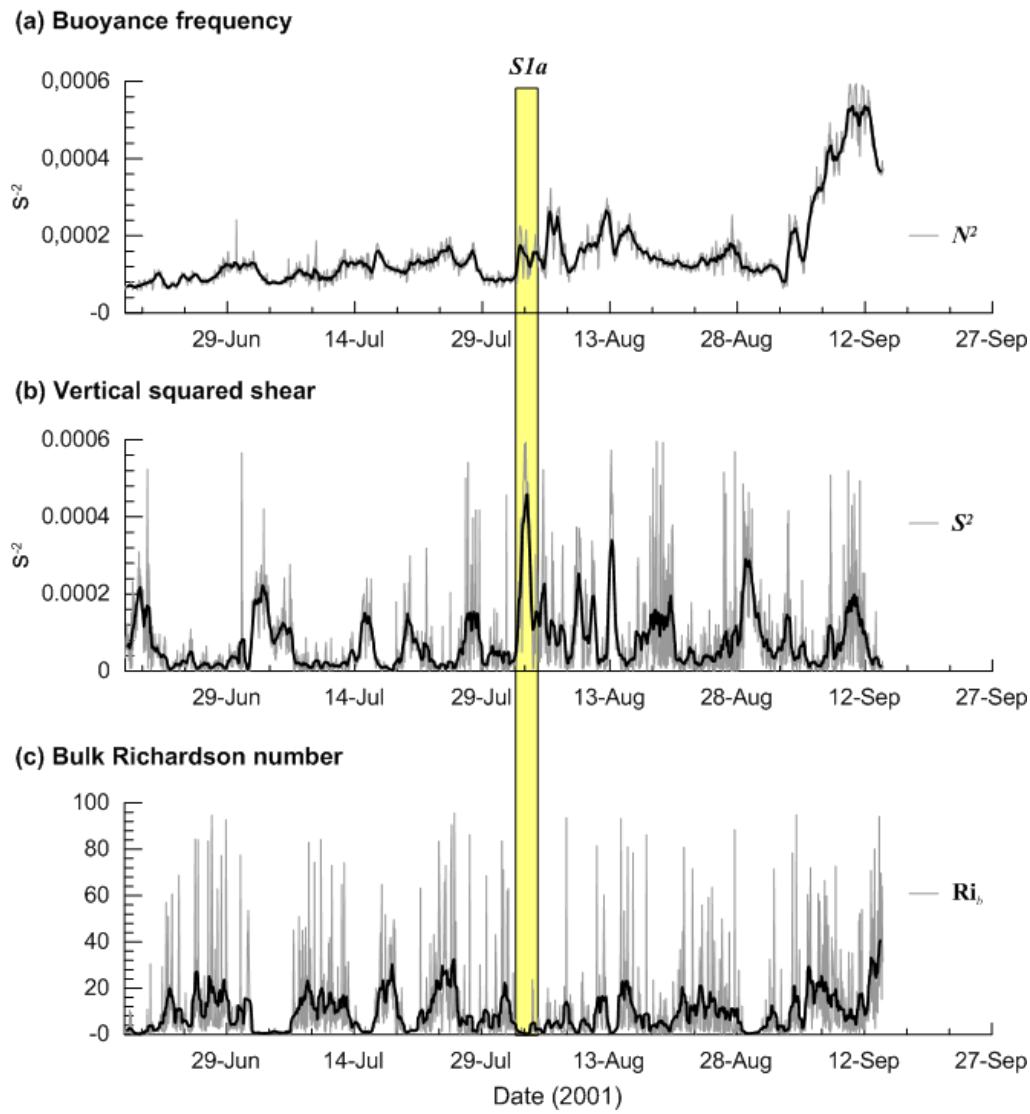

Figure VI-1. Buoyancy frequency squared between 60 m and 90 m depth (a) and vertical squared shear (S^2) depth averaged range from 60 m to 90 m (b). The bulk Richardson number calculated by N^2 and S^2 (c). The gray lines are 1 hour interval data and the thick black (solid and dot) lines are 15-hour running averaged.

4. Subtidal water temperature variations in the inner-shelf area driven by offshore along-shelf current.

The inshore bottom cooling events of E1, E2, and E3 did not show characteristics of local-wind forced circulation like event E4. During these three events, sea levels on the inner shelf (inshore mooring) were significantly lower than that at the coast (Mukho) only 2.3 km apart (Figure V-5f), and temperature decreased only at the inshore bottom not in the offshore mooring site (Figure V-5g) resulting in an enhancement of cross-shelf temperature difference. Those variations indicate the suppression of sea level and lifting of isotherms at the inshore mooring as schematically shown in Figure V-6a. In this case, the cold water mass at offshore (near bottom) flows into shoreward as shown in Figure VI-2a (light blue arrows), and the water mass is piled up in the inner shelf region, arising the sea level at the coast. Due to this sea-level difference in the inner-shelf area, seaward flow can be generated at surface layer. As a result of the coastward bottom flows and the seaward one at surface, the cross-shelf circulation in the inner-shelf area is developed. This onshore flow was reported by Hsueh and O'brien [1971] related to the vertical shear induced by the northward western boundary currents, but the effects were not extended to the inner-shelf area. The reason of this limitation may be the large scale of the offshore current (western boundary current) and the long offshore distance of forcing from the inner-shelf area. However, the shelf area off the east coast of Korea is characterized as the narrow width and strong along-shelf currents.

It is known that there is strong northward currents, e.g. EKWC, off the east coast of Korea in spring and summer, which transports Tsushima Middle Water (TMW) having the properties of high temperature (> 15˚C) and high salinity (>34.20 psu) [Kim and Kim, 1983]. The water properties observed during the periods from E1 to E4

correspond to the TMW [Cho and Kim, 1994] (Figure V-3f). Therefore, it is inferred that the offshore forcing to enhance the vertical shear of along-shelf current during the E1, E2 and E3 would be the onshore meandering of the EKWC (Figure VII-3).

It was explained the high correlations (> 0.87) between the difference of the horizontal temperatures and the depth-averaged vertical shears in terms of the geostrophic balance (Figure V-5g). In this relation, the horizontal differences of temperatures between inshore and offshore are mainly represented by the change of the inshore bottom, which itself has a good correlation with vertical shear of currents. In other words, the subtidal temperature fluctuations at inshore bottom are strongly related with the offshore-along-shelf current (or its vertical shear). The structures of the vertical shears of the along-shelf currents are presented in Figure VI-2a. It can be separated into the three layers; upper (5~20 m depth), middle (20~60 m depth), and lower (60~90 m depth) layer, according to the vertical structure of the shears. Particularly, it seems like that the inshore bottom temperature does directly response to the shear of the middle layer (Figure VI-2b), but the relation becomes weaker after 13-Aug.

It suggests that the nearshore upwelling can be driven by the offshore along-shelf currents and enhanced vertical shear, but the interior circulation within inner-shelf region is need to be further investigated.

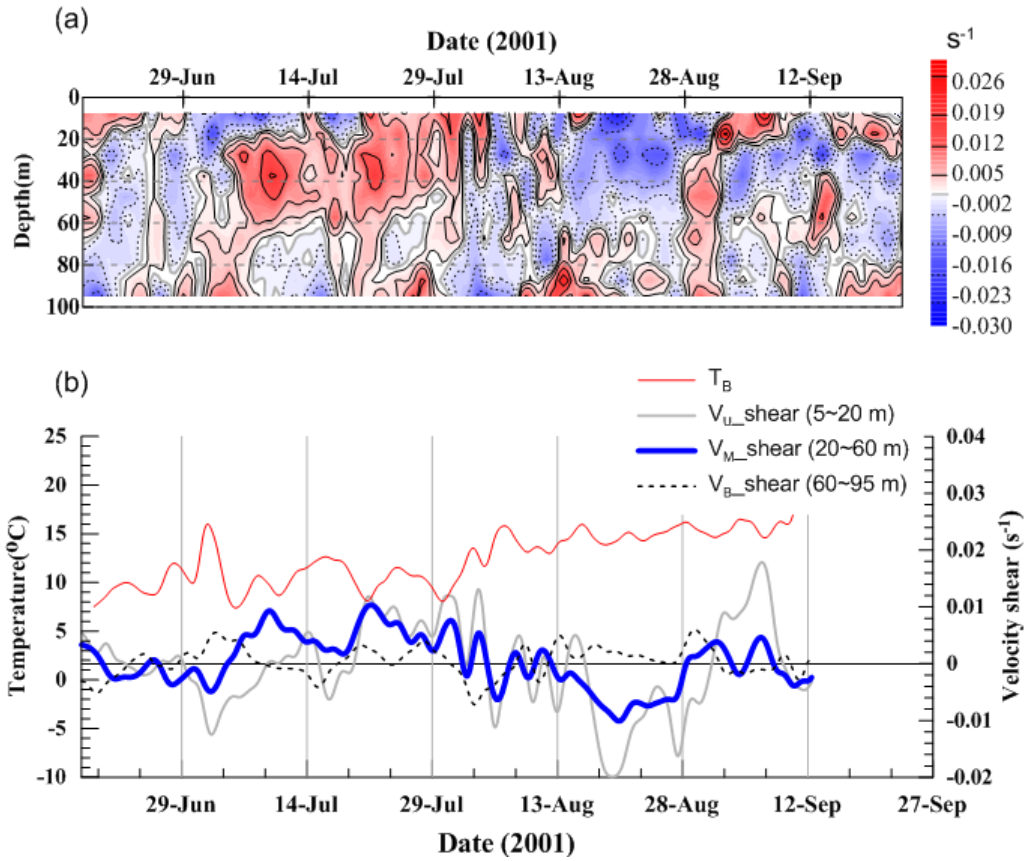

Figure VI-2. D(a) Depth-time contours of the vertical shear of along-shelf current and (b) time series of the bottom temperature at inshore bottom (solid line) and three depth-range averaged of vertical shear of along-shelf current (grey line; range from 5 to 20 m, thick line; 20 to 60m, and dashed line; 60 to 90 m). The ranges of the three layers is based on the vertical structures in (a), roughly.

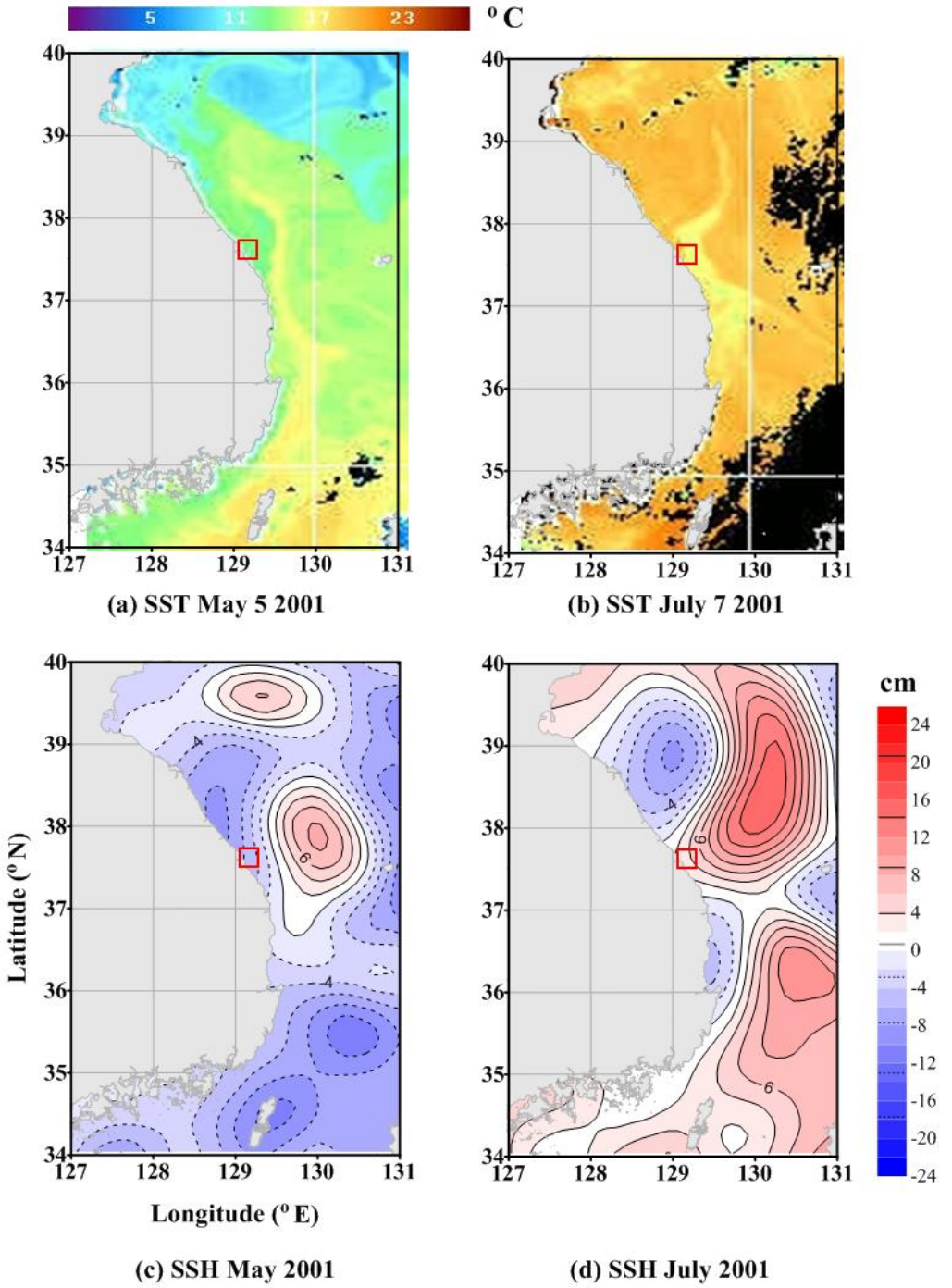

FigureVI-3. Sea Surface Temperature (SST) in May 5 (a) and July 7 (b) in 2001 and Sea Surface Height (SSH) in May 2001 (c) and July (d) in 2001. SST is a snap shot of the day observed data and the SSH is a monthly mean data (AVISO).

Chapter VII. Conclusion

Subtidal temperature fluctuations in stratified waters off the east coast of Korea are examined by use of the wind-forced coastal trapped wave (CTW) model and observations of velocity shear, water temperature, and sea level elevation. Phase speeds computed from the CTW model (4.6-5.9 and 9.5-10.3 m/s off northern and southern coasts respectively) are consistent with the observed speeds (6.1 and 10.4 m/s respectively) of sea level propagation along the coast. The temperatures from the model (T_{CTW}) are compared with those from observations (T_{OBS}), and the relationship between the temperatures from both and the observed current structures are examined. These suggest that the subtidal temperature fluctuations are not only driven by wind-forced CTWs but also affected by local nonlinear temperature advection associated with regional-scale circulation. During events of significant local advection, correlations between T_{CTW} and T_{OBS} may or may not drop, depending on the vertical structure and direction of along- and cross-shelf currents, because onshore and along-shelf advections of cold water cause a significant drop in temperature. It should be noted that regardless of the CTW dynamics (S1 and S2) this mechanism generally explains the above correlations unless the cross-shelf advection is compensated by the along-shelf advection (N1 and N2) off the east coast of Korea. The extendable application of CTW model to the long period (six years : 2006 ~ 2011) supports that the propagations of CTWs due to the remote wind forcing have a significant influence on the subtidal water temperature variations. The yearly averaged correlation coefficients between the T_{OBS} and T_{CTW} for the six years are 0.39 (on the basis of mean of maximum correlations of the respective months) and the matching rates of time series of T_{OBS} and T_{CTW} are higher in winter than in summer.

It is also suggested that an abrupt change in water properties (based on T-S relationship) is caused by sudden downwelling (S1a) and subsequent amplification of diurnal oscillations (S1b), which is the possible mechanisms responsible for the modified temporal structure of temperature. The abrupt downwelling is also explained by a breaking of geostrophic balance. Such processes, i.e. increasing of ageostrophy appear to have profound impacts on the subtidal temperature fluctuations beyond CTW dynamics.

A possible mechanism is proposed that the underlying inner-shelf circulation process on a narrow shelf is driven by the offshore forcing, i.e., onshore flows at bottom layer/baroclinic tilting is induced by the enhanced vertical shear of offshore along-shelf current. From the offshore boundary of the inner-shelf toward the coast, the shoreward cross-shelf flow emerges, leading to an increase in the coastal sea level. According to this mechanism, nearshore upwelling can be generated by neither local wind stress nor other forcing mechanisms, but by along-shelf currents at offshore region. Analysis of water temperature, current, sea level, and bottom pressure data collected near and off the east coast of Korea clearly shows that upwelling can be induced by both the onshore bottom flow induced by offshore current and the along-shelf wind stress. The coastward flow causes to pile up the water mass at coast and it can be connected to inner-shelf circulation. Nearshore upwelling can occur when a northward offshore current such as the EKWC meanders toward the east coast with an enhanced vertical shear of along-shelf current in summer.

The observation reveals how the nonlinear advection plays a role in subtidal temperature variability of stratified coastal water inside the deep basin beyond the wind-forced CTW dynamics. As previously suggested [e.g., Brink, 1991], an application of CTW formalism under the condition of strong local current cannot

guarantee a good correlation with the observations. However, it is also shown that the subtidal temperature variability can be well predicted by the remotely wind-forced CTW model, even in the case of strong local current if along-shelf advection is compensated by cross-shelf one. Consequently, this study suggests that subtidal water temperature variability off the east coast of Korea can be mainly predicted by linear CTW dynamics particularly when the local advections are prescribed from regional-scale circulation.

References

Allen, J. S. (1980), Models of wind- driven currents on the continental shelf. *Annu. Rev. Fluid Mech.* 12: 389-433

Akima, H., (1969), A method of smooth curve fitting, ESSA Tech. Rep. ERL 101-ITS 73.

Battisti, D. S. and B. M. Hickey (1984), Application of remote wind-forced coastal trapped wave theory to the Oregon and Washington coasts. *J. Phys. Oceanogr.*, 14, 887-903.

Brink, K. H., (1982), A comparison of long coastal trapped wave theory with observations off Peru. J. Phys. Oceanogr. 12: 897-913

Brink, K. H. (1989), Energy conservation in coastal-trapped wave calculations. *J. Phys. Oceanogr.*, 2, 1011–1016.

Brink, K. H. (1990), On the damping of free coastal-trapped waves. *J. Phys. Oceanogr.*, 20, 1219–1225.

Brink, K. H. (1991), Coastal-trapped waves and wind-driven currents over the continental shelf. *Ann.l Rev. of Flu. Mecha.*, 23, 389-412.

Brink, K. H. and D. C. Chapman (1987), Program for computing properties of coastal-trapped waves and wind-driven motions over the continental shelf and slope. Woods Hole Oceanographic Institution. Tech. Rep. WHOI-87-24, 122 pp.

Chapman, D.C., (1987), Application of wind-forced, long, coastal-trapped wave theory along the California coast. *J. Geophys. Res* 92, 1789–1816..

Cho, C.B., S. H. Nam, and K. I. Chang, (2014), Subtidal temperature variability in stratified shelf water off the mid-east coast of Korea, Con. Shelf Res., 75, 41-53.

Cho, Y.K. and K. Kim (1994), Seasonal variation of the East Korea Warm Current and its relation with the cold water, *La Mer*, 34, 172-182.

Choi, B.-J., D. B. Haidvogel, and Y.-K. Cho (2004), Nonseasonal sea level variations in the Japan/East Sea from satellite altimeter data, *J. Geophys. Res.*, 109, C12028, doi:10.1029/2004JC002387.

Fewings, M., S. J. Lentz and J. Fredericks (2008), Observations of Cross-shelf Flow Driven by Cross-Shelf Winds on the Inner Continental Shelf, *J. Phys. Oceanogr.*, 38, 2358-2378.

Fewings, M., P. Howd, J. Fredericks, and K. Hathaway (2008), Observations and a model of undertow over the inner continental shelf. *J. Phys. Oceanogr.,* 38, 2341–2357.

Freeland, H.J., F.M.Boland, J.A. Church, A.J. Clarke, A.M.G. Forebes, A. Huyer, R.L.Smith, R.O.R.Y. Thompson and N.J. White (1986), The Australian Coastal Experiment: A Search for Coastal-Trapped Waves. *J. Phys. Oceanogr.,* 16, 1230–1249.

Gibbs, M. T., J.H. Middleton, and P. Marchesiello (1998), Baroclinic Response of Sydney Waters to Local Wind and Deep Ocean Forcing. *J. Phys. Oceanogr.*, 28, 178–190.

Gill, A. E. (1982) Atmosphere-Ocean Dynamics *Academic Press, Inc.*, New York.

Gill, A. E., and E. H., Schumann (1974), The generation of long shelf waves by the wind *J. Phys. Oceanogr*. 4, 83-90

Gill, A. E., and E. H., Schumann (1979), Topographically induced changes in the structure of an inertial coastal jet: application to the Agulhas Current, *J. Phys. Oceanogr*. 9, 975-991.

Griffin, D. A. and J. H. Middleton (1991), Local and remote wind forcing of New South Wales inner-shelf currents and sea level. *J. Phys. Oceanogr.*, 21, 304-322.

Huthnance, J. M., L. A. Mysak, D. P. Wang (1986) Coastal trapped waves, in: Mooers, C. N. K. (Eds.), Baroclinic Processes on Continental Shelves, Coastal Estuarine Sci., 3, AGU, Washington, D.C, , pp. 1-18.

Hsueh, Y. and J. J. O'brien (1971) Steady Coastal Upwelling Induced by an Along-Shore Current, *J. Phys. Oceanogr.*, 1, 180–186.

Inazu, D., H. Naoki, S. Kizu, K. Hanawa (2005), Zonally Asymmetric Response of the Japan Sea to Synoptic Pressure Forcing , *J. Oceanogr*., 62, 909-916.

Johnson, E.R., (1991), The scattering at low frequencies of coastally trapped waves. *J. Phys. Oceanogr*., 21, 913–932.

Jordi, A., A.Orfila, G.Basterretxea, J. Tintore (2005), Coastal trapped waves in the northwestern Mediterranean, Con. Shelf Res., 25, 185-196.

Kim, H. J., Y. G. Park, and K, Kim (2005), Generation mechanism of the near-inertial interal waves observed off the east coast of Korea, Cont., Shelf Res., 25, 1712-1719.

Kim, H. R., S. Ahn, K. Kim (2001), Observation of highly nonlinear internal solitons generated by near-inertial internal waves off the east coast of Korea. *Geophys. Res. Lett*., 28(16), 3191-3194

Lentz, S. J., and D. C. Chapman (2004), The Importance of Nonlinear Cross-Shelf Momentum Flux during Wind-Driven Coastal Upwelling, *J. Phys. Oceanogr.*, 34, 2444–2457.

Lentz, S. J. and J. R. Austine (2008), The Inner Shelf Response to Wind-Driven Upwelling and Downwelling, *J. Phys. Oceanogr.*, 32, 2171–2193.

Lentz, S. J., R. T. Guza, S.Elgar, F.Feddersen, and T. H. C. Herbers (1999), Momentum balances on the North Caolina inner-shelf, *J. Geophys. Res.*, 104, 18205-18226

Lentz, S. J., (1994), Current dynamics over the northern California inner-shelf. *J. Phys. Oceanogr.,* 24, 2461–2478.

Lentz, S. J., M. Fewings, P. Howd, J. Fredericks and K. Hathaway (2008), Observations and a Model of Undertow over the Inner Continental Shelf, *J. Phys. Oceanogr.*,38, 2341-2357.

Lee, J. H. and J. Y. Chung (1982), A continental shelf waves off the eastern coast of Korea, *La Mer*, 20, 169-180.

Lee, J. C., and J. Y. Na (1985), Structure of Upwelling off the Southeast Coast ofKorea, *J. Kor. Soc. Oceanogr.*,, 20 (3), 6-19.

Lee, J. C., D. H. Kim, and J. C. Kim (2003), Observations of Coastal Upwelling at Ulsan in summer 1997, *J. Kor. Soc. Oceanogr.*,, 38 (3), 122-134.

Lim, D.B., and S.D. Chang (1969), On the cold water mass in the Korea Strait, *J. Kor. Soc. Oceanogr.*,,4, 71-82.

Lyu, S. J. and K. Kim (2005): Subinertial to interannual transport variations in the Korea Strait and their possible mechanisms. J. Geophys. Res., 110, C12016, doi:10.1029/ 2004JC002651.

Lyu, S. J., K. Kim, and H. T. Perkins (2002), Atmospheric pressure-forced subinertial variations in the transport through the Korea Strait, *J. Geophys. Res.*,, 29, 1294, doi:10.1029/2001GL014366.

Mitchell, D.A., Watts, D.R.,Wimbush,M.,Teague, W.J.,Tracey, K.L., Book, J.W., Chang, K.-I., Suk, M.-S., Yoon, J.-H. (2005), Upper circulation patterns in the Ulleung Basin, Deep-Sea Research II 52, 1617-1638.

Mitchum, G. T., and A. J. Clarke, (1986), The frictional nearshore response to forcing by synoptic scale winds. *J. Phys. Oceanogr.,* 16**,** 934–946.

Nam, S. H., Park, J.-H.,(2008), Semidiurnal internal tides off the east coast of Korea inferred from Synthetic Aperture Radar images, *Geophys. Res. Lett*., 35, L05602, doi:10.1029/2007GL032536.

Nam, S. H., Send, U. (2011), Direct evidence of deep-water intrusions onto the continental shelf via surging internal tides, J. Geophys. Res., 116, C05004, doi:10.1029/2010JC006692.

Nam, S. H., Send, U. (2013), Resonant diurnal oscillations and mean alongshore flows driven by sea/land breeze forcing in the coastal Southern California Bight, J. Phys. Oceanogr., 43 (3), 616-630, doi:10.1175/JPO-D-11-0148.

Nam, S. H., Lyu, S. J., Kim, Y. H., Kim, K., Park, J.-H., Watts, D. R. (2004), Correction of TOPEX/POSEIDON altimeter data for nonisostatic sea level response to atmospheric pressure in the Japan/East Sea, *Geophys. Res. Lett*., 31, L02304, doi:10.1029/2003GL018487.

Nam, S. H., Y. H., Kim, K. -A., Park, K.,Kim (2005a). Spatio-temporal variability in sea surface wind stress near and off the east coast of Korea. Act. Oceanol.Sin., 24 (1).107-114.

Nam, S. H., Kim, G.,Kim, K.-R., Kim, K.,Cheng, L. O., Kim, K.-W., Ossi, H.,Kim, Y.-G. (2005b), Application of real-time monitoring buoy systems for physical and biogeochemical parameters in the coastal ocean around the Korean peninsula. Mar. Tech. Soc. J., 39 (2), 54-64.

Nam, S. H., Kim, D. -J., Kim, H. R., Kim, Y.-G. (2007), Typhoon-induced, highly nonlinear internal solitary waves off the east coast of Korea, Geophys. Res. Lett., 34, L01607, doi:10.1029/2006GL028187.

Palma, E.D., R. P. Matano, and A. R. Piola (2008), A Numerical Study of the Southwestern Atlantic Shelf Circulation, *J. Geophys. Res.*, 113, C11010, doi:10.1029/2007JC004720.

Park, J.-H., and D. R. Watts (2005), Near-inertial oscillations interacting with mesoscale circulation in the southwestern Japan/East Sea, *Geophys. Res. Lett.*, 32, L10611, doi:10.1029/2005GL022936.

Park, K. A., K. R. Kim, K. Kim, J. Y. Chung, and P. C. Cornillon (2003), Comparison of the wind speed from an atmospheric pressure map (Na wind) and satellite scattorometer-observed wind speed (NSCAT) over the East (Japan) Sea, *J. Kor. Soc. Oceanogr.*,, 38 (4), 173-184.

Pond, S., and G. L. Pickard, (1983), Introductory Dynamical Oceanography, 2d ed. *Pergamon Press*, 328.

Pizarro O. and G. Shaffer (1998), Wind-driven, coastal-trapped waves off the island of Gotland, Baltic Sea, *J. Phys. Oceanogr.*, 28, 2117-2129.

Pringle, J. M. and K. Riser (2003), Remotely forced nearshore upwelling in Southern California, *J. Geophys. Res.*, 108(C4), .3131, doi:10.1029/2002JC001447.

Pringle. J. M. (2002), Enhancement of Wind-Driven Upwelling and Downwelling by Alongshore Bathymertic Variability, *J. Phys. Oceanogr.*, 32, 3101-3112.

Seung, Y. H., (1974), A dynamic consideration on the temperatures distribution in the east coast of Korea in August, *J. Kor. Soc. Oceanogr.*,, 9, 23-33.

Smith, R. L., (1981), A comparison of the structure and variability of the flow field in three coastal upwelling regions: Oregon, Northwest Africa, and Peru. Coastal Upwelling, F. A. Richards, Ed., Amer. Geophys. Union, 107–118.

Tilburg C. E and R. W. Garvine (2003), Three-Dimensional Flow in a Shallow Coastal Upwelling Zone: Alongshore Convergence and Divergence on New Jersey Shelf, *J. Phys. Oceanogr.*, 33, 2113-2125.

Torrence C. and G. P. Compo (1998), A Practical Guide to Wavelet Analysis, *Bulletin of the American Meteorological Society*, 79, 61-78.

Yang. H. S., S. J. Oh, H. P. Lee, C. H. Moon, M. S. Han and B. K. Kim (1998), Distribution of Particulate Organic Mater in the Gamp Upwelling Area of the Southwestern East Sea, *J. Kor. Soc. Oceanogr.*,, 33 (4), 157-167.

Yankovsky. A. E., and R. W. Garvine (1998), Subinertial Dynamics on the Inner New Jersey Shelf during the Upwelling Season, *J. Phys. Oceanogr.*, 28, 2444-2458.

Weisberg, R. H., and R. He, Local and deep-ocean forcing contributions to anomalous water properties on the West Florida Shelf, *J. Geophys. Res*., 108(C6), 3184, doi:10.1029/2002JC001407, 2003.

요 약

바람에 의한 연안갇힘파 (Coastal trapped wave) 모델을 적용하여, 동해중부 연안의 두 정점 (외해 정점: 수심 100m, 내해 정점: 수심 27 m)에서 장주기 (수 일에서 수 주일 주기) 수온 변동성을 연구하였다. 모델에 의해 예측된 수온과 관측된 수온 사이에 유의미한 상관성을 보였으며 (외해 정점: 상관계수 > 0.35, 내해 정점: 상관계수 > 0.36), 이러한 상관성은 원거리 바람을 포함하여 예측된 수온변화의 경우가 국지적 바람만 고려하였을 경우보다 내/외해 정점 모두에서 크게 나타났다. 연안갇힘파 모델의 1 모드 전파 속도 (속초-묵호: 4.6 ~ 5.9 m/s, 묵호-포항: 9.5 ~ 10.3 m/s) 역시 해수면 관측자료를 통해 계산된 전파속도 (속초-묵호: 6.1, 묵호-포항: 10.4m/s) 와 일치하였다. 장주기 수온 변동성을 연안갇힘파 모델을 통해 주요 부분을 설명할 수 있을 것으로 사료되며, 장기간 (2006 년 ~ 2011 년) 동안 연안갇힘파 모델을 적용하여 관측자료와 비교한 결과에서도 유사한 상관성을 보였다. 그러나, 연안갇힘파 이론에 의해서만 장주기 수온변동을 모두 설명할 수는 없으며, 특히 비선형 수평 이류가 중요해지는 시기에는 관측과 예측 값이 큰 차이를 보였다. 또한 본 연구를 통해, 하강류에 의한 수직혼합과 일주기 변동에 의한 eddy heat flux 역시 연안갇힘파 모델에 의한 수온 예측 결과와 관측결과의 차이를 증가시킬 수 있음을 보였다.

내해에서 바닥 수온 변화는 외해의 수온변화에서 나타나는 연안갇힘파 외 추가적인 국지적 영향을 포함하고 있다. 내해 정점에서의 장주기 수온변동은 외해의 연안에 나란한 방향의 해류와 해류의 수직전단 변동과 강한 연관성을 보였으며, 내/외 정점간 수평적 수온 차이와 외해 정점에서의 수직전단과의 상관도가 0.87 이상으로 높은 상관성을 보였다. 이러한 결과는 본 연구해역에서 지형류적 균형을 이루고 있음을 나타낸다. 내해 정점에서 발생하는 용승 현상은 연안에 나란한 방향의 바람이 없는

기간에도 뚜렷하게 나타났다. 내해의 장주기 수온변화는 바람에 의한 연안 용승과 바람에 의하지 않은 용승으로 구분되었으며, 국지적 바람과 연관성이 없는 용승 현상은 외해의 유속 변화와 더불어 내대륙붕 순환의 주요 변화 요인으로 판단된다.

주요어: 장주기 수온변동성, 연안갇힘파, 대륙붕, 동해

학번: 2001-30270

.